

Self-Assembly of Magnetic Nanoparticles: A Tool for Building at the Nanoscale

Suvojit Ghosh

Dissertation submitted to the faculty of the Virginia Polytechnic Institute and State University in partial fulfillment of the requirements for the degree of

**Doctor of Philosophy
In
Engineering Mechanics**

Ishwar K. Puri, Chair
Muhammad R. Hajj, Co-Chair
Marwan Al-Haik
Sunghwan Jung
John J. Socha
Elankumaran Subbiah

December 2, 2013
Blacksburg, VA

Keywords: magnetic nanoparticles, superparamagnetism, self-assembly, tissue engineering, functional grading

Copyright © 2013, Suvojit Ghosh

Self-Assembly of Magnetic Nanoparticles: A Tool for Building at the Nanoscale

Suvojit Ghosh

ABSTRACT

Nanoparticles can be used as building blocks of materials. Properties of such materials depend on the organization of the constituent particles. Thus, control over particle organization enables control over material properties. However, robust and scalable methods for arranging nanoparticles are still lacking. This dissertation explores the use of an externally applied magnetic field to organize magnetic nanoparticles into microstructures of desired shape. It extends to proofs of concept towards applications in material design and tissue engineering. First, external control over dipolar self-assembly of magnetic nanoparticles (MNPs) in a liquid dispersion is investigated experimentally. Scaling laws are derived to explain experimental observations, correlating process control variables to microstructure morphology. Implications of morphology on magnetic properties of such structures are then explored computationally. Specifically, a method is proposed wherein superparamagnetic nanoparticles, having no residual magnetization, can be organized into anisotropic structures with remanence. Another application explores the use of magnetic forces in organizing human cells into three-dimensional (3D) structures of desired shape and size. When magnetized cells are held in place for several days, they are seen to form inter-cellular contacts and organize themselves into tight clusters. This provides a method for 3D tissue culture without the use of artificial scaffolding materials. Finally, a method to pattern heterogeneities in the stiffness of an elastomer is developed. This makes use of selective inhibition of the catalyst of crosslinking reactions by magnetite nanoparticles. The last chapter discusses future possibilities.

*Dedicated to my parents,
for their unconditional support throughout my life.*

Acknowledgements

First and foremost, I would like to thank my advisor Prof. Ishwar K. Puri for being the perfect mentor. He inspired me to take on challenges which I would have never dared to pursue on my own. He motivated me to be a dreamer, to break free of the tethers of rationality in pursuit of the new. He made me good at what I do best. And he did all of this without ever telling me what to do or how to do it. I have learnt a lot from him, but the most important of all is the skill to be independent.

My utmost gratitude goes to all my committee members. They have helped me immensely on this journey of self-discovery, and for this I will be forever in their debt. Their unconditional support and confidence in my abilities allowed me to pursue my dreams. Their mentorship and advice were extremely valuable to every aspect of my life in the PhD program.

I must also thank all my teachers at Virginia Tech and prior. Their self-less dedication to teaching and mentorship has given me a rock-solid foundation in the laws of nature, enabling the broad diversity in my research pursuits. Their constant emphasis on the significance of originality inspired me to be creative.

I have to thank the whole ESM family; they made me feel at home in a land far away from home. Anne-Marie, Cristina, Linda, Lisa, Melissa, Sally, Dave, Danny, Darrel, Mac, Mark, Mike, Paul – they were always around to help when help was needed. They made my life easy in situations when it could have been very difficult. And they did all of this with a big smile. I felt

at home in Norris Hall, and I hope to come and visit whenever possible. I made some great friends in Norris, some that will last a life time.

I would like to thank my fellow members of the MuRG family. Aschvin, Austin, Ganesh, Monrudee, Ravi and Souvik made every day in the lab special. Be it through intellectual discussions, aggressive criticism or pointless blabber at 3 am, I had a special time in 200 Norris Hall. I have forged lifelong ties with these exceptional people, and count them as my family.

I had a second family in Blacksburg. The Subbiah Lab took me in as their own, and armed me with tools and resources to pursue some “really crazy work”. Adria, Arti, Chandra, Jagadees, Mona, Pamela, Ramesh, Sandy – they made me feel at home in a laboratory engaged in pursuits far beyond my understanding. They introduced me to the fascinating world of hands-on Biology. Experiments with cells are a crucial part of my doctoral research, and these would have never been possible without their support and encouragement.

I made a lot of great friends in Blacksburg. They made my time in this town very special. Be it going bar-hopping after a hard week’s work or playing cricket in a basketball court on a summer weekend, life would have been a lot duller without these special people. My friends have always been my pillars of support; they have helped me through some extremely difficult times. I am grateful to have encountered such amazing individuals during my doctoral studies.

Last but definitely not the least; I would like to thank my parents. This is not just for their constant and unconditional support throughout my life (which I take for granted), but for spawning an indomitable curiosity in me from the early days. I recall conversations with my father on space travel and satellite relay systems for inter-galactic communication pathways well before I reached age 10. My mother, a botanist by profession, took me on several excursions with her college students at a very young age. As part of those tours, I was introduced to the

enormity and diversity of plant life in Indian forests. I was initiated in the world of scientific investigation at a very early age; science was a topic of dinner table conversation at home. A child always looks up to their parents as role-models, and I was no exception. I was set for a career in research before I ever got to 3rd grade. My parents have been the single greatest influence on my life. Without them, life would have never been the same.

Suvojit Ghosh

Blacksburg, VA

December, 2013

Attributions

Prof. Ishwar K. Puri is my advisor and committee chair. He was the primary mentor for all the work presented in this dissertation, and provided guidance, support and valuable critique. He also contributed significantly to the written communication of the research.

Prof. Elankumaran Subbiah provided support and mentorship for the work on magnetic assembly of 3D cell cultures and contributed significantly to its written communication. Dr. Ramesh Jadi and Dr. Sandeep Kumar provided experimental support and expertise in this work.

Professor Marwan Al-Haik provided support and mentorship for the work on patterning of stiffness in polydimethylsiloxane. Dr. Mehran Tehrani provided experimental support and expertise on use of instrumented nanoindentation in this work. Both Professor Al-Haik and Dr. Tehrani contributed significantly to the written communication of the corresponding results.

Contents

Abstract	ii
Dedication	iii
Acknowledgements	iv
Attributions	vii
List of Figures	xii
List of Tables	xxi
1. Introduction.....	1
1.1 Form defines properties.....	1
1.2 Design of materials – <i>nanomaterials as building blocks</i>	2
1.3 Organizing nanoparticles by self-assembly.....	2
1.4 Dipolar self-assembly of magnetic nanoparticles	4
1.5 Magnetophoretic transport	4
1.6 A brief outline	5
1.6.1 Chapter 2	5
1.6.2 Chapter 3	6
1.6.3 Chapter 4	6
1.6.4 Chapter 5	7
1.6.5 Chapter 6.....	7
2. Controlled self-assembly using external magnetic field.....	9
2.1 Motivation and background	9

2.2	Materials and methods	12
2.2.1	Generation of composite microstructure.....	12
2.2.2	Sample preparation for X-Ray computed tomography	13
2.2.3	Sample preparation for TEM	13
2.2.4	Magnetic field setup.....	13
2.3	Scaling analysis	14
2.3.1	Relating magnetophoretic velocity to particle size.....	14
2.3.2	Relating structure anisotropy to magnetic field	15
2.4	Results and discussions	18
2.4.1	Dynamics of a magnetic nanoparticle.....	19
2.4.2	Height of microstructure (h)	20
2.4.3	Substrate coverage fraction (ξ).....	21
2.4.4	Structure anisotropy (ϑ).....	22
2.4.5	Anisotropy in clusters of nanoparticles.....	23
2.5	Conclusions	25
2.6	Acknowledgements	25
3.	Properties of nanoparticle ensembles: <i>Anisotropy enhancement by dipolar interactions</i>	26
3.1	Background and motivation	26
3.2	Theory	30
3.3	Computational method	35
3.4	Results and discussions	36
3.4.1	Anisotropy enhancement in a two-particle system	36
3.4.2	Parametric design for dipolar stabilization of magnetization reversal.....	43

3.4.3	Magnetization reversal in longer chains ($N > 2$)	47
3.5	Conclusions	49
3.6	Acknowledgements	50
4.	Magnetic assembly of 3D cell culture	51
4.1	Motivation and background	51
4.2	Materials and Methods	54
4.2.1	Synthesis of magnetic nanoparticles	54
4.2.2	Characterization of magnetic nanoparticles.....	54
4.2.3	Cell culture.....	55
4.2.4	Magnetization of cells.....	56
4.2.5	Sample preparation and imaging with Scanning Electron Microscopy (SEM).....	57
4.2.6	Confocal microscopy	57
4.3	Results and Discussions	58
4.4	Conclusions	65
4.5	Acknowledgements	65
5.	Patterning stiffness of elastomers by magnetophoretic control of catalyst inhibitor distribution	67
5.1	Motivation and background	67
5.2	Materials and methods	70
5.2.1	Synthesis of Magnetic Nanoparticles and Ferrofluid.....	70
5.2.2	Preparation of Nanocomposites	72
5.2.3	Mold Fabrication.....	72
5.2.4	Nanoindentation.....	73

5.3	Results and discussions	73
5.4	Conclusions	77
5.5	Acknowledgements	77
6.	Future directions	78
6.1	Vision	78
6.2	Controlled Self-assembly of Nanoparticles.....	79
6.3	Magnetic Forces in Biotechnology	80
6.4	Material Design	81
7.	References.....	82

List of Figures

Figure 2-1 (a) Magnetic nanoparticles dispersed in a fluid move towards locations that experience a stronger magnetic field. The particles initially agglomerate into clusters. Strong dipole-dipole interactions amongst clusters enable self-assembly into filaments. (b) The nanoparticles are initially uniformly dispersed in liquid PDMS prepolymer. (c) The polymer is cured while the system experiences an externally imposed magnetic field. The polymer matrix preserves the shapes of the self-assembled structures when the field is removed. (d) The structure morphology can be controlled by varying $ \mathbf{B}^{ext} $ and $ d\mathbf{B}^{ext}/dx $, as shown for three experimental conditions obtained by three curing positions relative to a system of two NdFeB permanent magnets. The values obtained, labeled A, B and C, are listed in Table 1. (e-g) Three-dimensional images obtained by X-Ray MicroCT reconstructions show variations in the microstructure geometry. Reproduced from Ref. [48] by permission of The Royal Society of Chemistry.....	11
Figure 2-2 (a) Map of magnetic field strength $ \mathbf{B}^{ext} $ with values of the (b) x -components of \mathbf{B}^{ext} , and (c) its gradient $d\mathbf{B}^{ext}/dx$ determined from FEMM software. Reproduced from Ref. [48] by permission of The Royal Society of Chemistry.....	14
Figure 2-3 A simplified two particle system demonstrates how anisotropy increases with increasing gradient of the magnetic field. Reproduced from Ref. [48] by permission of The Royal Society of Chemistry.....	16
Figure 2-4 (a) Optical micrograph images of self-assembled structures in profile, for the three different conditions labeled A, B and C (See Table 2-1), for the three different particle	

concentrations used in the experiments. The insets are high magnification images of the corresponding tips. The scale bar in insets measure 25 μm . (b) The height h decreases monotonically with $|d\mathbf{B}^{\text{ext}}/dx|$. Height of error bar is 2σ and is absent where occluded by plot marker. Sections reproduced from Ref. [48] by permission of The Royal Society of Chemistry..... 20

Figure 2-5 (a) Optical micrographs of the substrate in the dispersion showing the base of the filamentous microstructure for the various experimental conditions. The size of scale bar is 25 μm . (b) The coverage fraction ξ determined from such images demonstrate its monotonic dependence on $|\mathbf{B}^{\text{ext}}|$. Height of error bars is 2σ . Error bars are absent where occluded by plot markers. Sections reproduced from Ref. [48] by permission of The Royal Society of Chemistry..... 22

Figure 2-6 The anisotropy metric ϑ increases monotonically with the gradient of the external magnetic field. Reproduced from Ref. [48] by permission of The Royal Society of Chemistry..... 22

Figure 2-7 TEM micrographs close to the base of the microstructures in profile view show that the structures consist of MNP clusters organized along the magnetic field. (a) Individual clusters behave as dipoles enabling long range organization. However, the polymerization process interferes with such interactions to form irregular chains. (b) The clusters are not isotropic as expected from van der Waals interactions alone, indicating that there is an interplay between dipolar and van der Waals interactions in their formation. (c) The clusters are roughly 100 nm thick, but their lengths are much larger. The uneven brightness in the background is a consequence of the microtomining process used in sample preparation. Reproduced from Ref. [48] by permission of The Royal Society of Chemistry. 24

Figure 3-1 The potential barrier for magnetization reversal in an anisotropic ensemble of MNPs

is higher than that in an isolated particle due to magnetostatic coupling. Images of the self-assembled ensembles of magnetite nanoparticles in PDMS matrix obtained with (a) an optical microscope, and (b) X-Ray computed tomography show pillar-like structures consisting of chains that are aligned with the direction of the imposed field. The $\sim 750 \mu\text{m}$ tall pillars taper off from a $\sim 5 \mu\text{m}$ thick base and are highly anisotropic. (c) A system of two MNPs is the simplest system with which to study the effect of dipolar interactions in anisotropic structures. Here, the easy axes \mathbf{n}_1 and \mathbf{n}_2 lie along the straight line joining the centers. The magnetic moments \mathbf{m}_1 and \mathbf{m}_2 can rotate with respect to the particles due to the low magnetocrystalline anisotropy. (d) The total potential energy $E = E_{dip} + E_a$ of this system reaches a minimum value when $\theta = 0, \pm\pi$, i.e., the moments are parallel to each other as well as to the line joining the centers of the two particles. Note that the energy map is a planar projection of a four dimensional space containing all possible stable equilibria.²⁸

Figure 3-2 Determination of the potential barrier E_b from numerical simulations. (a)

Variation of reversal frequency f with temperature for magnetite particles with $a = 3.5 \text{ nm}$. The logarithmic nature of the plot indicates that the Néel-Arrhenius relation is followed. The effective potential barrier E_b is obtained from the slope and compared with theory in Table 3.3. (b) The maximum change in energy ΔE_{max} for an interval of $1 \mu\text{s}$ is seen to remain same for $N = 1$, but increases with $N = 2$. Also, while ΔE_{max} matches E_b for $N = 1$, the saddle point hypothesis in Equation (3.6) underestimates actual energy expense in reversals. The heights of the error bars equal 2σ (determined from ten simulations) but these are absent where occluded by the plot markers. 37

Figure 3-3 The dynamics of the x -component of the magnetic moment for two magnetite nanoparticles with aligned easy axes and the corresponding potential energy E of the system determined from Equation (3.5). (a) Over a period of 1 μ s, magnetization reversal is always collective, i.e. the two moments reverse together. The data presented here are for $a = 3.5$ nm at $T = 300$ K, but the observation is universal. The corresponding energy plot shows peaks above the theoretical potential barrier E_b determined from Equation (6). While few of these peaks correspond to magnetization reversals, many do not. (b) Closer observation of a single reversal event from the same data shows that the potential energy attained by the system during reversal is much larger than E_b , proving that magnetization reversal does not necessarily occur along the saddle points in the energy surface that present the lowest potential barrier E_b for it to occur. (c) Another interval from the same data shows that although the potential energy attained is above E_b , a reversal is not encountered. The reversal is prevented because the system here achieves this energy at a location far away from the saddle points. E/KV values are shifted in origin to have the equilibrium configuration be represented by $E = 0$ 39

Figure 3-4 The magnetization dynamics of two neighboring magnetite particles with $a = 3.5$ nm at $T = 300$ K show that the mode of switching is close to symmetric fanning, i.e., $e_{1y}e_{2y} < 0, e_{1z}e_{2z} < 0$. High thermal noise is visible..... 41

Figure 3-5 The magnetization reversal frequency diminishes exponentially with volume in an isolated MNP as well as the terminal particle in a linear chain. The slope of the curve allows K_{eff}^{num} to be determined, while the y -intercept provides the value of the attempt frequency f_0 (Table 3.3). The simulations represent magnetite nanoparticles with a damping

coefficient $|\lambda|=0.1$. Each data point is the mean value realized from 10 simulations of $1\text{ }\mu\text{s}$ duration. 42

Figure 3-6 The dynamics of the x -component of the dimensionless magnetic moment for the terminal magnetite MNP show the stabilizing effect of dipolar interactions on the magnetic moment. Various particle sizes ($3\text{ nm} \leq a \leq 6\text{ nm}$) are considered in MNP chains of different lengths ($N = 1, 2, 3$). For a particular particle radius, the terminal MNP of a longer chain has a smaller number of reversals. 44

Figure 3-7 The lower limit on particle size for stable magnetization depends on the chain length. (a) An isolated MNP reaches stable magnetization at a larger radius than for an idealized two- or three-particle chain, as shown for magnetite particles. (b) The ratio of these limiting radii for an isolated particle and a two-particle system is a function of the dimensionless interaction strength $k_{int} = \mu_0 M_s^2 / 24K$. The value of k_{int} for a material provides the bounds on MNP sizes that can be contained in a dispersion that can be self-assembled to structures with remanence. The heights of the error bars equal 2σ (determined from ten simulations) but these are absent where occluded by the plot markers. 47

Figure 3-8 Variation of $\langle e_x \rangle$ of a terminal dipole with chain length shows that (a) a longer magnetite MNP chain produces a more stable magnetic moment. This stability increases until saturation, i.e. $\langle e_x \rangle \sim 1$. The increase is more rapid for larger particle dimensions, which is explained by the higher system anisotropy that scales as a^3 . (b) The variation of $\langle e_x \rangle$ along the chain (for $a = 3.5\text{ nm}$) shows more stable relative magnetization closer to the center of the chain. 48

Figure 4-1 Size of the BSA coated MNPs (a&b) TEM images show that the magnetic core of the MNPs has a diameter of $\sim 10\text{ nm}$. (c) Dynamic light scattering analysis shows that the

modal value of the hydrodynamic diameter of BSA coated MNPs are ~50 nm in its original water solution, and ~80 nm when the solution is diluted in PBS. (d) The nanoparticle tracking analysis (NTA) results confirm the DLS results..... 55

Figure 4-2 Cytotoxicity of the BSA coated MNPs are evaluated by measuring the % viability of PC-3 cells at various concentrations of MNPs in PBS. Measurements are done by typan blue staining of dead cells, followed by counting using the Nexcelom Cellometer®. Height of error bars = 2σ , $N = 4$ 56

Figure 4-3 Megnetic assembly of 3D cell culture. (a) Multi-stage seeding process wherein a thick 3D culture is built layer-wise by an interplay of magnetic forces and cellular adhesion, enabled by adding a layer of cells at ~1 hour intervals. (b) Configuration of the apparatus showing the coverslip over an NdFeB disc magnet. (c) A 6 layer seeding of vero cells is visible to the naked eye. (d) Immediately after a 6 layer seeding, cells form a 3D cluster directly above the magnet. (e) After 5 days of culture, vero cells are observed to migrate away from the central high population cluster..... 58

Figure 4-4 Culture of 3D spheroids in suspension. (a) Magnetized cells, suspended in culture media inside a petridish, were assembled into 3D structures at the air-medium interface using magnets fitted to the petridish cover. The dish was incubated in this position for 5 days, resulting in 3D spheroids. (b) Image of spheroids (red oval) formed in suspension using magnetic forces. Inset: Cylindrical NdFeB magnets anchored to the petridish cover. 59

Figure 4-5 Control of shape using magnetic field. (a) A cylindrical disc magnet, which is axially magnetized, produced a circular sheet of cells. (b) A ‘flux gap’, formed by a layer of non-magnetic material sandwiched in between two rectangular magnets, produced a more anisotropic assembly. The PC-3 cell clusters presented here were fixed 5 days after seeding

for SEM imaging. Insets: NdFeB magnet configuration used in each assembly. Note: Cracks in the cell assembly were a consequence of the sample preparation process; they were not seen in the live cell assembly..... 60

Figure 4-6 Morphology and Intercellular connections. Cell monolayers (a,c) acquired the familiar flattened form while cells organized into 3D clusters (b, d) were spheroidal. Cell-cell contacts were also influenced through the 3D assembly. (a) Monolayers of PC-3 cells showed extracellular fibers on their surface, but such fibers did not visibly serve any mechanical function. (b) When the PC-3 cells were organized into 3D clusters using magnetic forces, these fibers formed inter-cellular connections (see red arrows). (c) Monolayers of HFL-1 cells had no inter-cellular contact. (d) HFL-1 cells organized in 3D clusters exhibited ample evidence of inter-cellular contacts aided by extra-cellular fibers (see red arrow). 61

Figure 4-7 Confocal microscopic image of a 3D cluster of PC3-mOrange cells assembled by magnetic forces showing (a) cells on the lower end of the cluster that were in contact with the glass substrate of the coverslip take the familiar elongated form of the monolayers, while (b) cells which have physical contact only with other cells acquired a spherical morphology. The light blue arrowhead and the line shows the position in the Z-stack for the cross-section displayed. 62

Figure 4-8 Figure 4 PC-3 cells organize themselves into a tight multilayer sheet. (a) PC-3 cells were initially assembled into a ring above a disc-shaped magnet. The cells organized themselves into a multilayer circular sheet over time. (b) Evidence of tension on an intercellular fiber given by observed stretching in the cell attached to it (red arrow) suggests that the cells pull themselves together using these fibers. 63

Figure 4-9 HFL-1 cells pack themselves into a tight spheroid. (a) Side view of a dislodged cluster (inset: lower magnification) shows (b) the underside that is torn away from the glass contains inter-cellular contacts and extracellular materials, while (c) the outside surface, which interfaced with the culture media, is smooth and comprised of stretched cells. (d) The stretched cells form inter-cellular contacts through filopodia-like protrusions..... 64

Figure 5-1 Magnetophoretic control of MNP concentration distribution used to pattern stiffness of PDMS. (a) PDMS is dissolved in a kerosene based ferrofluid containing MNPs (shown disproportionately large for illustration). The solution is then cast into molds close to a NdFeB magnet. Within ~30 minutes of casting, all MNPs in the solution move to the region immediately above the magnet. The kerosene is then evaporated under vacuum for ~24 hours at room temperature, then kept 60°C for another 24 hours for curing. This preserves the MNP concentration distribution. Instrumented nanoindentation is then performed along the boundary between pure PDMS and the PDMS having high MNP concentration. (b) Mold used in this experiment, having a PMMA coverslip as its floor, with a NdFeB magnet covering half of the floor. (c) Solution of PDMS in kerosene is poured into the mould. (d) After ~30 minutes, MNPs become concentrated in the region above the magnet. (e) Magnified image of the boundary, showing a sharp gradient in the MNP concentration..... 69

Figure 5-2 Dynamic light scattering shows that the hydrodynamic diameter of MNPs lie between 10 and 30 nm. There is some agglomeration (~100 nm)..... 71

Figure 5-3 Effect of MNP doping on reduced modulus (E_r) determined from homogeneous composites (a) Pure PDMS is much stiffer than PDMS with 10% (w/w) MNPs, as determined from the slope of the force-displacement curve obtained by instrumented

nanoindentation. (b) E_r first increases slightly with ψ , as is commonly observed in polymer composites that contain a harder dispersed phase. For $\psi > 5\%$, catalyst inhibition becomes dominant and E_r decreases monotonically with ψ 73

Figure 5-4 Magnetophoretic patterning of E_r . (a) The magnetic field is strongest along the periphery of the rectangular NdFeB magnet, thus MNP concentration is highest immediately above the periphery. The sample shown here has a starting MNP concentration $\psi^* = 0.1\%$ which best illustrates this feature. The dots show approximate locations of indentation points. (b) Map of E_r obtained from indentation at these points show that E_r varies long y axis. Data presented is for a sample with $\psi^* = 1.0\%$ 75

Figure 5-5 High resolution scan of E_r along a straight line for samples with (a) $\psi^* = 1.0\%$, (b) $\psi^* = 0.5\%$, (c) $\psi^* = 0.1\%$ shows that high gradients of the reduced modulus can be formed. The steepest gradient in (a) is 12.6 MPa mm^{-1} ($R^2 = 0.9623$). The general U-shaped profile is seen in all samples. The red dashed line is a 5-point moving average. (d) The minimum reduced modulus (E_r^{min}) decreases linearly with ψ^* 76

List of Tables

Table 2-1 Magnetic field $ \mathbf{B}^{ext} $ and its gradient $ d\mathbf{B}^{ext}/dx $ for the three different configurations shown in Figure 1 (d). The values are obtained using the Finite Element Method Magnetics software and verified by a Hall Probe.....	14
Table 3-1 Nomenclature.....	31
Table 3-2 Comparison of the numerically determined E_b^{num} for magnetite particles with $a = 3.5$ nm with theoretical models.....	37
Table 3-3 K_{eff} calculated from Equation (7) for $N = 2$, the numerically determined effective anisotropy K_{eff}^{num} from Figure (3-5), and the attempt frequency f_0 determined from Figure (5) for magnetite nanoparticles.....	42
Table 3-4 Material properties of common MNP core materials [80] and the calculated critical radii for stable magnetization of isolated MNPs (a_1) and two-particle systems (a_2) over measurement time $\tau_m = 100$ ns.	46

1. Introduction

1.1 Form defines properties

The world around us presents a well-defined correlation between form and function. This is largely because the properties of an entity are largely dependent on its form. Mechanical properties of an entity are no exception, and this is evident in commonly encountered objects. For instance, the opaque and soft StyrofoamTM packaging material has the same atomic structure as the brittle and transparent polystyrene petridish, differing only by the air-filled voids present in the former. The stiffness of a closed coil helical spring is given by [1]

$$k = \frac{Gd^4}{64R^3n}. \quad (1.1)$$

Here, the shear modulus G and the wire diameter d are the only ‘intrinsic’ properties of the wire forming the spring. However, the stiffness can be changed by changing the ‘form’ variables, i.e. the coil radius R or the number of coils n .

The phrase ‘material properties’ was carefully avoided in the preceding paragraph as the properties discussed were of a system, not necessarily a material. However, looking down at the atomic constitution demonstrates that material properties are highly dependent on form. Form in this context refers to arrangement of atoms. Diamond, graphite and carbon black are all made up of identical carbon atoms, differing only in their crystal structure, or the lack thereof. A difference in relative positioning of the carbon atoms can bring about wide differences in mechanical, optical, electric and chemical properties of these materials. This is observed even at the scale of a single molecule. For instance ethanol and dimethyl ether have the same molecular

constitution C_2H_6O , differing only in relative positioning of the constituent atoms. However, differences in physical properties, e.g., melting and boiling points, are significant [2]. Mother Nature has taken advantage of this dependence, designing materials optimized for her creations through millennia of painstaking experimentation, i.e., evolution. Recent atomistic investigations testify to this, demonstrating how structures of various proteins are optimized for their performance [3].

1.2 Design of materials – nanomaterials as building blocks

Our methods are rather limited compared to natural evolution of materials. There is, however, an immediate need for technology which enables development of materials optimized for a specific use. In this emerging field called material design, nanotechnology plays a crucial role. Nano-scale materials, e.g., nanoparticles, comprise only a few thousand atoms each. They are often known to present very interesting material properties on their own [4]. But most fascinating is the emergence of bulk properties of materials that depend solely on the manner of arrangement of nanoparticles contained within. Nanoparticles can thus play the ‘atoms and molecules’ in designing materials tailored to an application [4, 5]. The only limiting factor lies in the methods for enforcing a predesigned arrangement of these building blocks. Several efficient methods for organizing nanoparticles into superlattices have been developed over the last two decades [6, 7]. However, they are often very specific to particle materials, require complicated processing steps and have extremely low throughput.

1.3 Organizing nanoparticles by self-assembly

Various methods have been developed for structuring nanomaterials with high precision. For instance, lithographic methods using an electron beam enable a top down way of shaping

materials with nanoscale resolution [8]. High precision bottom up methods can be sought in optical tweezers which accurately arrange nanoparticles one at a time [9]. Such methods have extremely high costs due to the requirement of sophisticated instrumentation, suffer from low throughput and are often limited in terms of material choice. Consequently, they do little to go beyond scientific experiments. Self-assembly is a promising alternative. Besides the inherent high throughput, it eliminates the need of all but the very basic instrumentation.

A self-assembly process typically uses a manipulation strategy to enforce patterned aggregation of a group of similar ‘building blocks’, e.g., nanoparticles. It exploits the interactions that a particle has with other similar particles in its vicinity, e.g., through chemical bonding, coulombic or magnetostatic interactions [6, 7]. In addition, one or more externally applied drivers may be used to enforce long range order in inter-particle interactions, e.g., an electric or magnetic field [10, 11], thermophoresis [12], or capillary forces [13]. While simple in implementation, fine control over the position and orientation of individual particles require a rigorous analytical framework that accurately models the process. However, inter-particle interactions at the nanoscale are still being explored and a comprehensive understanding is often absent. This forms the single most important impediment for using self-assembly of nanoparticles as a tool for material design.

Most popular methods for nanoparticle self-assembly use patterned molecular ligands on the particle surface. Such ligands interact with each other and assemble the particles into superlattices [14-18]. Other methods such as evaporation [19] and templating [20, 21] have also been explored, each with its own set of benefits and limitations. An exhaustive review of self-assembly methods in nanoparticles will be digressive for the scope of this document. Instead, we

focus on a specific type of self-assembly that is investigated herein, i.e., magnetic field driven dipolar self-assembly of magnetic nanoparticles (MNPs).

1.4 Dipolar self-assembly of magnetic nanoparticles

An MNP typically comprises a single magnetic domain of a ferro- or ferrimagnetic material. Strong exchange interactions ensure that the magnetic moment of all individual atoms within an MNP are approximately coherent [22]. An MNP thus behaves as a point dipole. Colloidal dispersions of MNPs, often known as ferrofluids, form a popular model to investigate dipolar self-assembly. The key inter-particle interaction driving self-assembly of magnetic colloids is the magnetostatic dipolar interactions. This competes with other inter-particle influences in self-assembly, e.g., van der Waals and Coulombic forces. The key feature in dipolar interactions is that it can be manipulated with an externally applied magnetic field. This provides external control over the self-assembly process. This will be discussed in detail in Chapter 2 along with a comprehensive review of recent literature.

1.5 Magnetophoretic transport

The magnetic nature of MNPs ensures a second opportunity in organization; each MNP moves towards a stronger magnetic field. Thus, a desired concentration distribution of MNPs can be enforced in a liquid dispersion by a suitable spatially varying magnetic field that is determined *a priori*. This has enabled several relevant applications. For instance, magnetic drug targeting uses MNPs conjugated with drug molecules. Concentration distribution of said drugs can thus be controlled using a magnetic field. This enables localized therapy at the site of an infection or a tumor [23, 24]. This principle is also used throughout the work reported herein, applied to magnetic assembly of artificial tissues and patterning material properties in composite materials.

1.6 A brief outline

The simplicity in implementation and the versatility in patterning possibilities that emerge when dipolar self-assembly and magnetophoretic transport of MNPs are coupled has motivated all investigations documented herein. This is laid out in the following chapters. Each chapter describes an independent investigation contributing to the central theme of organizing MNPs using an externally applied magnetic field. This section presents a brief outline of the remainder of the document.

1.6.1 *Chapter 2*

Chapter 2 investigates external control of shape, size and location of microstructure formed by self-assembly of MNPs in a liquid dispersion. A magnetic field is used to influence the dynamics of MNPs in the liquid precursor of polydimethylsiloxane (PDMS). MNPs are observed to agglomerate by interplay of van der Waals and dipolar interactions to form anisotropic clusters. The clusters are concentrated near a substrate by magnetophoretic transport. Inter-cluster dipolar interactions are substantial, consequently the clusters self-organize to form filamentous microstructure parallel to the field. The PDMS is cross-linked in the presence of the field to preserve the microstructure. This enables a means to pattern magnetic microstructure in a composite. The externally applied magnetic field and its gradient serve as the two main control variables in such microstructure patterning. Their influence on microstructure geometry is investigated using X-Ray microCT, TEM and light microscopy. The correlations are explained through scaling laws that model the influence of the said control variables on dynamics of MNPs.

1.6.2 Chapter 3

In a closely packed ensemble of MNPs, the proximity of neighboring particles entails substantial inter-particle magnetostatic influence on the dynamics of the individual moments. This has a significant bearing on magnetic properties of self-assembled ensembles. This is numerically investigated in **Chapter 3**. A specific configuration is addressed wherein appropriate orientation of the particle easy axes causes transition of magnetic behavior from superparamagnetic to ferromagnetic. Individual MNPs are often superparamagnetic, i.e., they have zero effective residual magnetization. This is because of the frequent thermally driven reversals of its moment caused by a low barrier for magnetization reversal [25]. However, in the aforementioned configuration, magnetostatic interactions enhance the barrier. The frequency of reversals is thus reduced, and a group of self-assembled superparamagnetic particles develop a residual magnetization. A significant observation is that contrary to theoretical predictions [26], magnetization reversals do not necessarily occur along the energetically cheapest path. The study extends to develop a parametric design strategy of developing residual magnetization in self-assembled structures of superparamagnetic particles.

1.6.3 Chapter 4

3D cell culture methods in use rely on direct contact of cells with an artificial scaffold. Such surfaces cause undesirable mechanical or chemical interference. This is overcome by magnetic assembly of cells into a 3D structure, reported in **Chapter 4**. MNPs are synthesized by coprecipitation reaction and coated with a serum protein. Once coated, the MNPs are readily internalized by cells. Magnetized cells suspended in the culture medium are subsequently exposed to an externally applied magnetic field using NdFeB magnets. The cells assemble into 3D clusters due to magnetic forces. Shape and size of such clusters can be controlled as desired.

Further, the cells form intercellular contacts aided by extra-cellular fibers. Over the next few days, the cells organize themselves into tighter clusters; for epithelial cells, the cluster takes the form of a multi-layer sheet, while for fibroblasts, it is a tightly packed spheroid. The connecting fibers are observed to exercise tension on the cells. This suggests that the fibers are responsible for organizing the cells. For the HFL-1 cell line, cells on the periphery of the 3D clusters are seen to assume a different morphology than the cells that lie within them. This shows that cells assume different physical forms based on their functional role, as determined by sensing their microenvironment.

1.6.4 Chapter 5

An externally applied magnetic field enables control of the concentration distribution of MNPs in a liquid dispersant. If this liquid is a polymer precursor, it can be cured to preserve the said distribution. We use this principle to pattern the elastic modulus of polydimethylsiloxane (PDMS). Crosslinking reactions in PDMS are accelerated by a platinum catalyst. MNPs act as an inhibitor to the platinum. Thus, when MNPs are mixed with the liquid precursor of PDMS, the elastic modulus is degraded. A higher concentration of MNPs yields a less stiff PDMS. The magnetophoretic control over MNP concentration distribution and the catalyst inhibiting effect of are combined in **Chapter 5** to prescribe a desired pattern for the elastic modulus in a PDMS-MNP composite system.

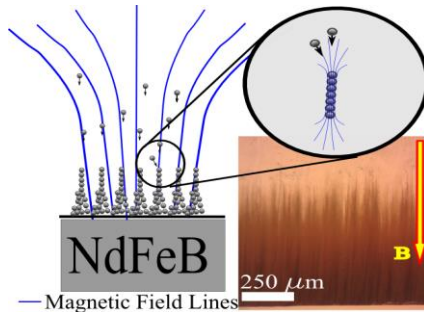
1.6.5 Chapter 6

External control over organization of nanoparticles promises applications in several disciplines. However, the means to enforce organization are still quite limited. **Chapter 6** discusses possible avenues towards new means for control by exploring the full spectrum of electromagnetic

interactions among nanoparticles. In addition, specific applications of such tools are discussed, concentrating on the areas of material design and tissue engineering.

2. Controlled self-assembly using external magnetic field¹

External control of dipolar self-assembly in a liquid dispersion of magnetic nanoparticles is explored. Magnetic nanoparticles are seen to agglomerate by interplay of van der Waals forces and dipolar interactions to form anisotropic clusters. These clusters are concentrated on a substrate by magnetophoresis, wherein they self-organize by dipolar interactions to form microscopic filaments along the field direction. Using diluted PDMS precursor as the liquid dispersant enables preservation of microstructure shape by cross-linking the polymer in the presence of the magnetic field. The field and its gradient are the two main control variables of interest when considering magnetic control of microstructure shape. Their influence is investigated through correlations with the height of a characteristic self-assembled filament, fraction of the substrate area covered by the microstructure and its shape anisotropy. These relations enable *a priori* design of microstructure in a composite material.



2.1 Motivation and background

We investigate external magnetic control of the shape of microstructures formed by self-assembly of magnetic nanoparticles (MNPs). The bottom up method provides simple and effective control over the geometry of microstructure in nanocomposites. Magnetic nanoparticles

¹Adapted from S. Ghosh and I. K. Puri, "Soft polymer magnetic nanocomposites: microstructure patterning by magnetophoretic transport and self-assembly," *Soft Matter*, vol. 9, pp. 2024-2029, 2013. Sections of this chapter have been reproduced by permission of The Royal Society of Chemistry.

(MNPs) are self-assembled in the liquid precursor of polydimethylsiloxane (PDMS) in the presence of a magnetic field \mathbf{B}^{ext} applied using NdFeB permanent magnets. First, the MNPs are dispersed in diluted liquid prepolymer. Combination of van der Waal's and dipolar interactions leads to their agglomeration, forming anisotropic clusters. The dispersion is then exposed to \mathbf{B}^{ext} wherein the field gradient $d\mathbf{B}^{ext} / dx$ induces magnetophoretic transport of the clusters towards a substrate in the dispersion, specifically a wall of the cuvette containing it. Close to the substrate, dipolar interactions self assemble the clusters into filaments. The polymer is cured in the presence of the field to preserve the microstructure shape. The geometry of the microstructure filaments is dependent on \mathbf{B}^{ext} and $d\mathbf{B}^{ext} / dx$, demonstrated in Figure 2-1. Such a patterning method can be used to impart desirable mechanical [27, 28], magnetic [29], electrical, thermal and optical [30] properties to composites, forming a novel tool for material design [4, 21].

MNPs find applications in spintronic devices [31], data recording media [32], particle sorting in microfluidics [33, 34], targeted drug delivery [35, 36], nanocomposites [37], and actuation systems in microdevices [38-40]. These applications need control over the relative positions of particles in packed structures, or could significantly benefit from it. Magnetostatic interactions among MNPs enable the formation of reversible self-assembled structures in a liquid dispersion [10, 11, 41-44]. This eliminates the need for sophisticated chemical processing routes in patterning, potentially enhancing throughput and facilitating cost benefits. However, the structures formed in a liquid dispersion in the presence of a magnetic field are lost due to thermal agitation once the field is removed. This has motivated investigations of alternate self-assembly routes for MNPs [7] involving, for instance, solvent evaporation [45], templates [46], and molecular linkers [15, 47].

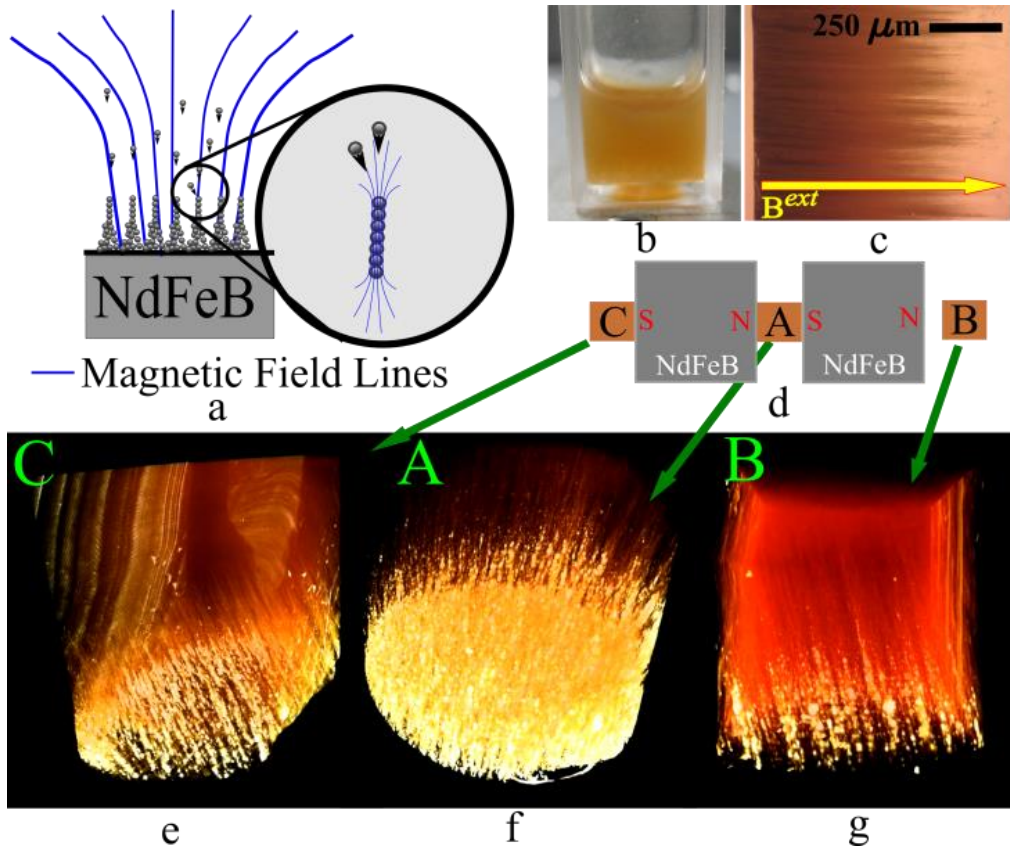


Figure 2-1 (a) Magnetic nanoparticles dispersed in a fluid move towards locations that experience a stronger magnetic field. The particles initially agglomerate into clusters. Strong dipole-dipole interactions amongst clusters enable self-assembly into filaments. (b) The nanoparticles are initially uniformly dispersed in liquid PDMS prepolymer. (c) The polymer is cured while the system experiences an externally imposed magnetic field. The polymer matrix preserves the shapes of the self-assembled structures when the field is removed. (d) The structure morphology can be controlled by varying $|B^{ext}|$ and $|dB^{ext}/dx|$, as shown for three experimental conditions obtained by three curing positions relative to a system of two NdFeB permanent magnets. The values obtained, labeled A, B and C, are listed in Table 1. (e-g) Three-dimensional images obtained by X-Ray MicroCT reconstructions show variations in the microstructure geometry. Reproduced from Ref. [48] by permission of The Royal Society of Chemistry.

MNPs dispersed in polymer melts have recently enabled the development of composites that contain self-assembled magnetic microstructure [27-29]. However, the focus of the few reported investigations has been on the influence of the microstructure on mechanical [27, 28] and magnetic [29] properties. These studies are limited to applications of a homogeneous magnetic field, producing linear self-assembled chains that are dispersed throughout the polymer matrix. The presence of a gradient in the field enforces magnetophoretic transport. This allows

controlled localization and structural patterning, as observed in ferrofluids [44]. A more complete understanding of the dependence of microstructure geometry on the magnetic field is needed to exploit the influence of heterogeneities on material properties of a nanocomposite.

Here we study how the microstructure geometry can be controlled in a soft polymer by using an external magnetic field, thus demonstrating the influence of both \mathbf{B}^{ext} and $d\mathbf{B}^{ext}/dx$, which together impose magnetic control during self-assembly. This form of magnetophoretic transport is capable of producing high particle concentrations near a substrate. We provide the first direct nanoscale visualization of such dipolar self-assembly outside of thin films. The TEM images provide confidence in our analysis that MNPs agglomerate in polymeric dispersions through a combination of isotropic van der Waal's forces and anisotropic dipolar interactions.

2.2 Materials and methods

2.2.1 Generation of composite microstructure

This involved the magnetophoretic transport and self-assembly of MNPs in the liquid precursor to PDMS. The magnetite nanoparticles (EMG 1400, Ferrotec Inc.) were first dispersed in tetrahydrofuran (THF) by ultrasonic treatment in a water bath (Branson 2510) for 15 minutes. Subsequently, PDMS (SylgardTM 184, Dow Corning) was added to the dispersion (1:1 w/w PDMS to THF), stirred vigorously and sonicated for another 15 minutes. The PDMS cross-linker was then added to the dispersion (10 % w/w cross-linker to PDMS). The resulting dispersion was immediately exposed to the externally applied magnetic field \mathbf{B}^{ext} for 30 minutes at room temperature. Bulk of MNPs were observed to settle on the cuvette wall closest to the nearest magnet within this time. The dispersion was then heated at 45 °C for 12 hours while still exposed to \mathbf{B}^{ext} . The THF was lost by evaporation as observed by a reduction in the volume of the

dispersion, and solid PDMS was obtained. Experiments were conducted for three different particle concentrations ψ (w/w, MNP to PDMS).

2.2.2 Sample preparation for X-Ray computed tomography

The cured PDMS was cut into ~1 mm cubes. One of the sides of the cube was the substrate S at which the self-assembled structures were formed. This is the polymer surface adjacent to the wall of the cuvette facing the nearest magnet. The specimens were individually mounted on a sample holder with S facing up and imaged using XRADIA MicroXCT-400 with a 20 \times objective. 360 projection images were obtained spanning a total rotation of 179° about a vertical axis close to the center of the sample. The volume data was reconstructed from these images using proprietary software from XRADIA.

2.2.3 Sample preparation for TEM

The PDMS blocks containing the self-assembled structures were trimmed to create a pointed edge at the surface S . Each sample was then sliced using a microtome (RMC Products CR-X Cryosectioning system) at -170 °C. Individual slices were ~100 nm in thickness and perpendicular to S . This allowed imaging of the root of the self-assembled microstructure. The slices were subsequently transferred on to TEM grids and imaged using Philips EM420.

2.2.4 Magnetic field setup

The setup for magnetic field comprised of a pair of 1" cube NdFeB magnets (K & J Magnetics, Inc., grade N-52), shown in the schematic in Figure 2-1 (d), placed 12.7 mm apart. Magnetic nanoparticles dispersed in diluted prepolymer were cured in plastic cuvettes at three positions relative to these magnets, labeled A, B and C. Numerical values for \mathbf{B}^{ext} are obtained from the Finite Element Method Magnetics (FEMM) software at the substrate posed by the cuvette walls.

Table 2-1 Magnetic field $|\mathbf{B}^{ext}|$ and its gradient $|d\mathbf{B}^{ext}/dx|$ for the three different configurations shown in Figure 1 (d). The values are obtained using the Finite Element Method Magnetics software and verified by a Hall Probe.

	Field ($ \mathbf{B}^{ext} $) (T)	Gradient ($ d\mathbf{B}^{ext}/dx $) (T cm^{-1})
A	0.6974	0.1217
B	0.4090	0.2435
C	0.5093	0.2742

Values at specific points were confirmed by using a Hall probe magnetometer. Values of $d\mathbf{B}^{ext}/dx$ were obtained by a central difference scheme. A map of these values is shown in Figure 2-2. The positions used to determine the magnetic control variables are separated from the surface of the magnet by the thickness of cuvette walls and listed in Table 2-1.

2.3 Scaling analysis

2.3.1 Relating magnetophoretic velocity to particle size

Each dipole encountered herein is an MNP cluster of submicron length. Inertia thus plays a negligible role in its dynamics. Magnetophoretic force is balanced only by fluid drag. Drag on a spherical particle is given by Stokes' formulation,

$$\mathbf{F} = -6\pi\mu a \mathbf{U}, \quad (2.1)$$

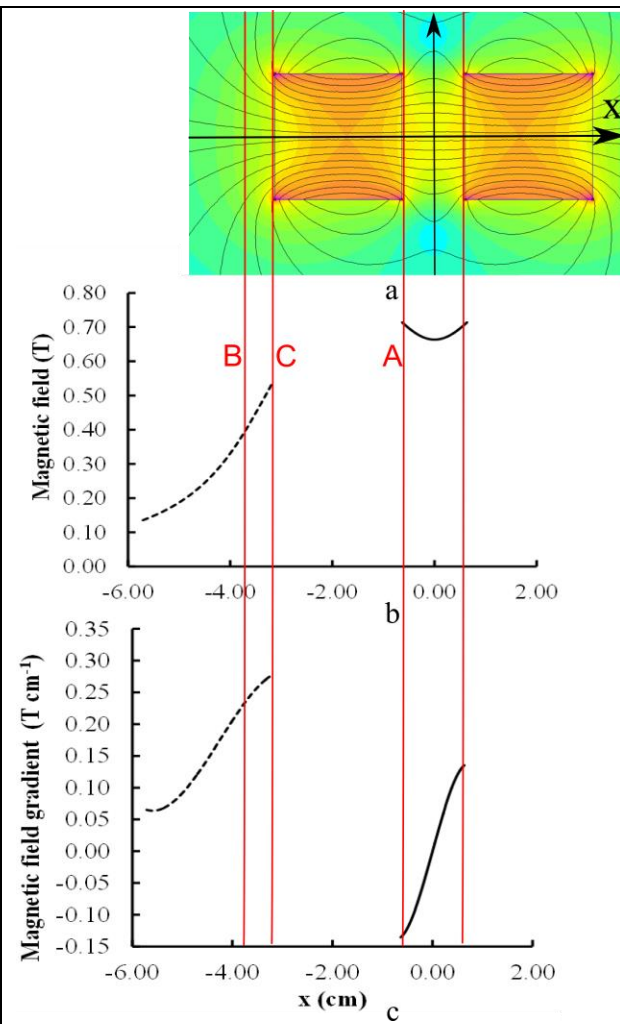


Figure 2-2 (a) Map of magnetic field strength $|\mathbf{B}^{ext}|$ with values of the (b) x -components of \mathbf{B}^{ext} , and (c) its gradient $d\mathbf{B}^{ext}/dx$ determined from FEMM software. Reproduced from Ref. [48] by permission of The Royal Society of Chemistry.

where a denotes the particle radius and μ the dynamic viscosity of the liquid dispersant. For nonspherical particles, the drag $F \sim \mu a U$ where a is an estimate of the particle size. This equals the magnetophoretic force, i.e.,

$$|(\mathbf{m} \cdot \nabla) \mathbf{B}| \sim \mu a U. \quad (2.2)$$

The magnetic moment $|\mathbf{m}| \sim a^3 M_s$ where M_s is the saturation magnetization of the constituent material. Thus, it follows from Eq. 2.2 that the magnetophoretic speed of a particle scales as

$$U \sim a^2. \quad (2.3)$$

2.3.2 Relating structure anisotropy to magnetic field

A filament with a large height h and a small base area is considered highly anisotropic herein. The anisotropy metric ϑ , a representative measure of the ‘cone angle’ of a filament, is introduced later to quantify this feature. This subsection relates the dependence of such a metric on the magnetic control variables. A lower value of ϑ indicates higher shape anisotropy. Its lowest value is achieved for a single chain of particles and represents the highest conceivable shape anisotropy.

The source of microstructure anisotropy is the long range orientation of the dipole-dipole bonds in the direction of the magnetic field. A larger $|\mathbf{B}^{ext}|$ thus induces greater alignment of such bonds and thus a smaller ϑ . However, this observation is not universal. In reality, the bonds are directed along the local direction of the magnetic field. The above statement is valid only when $|\mathbf{B}^{ext}| \sim |\mathbf{B}^{dip}|$, the field experienced by one dipole due to neighboring dipoles. In such a situation, the competition between the two produces a discernible difference in the direction of the local magnetic field and thus structure anisotropy. A saturation value of $|\mathbf{B}^{ext}|$ as a control

for ϑ is observed when $|\mathbf{B}^{ext}| \gg |\mathbf{B}^{dip}|$. Also, for a nonhomogeneous field, the magnetophoretic force due to the magnetic field gradient influences the anisotropy. In order to analyze the dependence of microstructure anisotropy on the magnetic control variables $|\mathbf{B}^{ext}|$ and $|d\mathbf{B}^{ext}/dx|$, we consider a simple system comprised of the two dipoles shown in Figure 2-3.

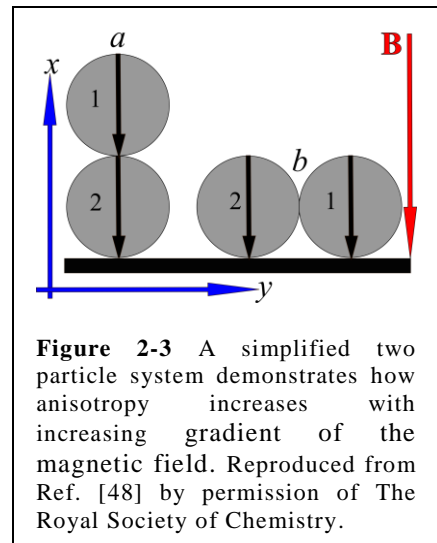


Figure 2-3 A simplified two particle system demonstrates how anisotropy increases with increasing gradient of the magnetic field. Reproduced from Ref. [48] by permission of The Royal Society of Chemistry.

The said saturation value of $|\mathbf{B}^{ext}|$ can be estimated by comparing it with $|\mathbf{B}^{dip}|$. For the configuration in Figure 2-3 (b), the magnetic field at the center of dipole 1 due to the presence of its neighbor, dipole 2, is given by $\mathbf{B}_1^{dip} = \mu_0 M_s / 24 \mathbf{e}_x$. For magnetite, $M_s = 446 \times 10^3 \text{ Am}^{-1}$ leads to $|\mathbf{B}_1^{dip}| \sim 0.023 \text{ T}$, which is an order of magnitude smaller than the applied value of $|\mathbf{B}^{ext}|$ in our experiments. As \mathbf{B}^{ext} is directed along $(-x)$, the net magnetic field experienced by dipole 1 is also similarly directed towards the externally imposed field. This shows that for magnetite nanoparticles and the values of $|\mathbf{B}^{ext}|$ used in our setup, all dipoles in the system encounter a local magnetic field that is directed along $(-x)$. The alignment effect of $|\mathbf{B}^{ext}|$ is thus well past saturation, and ϑ is not expected to depend on $|\mathbf{B}^{ext}|$. This is confirmed in Section 2.4

Corresponding to our experimental setup described in Figures 2-1 and 2-2, we may assume magnetic field on the x -axis to be $\mathbf{B}^{ext} = -B(x)\mathbf{e}_x$. The total potential energy of the system

$$U_{tot} = -\sum_i \mathbf{m}_i \cdot \mathbf{B}^{ext}(\mathbf{r}_i) + \frac{\mu_0}{4\pi} \left(\frac{\mathbf{m}_1 \cdot \mathbf{m}_2}{r^3} - \frac{3(\mathbf{m}_1 \cdot \mathbf{r})(\mathbf{m}_2 \cdot \mathbf{r})}{r^5} \right), \quad (2.4)$$

where \mathbf{r} denotes the position vector of one dipole relative to the other, \mathbf{r}_i the position vector about the i^{th} particle about a common origin. Thus, the potential energies for cases (a) and (b) in Figure 2-3 are, respectively,

$$U_{\text{tot}}^a = -m(B(a) + B(3a)) - \frac{\mu_0}{4\pi} \frac{m^2}{4a^3}, \text{ and} \quad (2.5)$$

$$U_{\text{tot}}^b = -2mB(a) + \frac{\mu_0}{4\pi} \frac{m^2}{8a^3}. \quad (2.6)$$

Here, a denotes the radius of the dipolar particle. The difference between these two values dictates whether anisotropic chains are formed along the magnetic field, or all nanoparticles are pulled towards the substrate. This difference,

$$\Delta U_{\text{tot}} = m(B(a) - B(3a)) - \frac{\mu_0}{4\pi} \frac{3m^2}{8a^3}. \quad (2.7)$$

A two-particle system attains a configuration where both particles lie on the substrate, i.e., case (b), when $\Delta U_{\text{tot}} > 0$. Approximating $B(a) - B(3a) \sim |dB/dx|(2a)$, the criteria for this transition is,

$$\frac{16a|dB/dx|}{\mu_0 M_s} > 1. \quad (2.8)$$

Thus, a larger magnitude of the magnetic field gradient renders a smaller anisotropy in the resultant structure, i.e., a larger ϑ . In more complicated systems that comprise several dipoles, such simplified equations cannot be construed. However, the dimensionless number obtained from Equation 2.8,

$$\Pi = \frac{a | dB / dx |}{\mu_0 M_s} \quad (2.9)$$

provides guidance about the anisotropy of the system. Smaller values of Π lead to higher anisotropy in the microstructure, i.e., a lower value of ϑ .

2.4 Results and discussions

The geometry of self-assembled microstructure can be controlled by varying \mathbf{B}^{ext} and $d\mathbf{B}^{ext} / dx$ using a set of permanent magnets. Here, we use two NdFeB magnets for the purpose, illustrated in Figure 2-1 (d). MNP dispersions in diluted PDMS prepolymer are cured at three spatial positions relative to the magnet pair, leading to the three different values of \mathbf{B}^{ext} and $d\mathbf{B}^{ext} / dx$ listed in Table 2-1. Quantitative aspects of the microstructure geometry are correlated with these magnetic control variables.

A very dilute dispersion aids a controlled magnetophoretic self-assembly process by significantly diminishing the irreversible and uncontrolled agglomeration of a large number of particles [11, 49]. However, at low concentrations, magnetostatic interactions are insignificant due to the large separation between adjacent particles. The observed self-assembly is thus minimal [29, 50]. Beginning from a sparse dispersion, we use gradual and controlled magnetophoretic transport of MNPs towards a wall of the cuvette containing the dispersion. This transport is enabled by the force induced on each dipole due to the gradient in the magnetic field, producing the filament-like microstructure shown in Figure 2-1 (e-g).

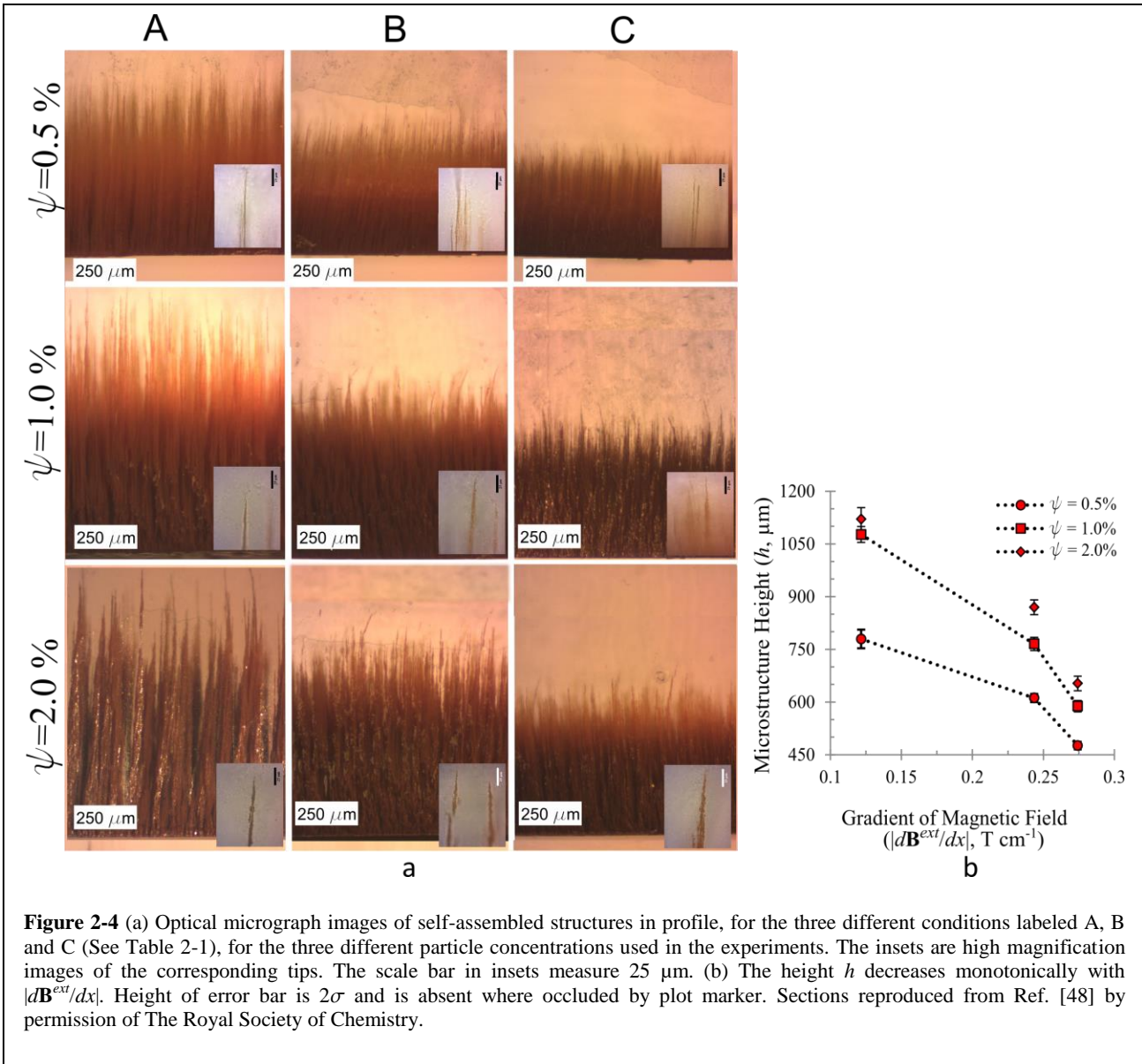
Control over geometry of the microstructure is investigated by measuring the (1) the height h of the self-assembled filaments, and, (2) the fraction of the substrate area covered by the

microstructure, denoted by ξ . Optical micrographs of the microstructure are analyzed for such measurements.

2.4.1 Dynamics of a magnetic nanoparticle

The self-assembled microstructure geometry depends on both \mathbf{B}^{ext} and $d\mathbf{B}^{ext}/dx$. Establishing magnetic control over the self-assembled structure requires that the dynamics of interacting dipoles in a magnetic field be examined. The influence of a magnetic field on the dispersed MNPs is described by the Zeeman energy of a point dipole in a field, $U = -\mathbf{m} \cdot \mathbf{B}$. Each dipole experiences a force $\mathbf{F} = (\mathbf{m} \cdot \nabla) \mathbf{B}$ that pulls the particle towards regions where the magnetic field is stronger, and a torque $\tau = \mathbf{m} \times \mathbf{B}$, which aligns the dipole with the field direction. The magnetic field experienced by a dipole \mathbf{m} is given by $\mathbf{B} = \mathbf{B}^{ext} + \mathbf{B}^{dip}$. Hence, magnetostatic self-assembly occurs through interplay between (1) interparticle dipole-dipole interactions (DDI), and (2) the dipole-field interactions (DFI).

\mathbf{B}^{ext} is the only external control variable, and its collective influence on participating dipoles is summarized thus. (1) A dipole attaches to another so that their individual moments point along the line joining their centers. (2) The dipole-dipole ‘bonds’ are oriented along the local direction of \mathbf{B} , the most simplified manifestation of which is the formation of linear chains in the direction of \mathbf{B}^{ext} . (3) Each dipole experiences a force in the direction of strengthening magnetic field, resulting in magnetophoretic transport in that direction. Here, a dipole is not an individual MNP but is rather formed as an MNP cluster [41] which is discussed later.



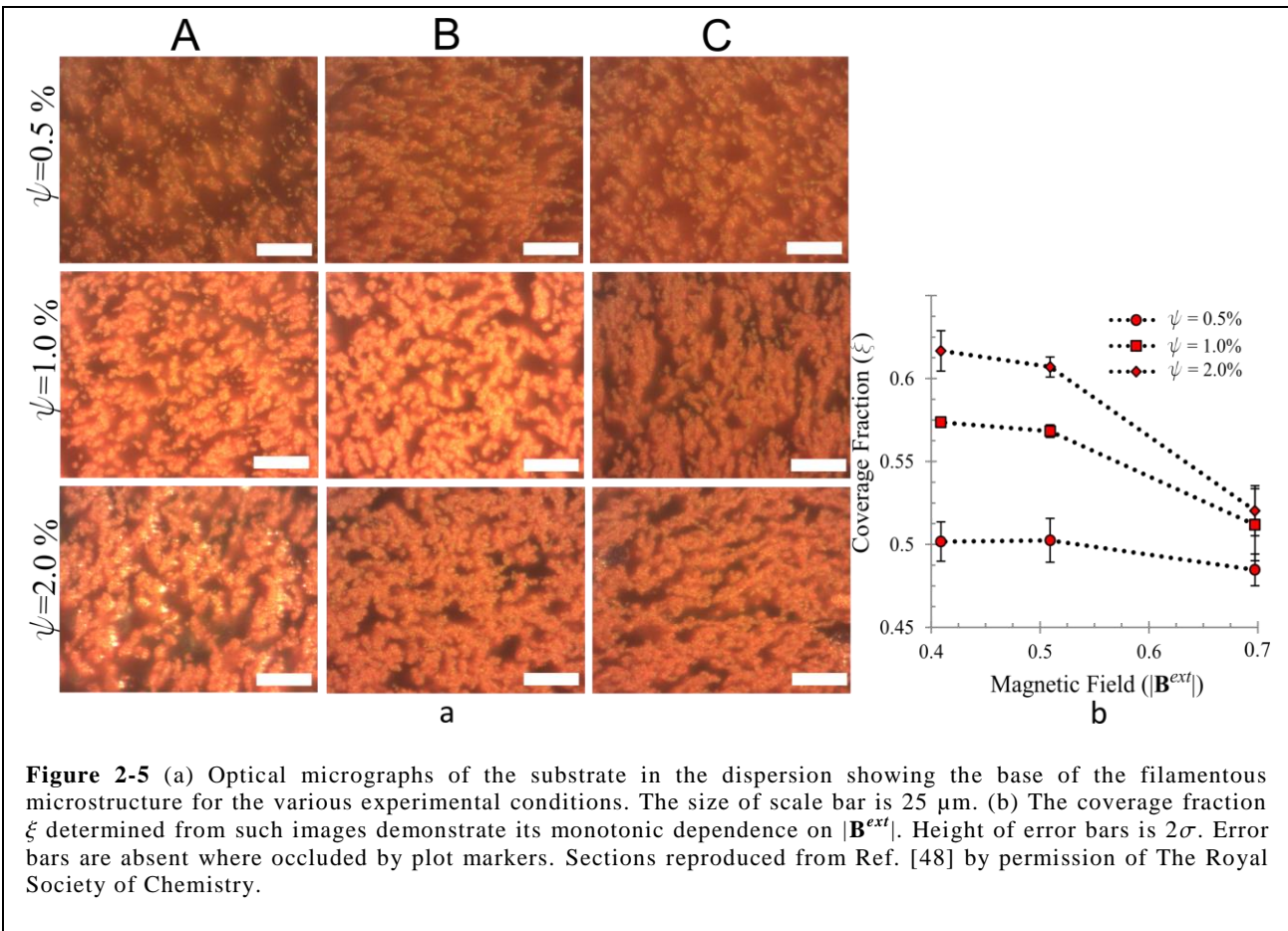
2.4.2 Height of microstructure (h)

Considering the dynamics discussed above, a control strategy for h follows intuitively. Consider an MNP cluster approaching a self-assembled structure, as shown in Figure 2-1 (a). The net force on it is directed along the gradient of the local magnetic field. Since $\mathbf{B} = \mathbf{B}^{\text{ext}} + \mathbf{B}^{\text{dip}}$, this net force is the result of two competing components, i.e., the force due to \mathbf{B}^{dip} (F_{DDI}) and that due to \mathbf{B}^{ext} (F_{DFI}). When $F_{DFI} >> F_{DDI}$, an MNP cluster moves towards the substrate instead of joining

the terminus of a preexisting self-assembled structure. As $F_{DFI} \sim |d\mathbf{B}^{ext}/dx|$, h decreases monotonically with $|d\mathbf{B}^{ext}/dx|$, as shown in Figure 2-4 (b). Similar observations can be made by examining the experimental configurations for previous experiments on ferrofluids [44], although for a homogeneous field the length of a self-assembled chain increases with $|\mathbf{B}^{ext}|$ [27]. Further, in Figure 2-4 (b), h increases monotonically with ψ because of the increase in the number of dipolar clusters available for microstructure generation.

2.4.3 Substrate coverage fraction (ξ)

Observed variations in the coverage fraction ξ are not intuitive as that for h . A larger $|d\mathbf{B}^{ext}/dx|$ should lead to smaller ξ as more particles are drawn to the substrate by the larger F_{DFI} . This is however not observed. Figure 2-5 (b) instead shows variations that correlate monotonically with $|\mathbf{B}^{ext}|$ but not with $|d\mathbf{B}^{ext}/dx|$. The dynamics of microstructure formation can explain this. By Stokes' formulation, the magnetophoretic velocity of each dipole towards the substrate $U \sim a^2$ from Equation 2.3 and is very sensitive to cluster size. Consequently, the largest clusters reach the substrate much sooner than smaller ones. These clusters are restrained on the substrate by the magnetic field and behave as a two-dimensional gas of repulsive dipoles [43]. Due to the large structure sizes, the associated inter-cluster dipolar interactions are strong. Such interactions are mainly repulsive as the magnetic moments of the clusters are parallel to each other and to \mathbf{B}^{ext} . These seed clusters form the nucleation sites for the smaller clusters that arrive later. The repulsion, hence the separation distance, increases with increasing $|\mathbf{B}^{ext}|$ due to a greater alignment of the net magnetization of each dipole with \mathbf{B}^{ext} . Consequently, the seeding clusters are more sparsely distributed at larger $|\mathbf{B}^{ext}|$ values, leading to lower ξ , which is evident from Figures 2-5.



2.4.4 Structure anisotropy (ϑ)

The structure anisotropy is not governed solely by the ability of the magnetic field to orient dipoles and thereby enhance intercluster repulsion as would be expected for homogeneous magnetic fields [27], but also by the magnetophoretic force experienced by each MNP due to the field gradient. A smaller gradient of the magnetic field promotes filament formation, while a very large gradient will cause all clusters to form a uniform coating on the substrate. To establish this, we consider a

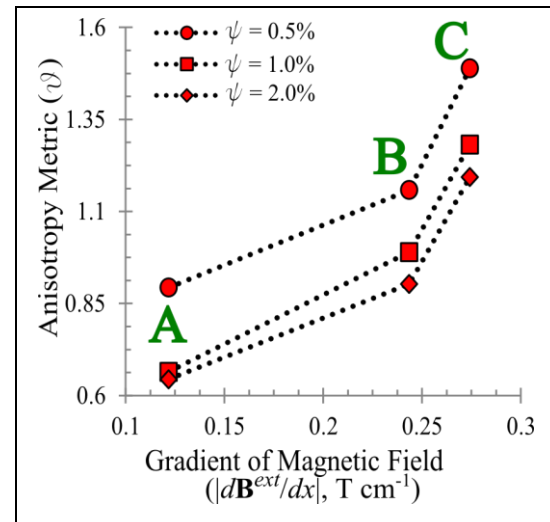


Figure 2-6 The anisotropy metric ϑ increases monotonically with the gradient of the external magnetic field. Reproduced from Ref. [48] by permission of The Royal Society of Chemistry.

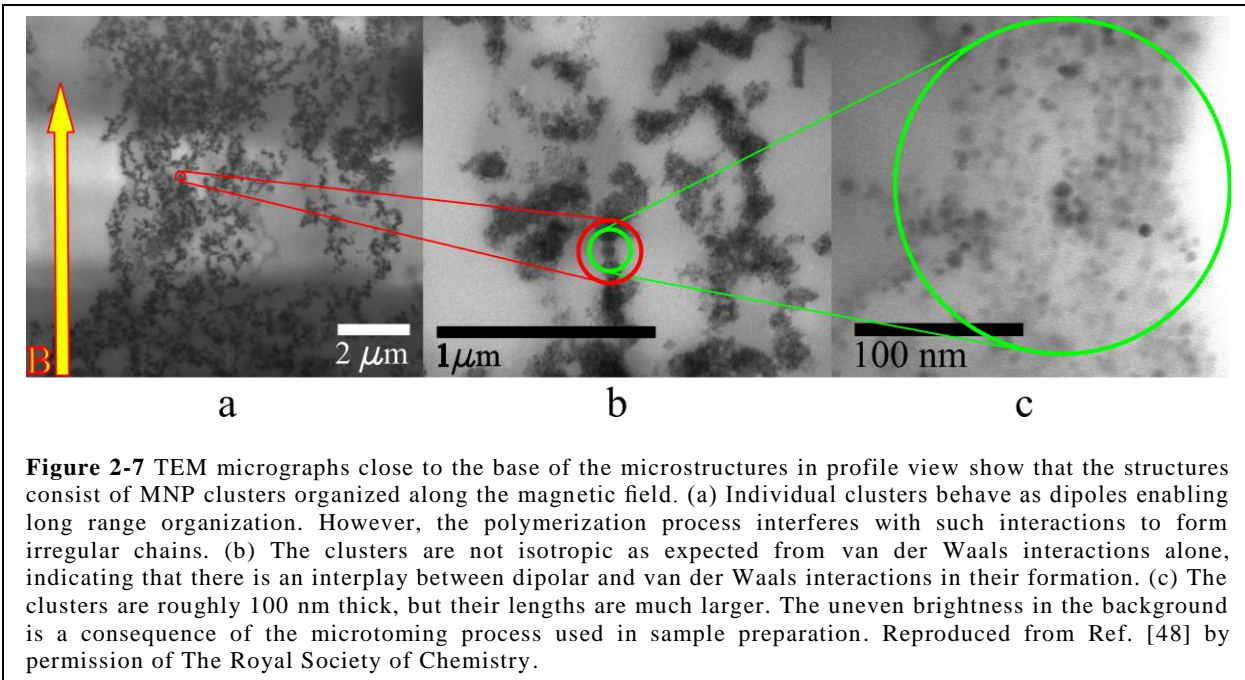
metric for anisotropy based on a length associated with the coverage fraction, $\Lambda = \sqrt{\xi}$. The anisotropy metric

$$\vartheta = \Lambda / h, \quad (2.10)$$

is a measure of the tip angle of the filaments where smaller ϑ corresponds to higher anisotropy. A simple analysis of the dynamics of two dipoles provides an estimate of the dependence of ϑ on the control variables \mathbf{B}^{ext} and $d\mathbf{B}^{ext} / dx$ as discussed in Section 2.3.2. Comparing the relative magnitudes of these variables, the dimensionless parameter Π defined in Equation 2.9 serves to describe the anisotropy in these structures. With all other factors constant among the various experimental cases herein, ϑ should increase monotonically with $|d\mathbf{B}^{ext} / dx|$, i.e., increasing Π , as observed in Figure 2-6.

2.4.5 Anisotropy in clusters of nanoparticles

The agglomeration of interacting dipolar particles has been the subject of several theoretical and computational studies [51, 52]. Recently, direct observations of MNP agglomerates in vitrified liquid films have demonstrated that increasing the particle radius, thus the magnetic moment \mathbf{m} , causes the dominant forces for agglomeration to transition from van Der Waals interactions to dipolar interactions so that the formed clusters transition from being isotropic to anisotropic [10, 49]. Tuning the particle size in a system is difficult to achieve, specially for industrial processes that will make use of commercially available MNPs. The value of $|\mathbf{m}|$ for most commonly used magnetite MNPs is too small to produce significant dipolar interactions [49]. However, isotropic agglomeration by van der Waals interactions leads to clusters that possess a higher resultant \mathbf{m} , allowing these to undergo dipolar-interaction dominated self-assembly [27, 41]. The dipolar parameter λ [41], defined as the ratio of dipolar interaction potential energy to the energy of thermal fluctuations, is very small for the magnetite



nanoparticles of particle radius $a \sim 5$ nm (EMG 1400, Ferrotec, Inc.) that are used herein. Consequently, the dipolar interactions between isolated particle-pairs are insignificant. As the particles become more concentrated close to the substrate, van der Waals dominated inter-particle interactions lead to the formation of clusters [41].

Figure 2-7 (a) shows that each structure is comprised of several smaller clusters of different shapes, sizes and orientations. Figure 2-7 (b) shows that these clusters are anisotropic, differing significantly from the isotropic clusters formed by van der Waals forces observed otherwise [41, 49]. This indicates interplay of both dipolar and van der Waals interactions in the formation of such clusters. The dominance of the dipolar interactions in inter-cluster ‘bonding’ is clear in Figure 2-7 (a) by observing the long-range global order that is enforced in the overall direction of \mathbf{B}^{ext} . This is also apparent from the formation of the filamentous microstructure, which is highly anisotropic. The complexity of the structures is a possible consequence of the subsequent evaporation of the diluent (tetrahydrofuran) from the prepolymer and the onset of

cross-linking reactions. The wide variations in the shapes of the structures are attributed to strong thermal fluctuations, which are exaggerated by the relatively high temperature ($\sim 45^\circ\text{C}$) used to cure the polymer.

2.5 Conclusions

We demonstrate a method to produce a filamentous magnetic microstructure on a substrate in a soft-polymer matrix through the self-assembly of magnetic nanoparticles. Geometry of the microstructure depends on the externally applied magnetic field \mathbf{B}^{ext} applied during the cross-linking process. Magnetic control is enabled through two variables, i.e., \mathbf{B}_{ext} and $d\mathbf{B}_{\text{ext}}/dx$. The dependence of structural metrics of the microstructure, such as height h , coverage area ξ and structure anisotropy ϑ , on these magnetic control variables are explained by examining the mechanics of magnetophoretic transport and the self-assembly of magnetic dipoles dispersed in a liquid. We demonstrate that these dipoles are clusters that are formed through the interplay between the van der Waals and dipolar interactions at the length scale of individual particles. Interactions between adjacent clusters are primarily dipolar, enabling magnetic control.

2.6 Acknowledgements

We thank Mr. Sourav Mishra and Prof. Ge Wang of the Virginia Tech Wake Forest University School of Biomedical Engineering and Sciences for access to the X-Ray CT facility and associated user training supported by the NSF Major Research Instrumentation grant CMMI0923297, and Mr. Steve McCartney of the ICTAS Nanoscale Characterization and Fabrication Facility at Virginia Tech for TEM sample preparation and imaging.

3. Properties of nanoparticle ensembles: Anisotropy enhancement by dipolar interactions²

Inter-particle magnetostatic coupling of dipole moments has a significant influence on the magnetic properties of densely packed nanoparticle ensembles. Consequently, shape and size of an ensemble has a bearing on its bulk magnetic properties. We investigate such an effect in a linear chain of magnetic nanoparticles. In this configuration, when easy axes of the particles are aligned with the chain direction, magnetostatic coupling enhances the potential barrier for magnetization reversal. This is considered an increase in effective magnetocrystalline anisotropy. The frequency of thermally driven magnetization reversals is thus significantly reduced and the ensemble may transition from superparamagnetic to ferromagnetic behavior. To investigate this effect, we simulate an idealized chain in a two-particle system. We observe that when thermal effects are significant, magnetization reversals do not necessarily occur along the energetically cheapest paths. The effective potential barrier is thus much higher than saddle points in the energy map considered by theoretical models. We also observe the possibility of using a universal attempt frequency in a modified Néel-Arrhenius relation. We extend to outline key features for the parametric design of magnetization stabilization by making use of the dipolar interactions.

3.1 Background and motivation

Magnetic nanoparticles (MNPs) are used for many emerging applications, ranging from information storage to medicine. Most of them organize the MNPs into patterned structures to tailor bulk material properties. Consequently, a wide array of self-assembly (SA) methods have

²Adapted from S. Ghosh and I. K. Puri, "Anisotropy Enhancement in Linear Chains of Magnetic Nanoparticles by Dipolar Interactions," *In preparation*, 2013

been investigated, exploiting different types of inter-particle interactions [7]. Inter-particle dipolar interactions are inherent to MNPs. Their use in self-assembly eliminates the need for the sophisticated routes of other techniques, e.g., solvent evaporation [45], templates [46], and molecular linkers [15, 47]. Instead, dipolar interactions enable control over the microstructure geometry by employing an externally applied magnetic field. The inter-particle ‘bond’ between two neighboring dipoles aligns with the direction of the field and serves as the primary driver in such organization [48]. A simple example is a linear filament along the field direction, as shown in Figure 3-1 (a, b). Dipolar interactions play a significant role in the magnetic behavior of such anisotropic closely packed ensembles and can be used as a tool to engineer their magnetic properties. We address one such possibility, i.e., the enhancement of effective magnetocrystalline anisotropy by stabilizing the magnetic moments in a linear chain of superparamagnetic MNPs.

Good control over the SA of MNPs requires a stable dispersion in which magnetostatic interactions among neighboring particles are negligible. Dilute dispersions of superparamagnetic particles are used for this purpose since their low magnetocrystalline anisotropy enables frequent thermally driven magnetization reversals rendering a net zero magnetization [53-55]. The low anisotropy of the particles also allows for substantial flexibility in the motion of their magnetic moment. When two particles come in proximity, dipolar interactions between their magnetic moments become a significant driver of the collective magnetization dynamics.

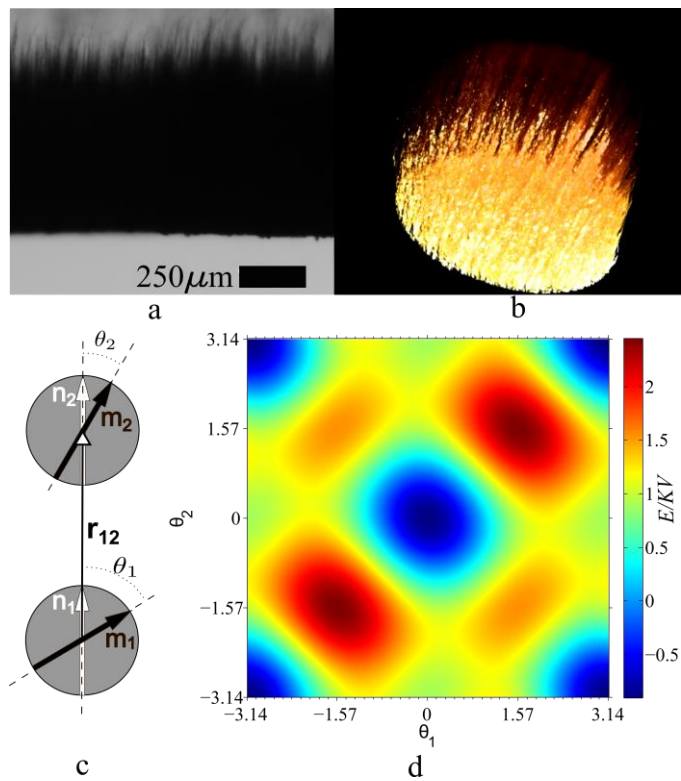


Figure 3-1 The potential barrier for magnetization reversal in an anisotropic ensemble of MNPs is higher than that in an isolated particle due to magnetostatic coupling. Images of the self-assembled ensembles of magnetite nanoparticles in PDMS matrix obtained with (a) an optical microscope, and (b) X-Ray computed tomography show pillar-like structures consisting of chains that are aligned with the direction of the imposed field. The ~750 μm tall pillars taper off from a ~5 μm thick base and are highly anisotropic. (c) A system of two MNPs is the simplest system with which to study the effect of dipolar interactions in anisotropic structures. Here, the easy axes \mathbf{n}_1 and \mathbf{n}_2 lie along the straight line joining the centers. The magnetic moments \mathbf{m}_1 and \mathbf{m}_2 can rotate with respect to the particles due to the low magnetocrystalline anisotropy. (d) The total potential energy $E = E_{\text{dip}} + E_a$ of this system reaches a minimum value when $\theta = 0, \pm\pi$, i.e., the moments are parallel to each other as well as to the line joining the centers of the two particles. Note that the energy map is a planar projection of a four dimensional space containing all possible stable equilibria.

The dynamics of the magnetic moments in a system of single domain MNPs are governed by the potential barrier that separates the stable equilibria of the moments, E_b . For isolated single domain MNPs that lie in a zero magnetic field, this barrier is imposed solely by the magnetocrystalline anisotropy. When multiple particles are involved, inter-particle dipolar interactions influence the energy map, as described in Figure 3-1 (d). The dynamics of the magnetic moments, hence E_b define the magnetic properties of an ensemble of MNPs. Therefore, the magnetic properties of a microstructure produced through the SA of superparamagnetic particles can be engineered by controlling dipolar interactions. The simplest manifestation of this

is observed in a two-particle system, which has formed the basis of idealized investigations [26, 32, 56-59]. By appropriately selecting the material properties and the angle between the easy axes of participating MNPs (popularly called the bond angle β [26, 57]), the potential barrier for magnetization reversals can be either enhanced [60, 61] or reduced [32]. While increasing E_b provides a route that transitions behavior from superparamagnetic to ferromagnetic and consequently enhances its blocking temperature, its reduction is useful for designing low coercivity recording media.

Herein we investigate the stabilizing influence of dipolar interactions against thermally activated magnetization reversals, i.e., the situation where dipolar interactions enhance E_b . Initially, we consider a two-particle system where the magnetic easy axes (\mathbf{n}_1 and \mathbf{n}_2) are aligned with the line joining their centers (\mathbf{r}_{12}), as shown in Figure 3-1 (c). This configuration enhances E_b [26]. The equilibria in such a system occur when both magnetic moments \mathbf{m}_1 and \mathbf{m}_2 are parallel to (1) each other and (2) to the line joining their centers [56], as seen in the energy map in Figure 3-1 (d).

Micromagnetics simulations using the stochastic Landau-Lifshitz-Gilbert (LLG) equation [62, 63] can be used to determine the magnetic properties of a system of MNPs by simulating the dynamics of the magnetic moment of each participating MNP [64-66]. This equation has been used to study the influence of dipolar coupling on thermally driven magnetization reversals in two-particle systems [58, 59]. We adopt this method to observe the magnetization dynamics when the externally applied magnetic field is zero. The simulations enable the calculation of E_b through the Néel-Arrhenius relation [67], which we compare to theoretical estimates for a two-particle system with $\beta=0$ [26]. Our observations show that magnetization reversals do not necessarily occur along the most energetically economical path. This is consistent with earlier

reports that the maximum energy during a reversal exceeds the theoretical barriers for a field-induced reversal when thermal fluctuations are absent [58, 68]. An effective potential barrier can thus never be determined from the saddle points in the energy map, as suggested in Ref. [26]. However, analytical formulations of this saddle point provide an effective anisotropy constant K_{eff} that is comparable to the one obtained from analyzing the simulation data for the two-particle system. Our empirical observations indicate that the Néel-Arrhenius relations can be employed through a universal attempt frequency f_0 , providing a motivation for future theoretical study. Subsequently, we introduce a parametric design strategy to engineer magnetization stabilization using dipolar interactions to assist material and process variable selection for a wide array of emerging applications using SA of MNPs.

3.2 Theory

Thermally driven magnetization reversal is described by the Néel-Arrhenius relation for reversal frequency [67],

$$f = f_0 \exp\left(-\frac{E_b}{k_B T}\right), \quad (3.1)$$

where E_b denotes the potential barrier for magnetization reversal and $f_0 \sim 10^9 - 10^{11}$ Hz is the attempt frequency. The nomenclature used herein is summarized in Table 3-1. Equation (3.1) is generally valid for large barriers i.e., $E_b/k_B T \geq 5-10$ [69], and f_0 varies with factors such as the external field, dipolar interaction strength in a two-particle system, as well as the damping constant [58, 65]. An alternate form $f = f_0 \exp(-KV^{0.979}/k_B T)$ has also been proposed from micromagnetics simulations of isolated MNPs, which is valid over a wider $E_b/k_B T$ range [65].

Table 3-1 Nomenclature

Symbol	Quantity	Dimensions	Units
a	Particle radius	[L]	m
\mathbf{B}	Magnetic Field	[M][T] ² [I] ⁻¹	T
\mathbf{e}	Non-dimensional magnetic moment defined as $\mathbf{e} = \mathbf{m}/ \mathbf{m} $	-	dimensionless
f	Magnetization reversal frequency	[T] ⁻¹	Hz
f_0	Attempt frequency	[T] ⁻¹	Hz
E	Potential energy of a system of magnetic nanoparticles	[M][L] ² [T] ⁻²	J
E_{an}	Anisotropy energy	[M][L] ² [T] ⁻²	J
E_b	Energy barrier for magnetization reversal	[M][L] ² [T] ⁻²	J
k_B	Boltzmann constant	[M][L] ² [T] ⁻² [θ] ⁻¹	J K ⁻¹
k_{int}	Dipolar interaction strength defined by Equation (5)	-	dimensionless
K	Magnetocrystalline anisotropy constant defined by Equation (7)	[M][L] ⁻¹ [T] ⁻²	J m ⁻³
K_{eff}	Effective anisotropy constant	[M][L] ⁻¹ [T] ⁻²	J m ⁻³
\mathbf{m}	Magnetic moment	[L] ² [I]	A m ⁻²
M_s	Saturation Magnetization	[L] ⁻¹ [I]	A m ⁻¹
\mathbf{n}	Direction of easy axis	-	dimensionless
r	Inter-particle distance	[L]	m
T	Temperature	[θ]	K
V	Particle volume	[L] ³	m ³
γ	Gyromagnetic constant	[M] ⁻¹ [T] ¹ [I] ¹	T ⁻¹ s ⁻¹
λ	Damping Constant	-	dimensionless
μ_0	Permeability of free space	[M][L][T] ⁻² [I] ⁻²	N A ⁻²
τ_m	Measurement time	[T]	s

The investigation of magnetization reversals requires an accurate estimate of the potential barrier, hence examining the energy map of the system is necessary. The magnetic moment \mathbf{m} of an MNP has an inherent predilection to align itself with the magnetocrystalline easy-axes, which are the preferred crystallographic directions fixed to the MNP. For simplicity, we consider the case of uniaxial anisotropy, i.e., each MNP possesses a single easy axis, \mathbf{n} . Misalignment between \mathbf{m}_i and \mathbf{n}_i of the i^{th} particle in a system comes at the cost of the anisotropy energy, i.e.,

$$E_a^i = -\frac{KV}{|\mathbf{m}_i|^2} (\mathbf{m}_i \cdot \mathbf{n}_i)^2, \quad (3.2)$$

where K denotes the magnetocrystalline anisotropy constant, and V the particle volume. This energy is solely responsible for driving the dynamics of \mathbf{m} for an isolated particle that lies in a zero field. However, when neighboring MNPs are present, the i^{th} MNP in a multi-particle system encounters the magnetic field

$$\mathbf{B}_i^{\text{dip}} = \frac{\mu_0}{4\pi} \sum_{j \neq i} \left(\frac{3\mathbf{r}_{ij}(\mathbf{r}_{ij} \cdot \mathbf{m}_j)}{r_{ij}^5} - \frac{\mathbf{m}_j}{r_{ij}^3} \right), \quad (3.3)$$

where \mathbf{r}_{ij} denotes the position vector of the i^{th} particle relative to the j^{th} particle, and \mathbf{m}_j the j^{th} particle's magnetic moment. This is the cause of dipolar interactions. Noting that the Zeeman energy of a dipole moment $E = -\mathbf{m} \cdot \mathbf{B}$, the total energy of a system of several particles is

$$E = -\sum_i \frac{KV}{|\mathbf{m}_i|^2} (\mathbf{m}_i \cdot \mathbf{n}_i)^2 + \frac{\mu_0}{4\pi} \sum_{i>j} \left(\frac{\mathbf{m}_i \cdot \mathbf{m}_j}{r_{ij}^3} - 3 \frac{(\mathbf{m}_i \cdot \mathbf{r}_{ij})(\mathbf{m}_j \cdot \mathbf{r}_{ij})}{r_{ij}^5} \right). \quad (3.4)$$

For the more specific case of a two-particle system, the total energy in the units of KV is

$$\frac{E}{KV} = -\sum_i \hat{\mathbf{e}}_i \cdot \hat{\mathbf{n}}_i + k_{\text{int}} (\hat{\mathbf{e}}_1 \cdot \hat{\mathbf{e}}_2 - 3(\hat{\mathbf{e}}_1 \cdot \hat{\mathbf{e}}_r)(\hat{\mathbf{e}}_2 \cdot \hat{\mathbf{e}}_r)), \quad (3.5)$$

where $\hat{\mathbf{e}}_i = \mathbf{m}_i / |\mathbf{m}_i|$, $\hat{\mathbf{e}}_r = \mathbf{r}_{ij} / |\mathbf{r}_{ij}|$, and for closely packed structures with $r \sim 2a$, the dipolar interaction strength takes the form that is independent of particle size, i.e., $k_{int} = \mu_0 M_s^2 / 24K$. This energy map was illustrated in Figure 3-1 (d) where $k_{int} = 0.453$ is calculated for magnetite. The value of this interaction strength plays a crucial role in determining E_b . An analytical treatment of this map provides the potential barriers required for magnetization reversals [26]. Saddle points in the energy map, which form the lowest barrier separating the two equilibria, change with critical k_{int} values and the applied field. These saddle points have been hypothesized to be the passage between the equilibria of the magnetic moments [26]. This is however plausible only when the potential barrier is large, i.e. $E_b / k_B T \gg 1$. Instead, we investigate a contrary situation where thermal fluctuations are commensurate with the energy barrier. (Note that k_{int} is defined differently in Ref. [26] and in Equation (3.5). Comparing Equation (3.5) to Equation (2) in Ref. [26], $k_{int} = 2k_{int}^{[26]}$, where $k_{int}^{[26]}$ refers to the coupling strength used in Ref. [26].)

For strong dipolar couplings with $k_{int} > 2/3$, or for weak couplings with a strong external field, the abovementioned saddle point forming the lowest energy barrier is [26],

$$E_b = 2KV \left(1 + \frac{k_{int}}{2}\right) \left(1 - \frac{h}{k_{int}/2 + 1}\right)^2, \quad (3.6)$$

where h denotes the dimensionless magnetic field. We consider a zero external field, i.e. $h = 0$. This formulation is compared with numerical calculations in Section 3.4.1.

Our second goal is to outline a strategy for the parametric design of the SA of MNPs. For this, we quantify the stabilizing influence of dipolar interactions in a linear chain of MNPs. Using the rigorous analytical framework for a two-particle system [26], we define an effective anisotropy constant K_{eff} , which can be used in the single-particle form of the Néel-Arrhenius

relation $f = f_0 \exp(-K_{\text{eff}} V / k_B T)$ in a similar manner to the concept of effective volume [70].

Comparing this expression to Equation 3.6 with $h = 0$, the effective anisotropy constant of a two-particle system

$$K_{\text{eff}} = 2K \left(1 + \frac{k_{\text{int}}}{2} \right) \quad (3.7)$$

This expression is also compared with the simulation results of Section 3.4.1.

For longer chains ($N > 2$), an analytical expression for E_b like Equation (3.6) is difficult to obtain from the saddle points in the energy hypersurface. Mean field approximations have been proposed which show qualitative agreement with experimental data [61, 71]. Such approximations are plausible only when the dynamics of the magnetic moment of any particle are faster than the collective dynamics of its neighbors. Since, dipolar coupling decays as $1/r^3$, any particle in a linear chain only experiences the strong coupling with its nearest neighbor. Hence, the dipolar coupling contribution due to the remaining particles has a significantly smaller influence. As a simple justification, we consider the energy cost required to rotate the angle θ_2 (in Figure 3-1(c)) from 0 to $\pi/2$ while holding $\theta_1 = 0$, given by $KV + (\mu_0/4\pi)(2m^2/r^3)$, and generalize this expression for chains ($N > 1$) to obtain an order of magnitude estimate for E_b , i.e.,

$$E_b = KV + \frac{\mu_0}{4\pi} \frac{2m^2}{r^3} \sum_{p=1}^{N-1} \frac{1}{p^3}. \quad (3.8)$$

The obtained values for $N = 2$ and $N = 3$ are comparable and are in agreement with the observation that the coercivity of a two-particle system is essentially the same as for longer chains when $\beta = 0$ [72].

3.3 Computational method

Due to the presence of a single domain in an MNP and the consequent coherence among the moments of the individual atoms comprising it, the magnetization of a particle can be considered as a single magnetic moment [73]. This macrospin approximation allows use of the LLG equation [62, 63] to predict the dynamics of the magnetic moment of an MNP [74-77]. Its stochastic form is a Langevin equation [77], i.e.,

$$\frac{d\mathbf{m}_i}{dt} = \gamma \mathbf{m}_i \times (\mathbf{B}_i^{eff} + \mathbf{b}_{fl}) - \frac{\gamma \lambda}{m_i} \mathbf{m}_i \times (\mathbf{m}_i \times (\mathbf{B}_i^{eff} + \mathbf{b}_{fl})) \quad (3.9)$$

where γ denotes the gyromagnetic constant of an electron spin, and λ is a phenomenological damping constant [74, 77]. $\mathbf{B}_i^{eff} = \mathbf{B}_i^{dip} + \mathbf{B}_i^a + \mathbf{B}_i^{ext}$ denotes the total effective field on the i^{th} particle where $\mathbf{B}_i^a = (2KV/m^2)(\mathbf{m} \cdot \mathbf{n})\mathbf{n}$ models the effect of magnetocrystalline anisotropy and \mathbf{B}_i^{ext} is the externally applied field, which is assumed zero for our purpose. We use a time step $\Delta t = 10^{-12}$ s [65] for which thermal agitation can be modeled as a purely random process [73, 78]. This implies that thermal fluctuations in \mathbf{m} can be investigated as the effect of a magnetic field \mathbf{b}_{fl} [64, 65, 74, 77] that satisfies the properties of a Gaussian stochastic process given by [74, 77]

$$\langle b_{fl,\alpha}(t) \rangle = 0; \langle b_{fl,\alpha}(t)b_{fl,\beta}(s) \rangle = 2 \frac{\lambda}{1+\lambda^2} \frac{k_B T}{\gamma m} \delta_{\alpha\beta} \delta(t-s). \quad (3.10)$$

A stochastic form of the Heun scheme is used to integrate Eq. (3.9), an approach that is consistent in the sense of Stratonovich stochastic calculus [77]. This assumption and the time step value are justified by a general response time for a single domain particle that is of the order of 10^{-10} s [73]. Details of the numerical scheme used can be found in Ref. [77].

3.4 Results and discussions

3.4.1 Anisotropy enhancement in a two-particle system

In light of the significance of the effective potential barrier encountered by thermally driven attempts at magnetization reversals, we first determine E_b from numerical simulations (denoted hereinafter as E_b^{num}). Since the Néel-Arrhenius relation is the simplest method to characterize such reversals, we use it to numerically calculate E_b^{num} by focusing on the change in the reversal frequency f with temperature T , as shown in Figure 3-2 (a). Fitting an exponential relation, as in Equation (3.1), allows us to determine both f_0 and E_b^{num} . In order to study the influence of dipolar interactions on magnetization stabilization, we simulate the dynamics of \mathbf{m} for a single particle and a two-particle system of magnetite with $a = 3.5$ nm such that $E_b / k_B T \sim 1$.

Figure 3-2 (a) shows that an exponential rule is followed for the decay in reversal frequency f , as suggested by Equation (1) so that the slopes of the fitted curves provide the effective E_b^{num} . The data are presented in Table 2 and compared with theoretical predictions, i.e., $E_b = KV$ for isolated particles ($N = 1$) and $E_b = 2KV(1 + k_{int}/2)$ for two-particle systems ($N = 2$) as determined from Equation (3.6) with $h = 0$. For $N = 1$, E_b is expected to be underestimated since \mathbf{m} seldom relaxes to its equilibrium state that is aligned with the easy axis \mathbf{n} . The energy expense for a reversal is therefore rarely equal to the theoretical barrier of KV in this noisy regime. However, when particle size increases, the potential barrier is closer to the theoretical prediction, which will be seen when we use a similar analysis with Figure 3-5 to determine K .

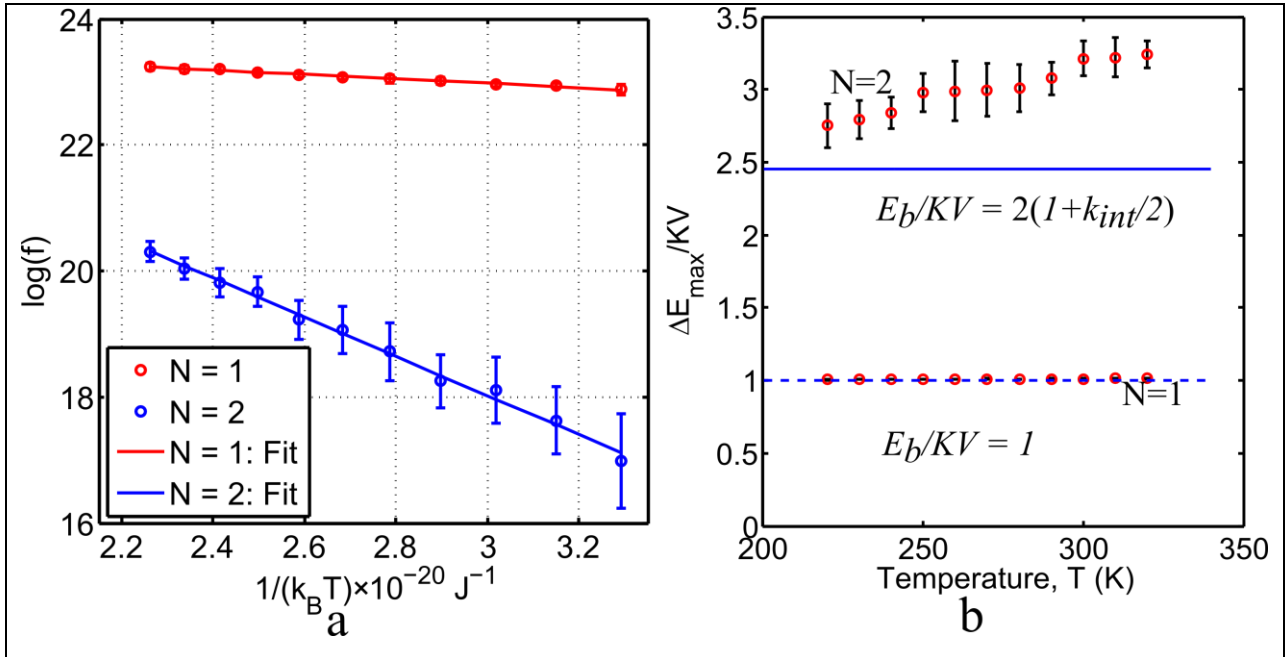


Figure 3-2 Determination of the potential barrier E_b from numerical simulations. (a) Variation of reversal frequency f with temperature for magnetite particles with $a = 3.5$ nm. The logarithmic nature of the plot indicates that the Néel-Arrhenius relation is followed. The effective potential barrier E_b is obtained from the slope and compared with theory in Table 3.3. (b) The maximum change in energy ΔE_{\max} for an interval of $1 \mu\text{s}$ is seen to remain same for $N = 1$, but increases with $N = 2$. Also, while ΔE_{\max} matches E_b for $N = 1$, the saddle point hypothesis in Equation (3.6) underestimates actual energy expense in reversals. The heights of the error bars equal 2σ (determined from ten simulations) but these are absent where occluded by the plot markers.

Table 3-2 Comparison of the numerically determined E_b^{num} for magnetite particles with $a = 3.5$ nm with theoretical models.

	$N = 1$	$N = 2$
E_b^{num} / KV determined from Figure 3-2(a) using Equation (3.1)	0.839	7.524
E_b/KV determined from theoretical model*	1.000	2.453

*Assuming no external field is present, for $N = 1$, $E_b = KV$ and for $N = 2$, $E_b = 2KV(1 + k_{\text{int}}/2)$ is determined from equation (6) with $h = 0$.

For $N = 2$, however, the disparity is much larger. This can be explained by considering that the value of E_b predicted by Equation (3.6) only determines saddle points in an anisotropic energy map. In the very noisy simulated systems, thermal fluctuations can cause the system of magnetic moments to reverse along many paths, which are not necessarily energetically the most economical.

To more accurately calculate the energy barriers traversed during reversals, the potential energy change during a reversal must be examined. However, in a very noisy system, it is impossible to demarcate the beginning and end of a reversal event. Instead, we look at the maximum potential energy difference over a simulation time of 1 μs as a measure of the maximum potential barrier crossed by the system, denoted by ΔE_{max} . This is a measure of the highest expenditure afforded by thermal reversals during that period of magnetization dynamics. Figure 3-2 (b) demonstrates that for the cases simulated for Figure 3-2 (a), for $N = 1$, $\Delta E_{max} = KV$. However, as predicted, for $N = 2$, $\Delta E_{max} > 2KV(1 + k_{int}/2)$. This qualitatively validates our hypothesis.

Quantitatively, the potential barrier E_b^{num} is much larger than the maximum energy ΔE_{max} expended during a reversal. This implies that the maximum potential barrier preventing a thermal reversal is actually never overcome. This can be expected in a stochastic system in which the potential barrier separating the equilibria is path-dependent. The two values will match only when thermal fluctuations are very large or when the simulation time is very long. For the 110 simulations performed to obtain the plot for $N = 2$, such a situation was never encountered. Consequently, an effective potential barrier must be determined, which should be temperature dependent and account for the distribution of reversal paths for a system with an anisotropic energy map.

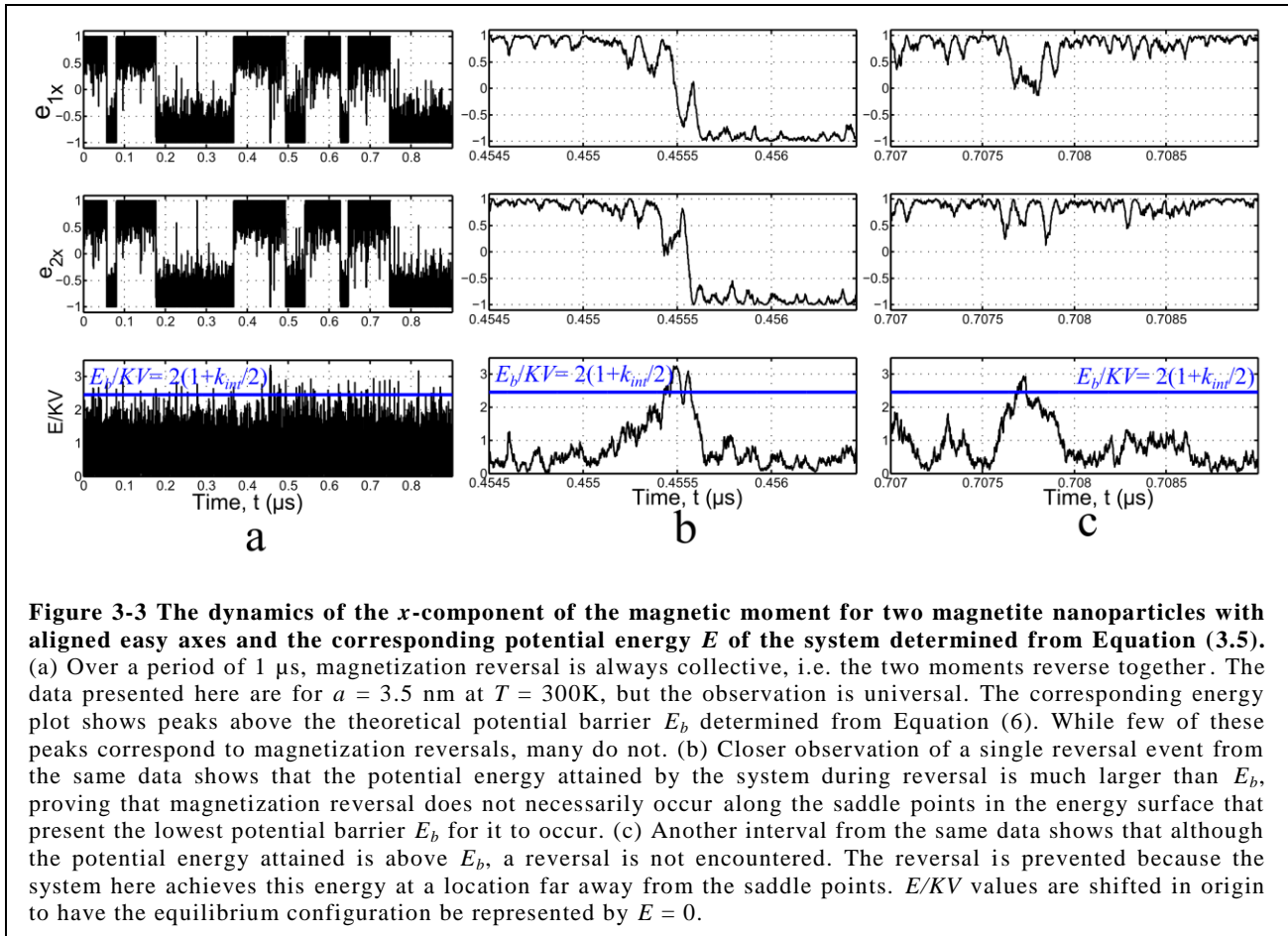


Figure 3-3 The dynamics of the x -component of the magnetic moment for two magnetite nanoparticles with aligned easy axes and the corresponding potential energy E of the system determined from Equation (3.5). (a) Over a period of 1 μ s, magnetization reversal is always collective, i.e. the two moments reverse together. The data presented here are for $a = 3.5$ nm at $T = 300$ K, but the observation is universal. The corresponding energy plot shows peaks above the theoretical potential barrier E_b determined from Equation (6). While few of these peaks correspond to magnetization reversals, many do not. (b) Closer observation of a single reversal event from the same data shows that the potential energy attained by the system during reversal is much larger than E_b , proving that magnetization reversal does not necessarily occur along the saddle points in the energy surface that present the lowest potential barrier E_b for it to occur. (c) Another interval from the same data shows that although the potential energy attained is above E_b , a reversal is not encountered. The reversal is prevented because the system here achieves this energy at a location far away from the saddle points. E/KV values are shifted in origin to have the equilibrium configuration be represented by $E = 0$.

To substantiate these arguments, we examine the dynamics of \mathbf{m} . Figure 3-3 (a) presents the dynamics of the moments of two magnetite nanoparticles where, despite the heavy noise, reversals in \mathbf{m} are invariably collective, i.e., the moments always flip together. The potential energy of the system is calculated from Equation (3.5) for each step and shows peaks that exceed E_b during each reversal event. However, several peaks exist where $E > E_b$ although a reversal is not observed. Figure 3-3 (b) offers a closer look at one such reversal event. The potential energy clearly exceeds that at the saddle point E_b during the reversal, indicating that reversal does not occur over the saddle point but along a path that is energetically more expensive. This is true for most reversals as seen from the energy plot in Figure 3-3 (a). Figure 3-3 (c) demonstrates how during an interval, whereas E exceeds E_b , a reversal is not observed. This is because the system

attains such a potential at a state far away from the saddle points. The barrier near these positions in the state space is much higher than the thermal fluctuations can afford and consequently a reversal is prevented.

All three components of the magnetic moment are plotted over time in Figure 3-4. Ref. [26] predicted that when $k_{int} < 2/3$ and an external magnetic field is absent, a thermal reversal can occur by coherent rotation for which the formulation for E_b is different from that in Equation (3.6). Despite the strong noise, the switching mode we observe is symmetric fanning, characterized by $e_{1y}e_{2y} < 0, e_{1z}e_{2z} < 0$. This justifies our choice of the relation of Equation (6) to characterize the energy barrier. The analysis in Ref. [26] is valid for relatively low thermal noise. When the latter is significant, it plays the role of an external field requiring the use of Equation (3.6) instead.

The effective anisotropy predicted in Equation (3-7) is next put to test. By observing the variation in f with particle volume V , we can numerically calculate the effective anisotropy constant K_{eff}^{num} in a similar manner to the process adopted to determine E_b^{num} . We observe an exponential decay of f with V , as seen in Figure 3-5. K_{eff}^{num} is compared to K_{eff} in Table 3.3, showing a huge disparity between the two values for $N = 2$, the reasons for which are similar to those for the differences between E_b and E_b^{num} . However, there is a saturation in the anisotropy enhancement by dipolar interactions as N increases beyond three particles, which supports our arguments to this effect in Section 3.2.

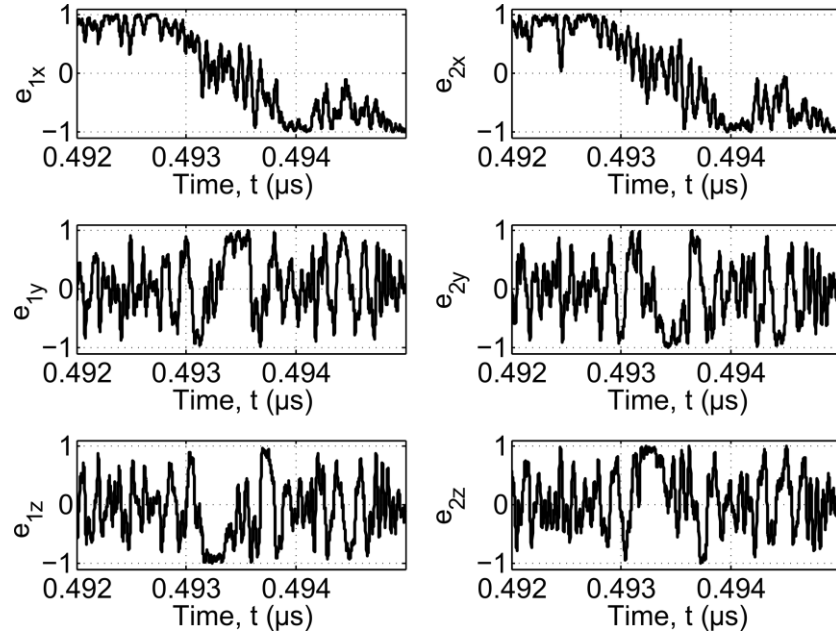


Figure 3-4 The magnetization dynamics of two neighboring magnetite particles with $a = 3.5$ nm at $T = 300$ K show that the mode of switching is close to symmetric fanning, i.e., $e_{1y}e_{2y} < 0, e_{1z}e_{2z} < 0$. High thermal noise is visible.

The y -intercept in Figure 3-5 provides the value of f_0 , which is also presented in Table 3.3. These numerical values are in agreement with earlier observations made from similar simulations [65]. However, since f_0 depends on the choice of λ [65] that is yet unknown for most materials, the numerical values discussed for the prefactor should be simply construed as trends.

The nature of the curves indicates that an exponential relation of the form

$$f = f_0 \exp\left(-\frac{K_{eff}(V - V_0)}{k_B T}\right) \quad (3.11)$$

is an effective replacement for Equation (3.1) for a system of interacting MNPs in a linear chain. This empirically motivated expression allows us to use a simplified universal value of f_0 for interacting MNPs. The theoretical basis for this expression is outside the scope of this work.

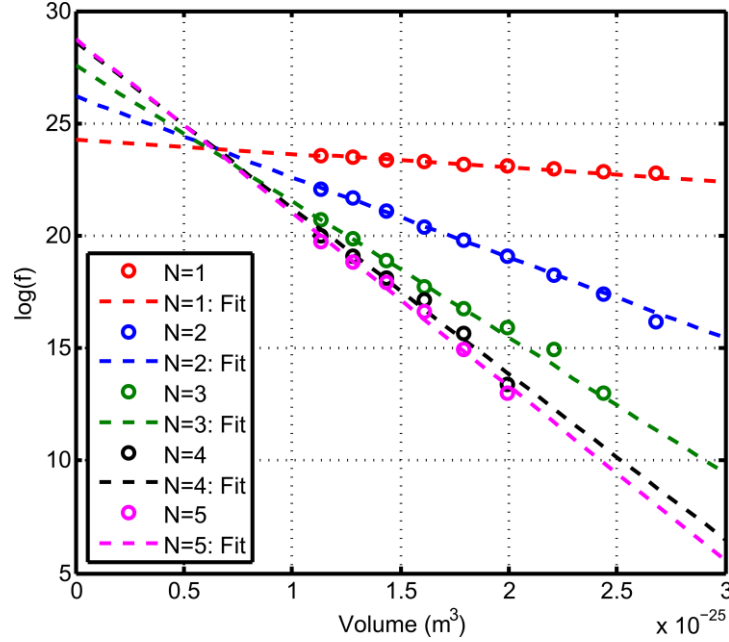


Figure 3-5 The magnetization reversal frequency diminishes exponentially with volume in an isolated MNP as well as the terminal particle in a linear chain. The slope of the curve allows K_{eff}^{num} to be determined, while the y-intercept provides the value of the attempt frequency f_0 (Table 3.3). The simulations represent magnetite nanoparticles with a damping coefficient $|\lambda|=0.1$. Each data point is the mean value realized from 10 simulations of 1 μ s duration.

Table 3-3 K_{eff} calculated from Equation (7) for $N = 2$, the numerically determined effective anisotropy K_{eff}^{num} from Figure (3-5), and the attempt frequency f_0 determined from Figure (5) for magnetite nanoparticles

Chain Length (N)	K_{eff} from Eq. (7) (kJ m ⁻³)	K_{eff}^{num} from Fig. 5 (kJ m ⁻³)	f_0 (GHz)
1	23.0*	23.0	31.8
2	56.4	146.3	223.4
3	-	236.5	601.2
4	-	306.1	2742.2
5	-	324.0	3106.4

*The effective anisotropy constant of a single particle is simply magnetocrystalline anisotropy constant of the material K . The corresponding numerical value shows good agreement.

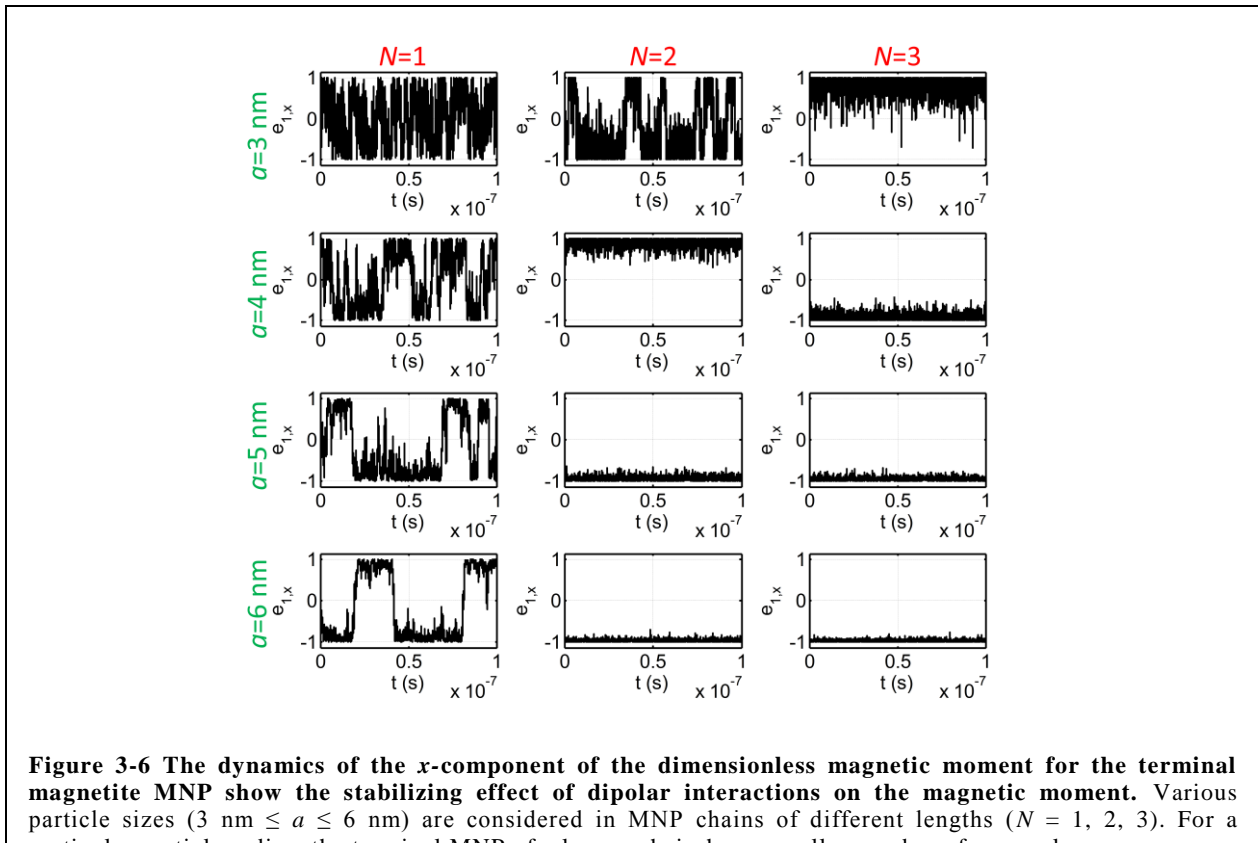
3.4.2 Parametric design for dipolar stabilization of magnetization reversal

Equation (3.9), which governs the dynamics of a system of interacting magnetic moments, is rather involved. Its stochastic nature, brought about by thermal noise, adds to the complexity. However, an accessible design strategy for an SA process aimed at dipolar stabilization can still be construed from the more simple approach of comparing the energy barriers for an isolated particle and a two-particle system by using a universal value of f_0 as suggested in Equation (3.11). This strategy aids the choice of materials and particle sizes to enhance anisotropy in linear chains of MNPs that have their easy axes aligned along the chain direction. We determine the bounds on particle size within which, over a duration τ_m (often called the measurement time), (1) an isolated particle has a fluctuating magnetic moment due to its low anisotropy so that it has no net magnetization, and (2) dipolar interactions in a two-particle system or a longer linear chain enhance the effective anisotropy and stabilize the magnetic moments so that reversals are minimal, i.e., some remanence is observed. The discussion in Section 3.2 on the influence of dipolar coupling on E_b leads to parametric equations for this purpose.

Since magnetite forms the core of most commercially available MNPs, we use it as an example material to determine approximate lower bounds on the radii that ensure a stable dipole moment over $\tau_m = 100$ ns at room temperature ($T = 300$ K) for an isolated MNP and a two-particle system. Magnetite has a saturation magnetization $M_s = 446 \times 10^3$ A/m and an anisotropy constant $K = 23 \times 10^3$ J/m³ [79]. The potential barrier between the stable equilibria of the magnetic moment of an isolated magnetite nanoparticle arises solely due to the magnetocrystalline anisotropy, i.e. $E_b = KV = 9.63a^3 \times 10^4$ J. For an isolated MNP to have a stable magnetic moment for 100 ns requires that $f \leq 10^7$ Hz. Assuming $f_0 \sim 30$ GHz (a value that is determined from our simulations and also reported in previous studies [65]), this requires

$E_b \geq 8k_B T$, i.e. $a \geq 7$ nm. Thus, for any $a \leq a_1$ the particle undergoes magnetization reversals over 100 ns. As seen in Figure 3-6, for $a = 6$ nm and $N = 1$, a few magnetization reversals are indeed observed over this time, implying that the net magnetization during this period is very small.

For a two-particle system when the easy axis of each particle is parallel to the chain direction and no external magnetic field is present, the potential barrier obtained from Equation (3.6) is enhanced to $E_b = 2KV(1+k_{int}/2) = K_{eff}V$. We assume the relation $E_b \geq 8k_B T$ holds for estimating the limiting radius for a stable magnetization over $\tau_m = 100$ ns. This is true only if f_0 is the same for both $N = 1$ and 2, which is not the case. However, considering that $a_2 = (\ln(f_0\tau_m) \times 3/4\pi \times 8k_B T / K_{eff})^{1/3}$, i.e. $a_2 \sim (\ln(f_0))^{1/3}$ and the attempt frequencies differ by



less than an order of magnitude as listed in Table 3.2, such an assumption is plausible. The lower bound for the particle radius for a stable magnetization over $\tau_m = 100$ ns is therefore $a_2 = 5.20$ nm. This means that a particle with $a \geq a_2$ should have a stable magnetic moment in such a two-particle system over 100 ns. We observe from Figure 3-6 that when $N = 2$ particles and $a \geq 4$ nm, the system has a fairly stable magnetization. The mismatch is due to the higher effective anisotropy encountered in a two-particle system than the saddle point analysis used to derive Equations (3.6, 7) [26], as discussed in Section 3.4.1.

From these two considerations, for a duration of $\tau_m = 100$ ns, all particle sizes within $a_1 < a < a_2$ have no net magnetization in isolated conditions in a dilute dispersion. However, when they are self-assembled to form a linear chain having aligned easy axes, a remanence is observed over the same time period τ_m . Table 3-4 lists the two critical radii determined from similar considerations for a wide range of MNP materials in use.

It should be noted that Equation (3.7) underestimates the values of K_{eff} obtained from the simulations, as shown in Table 3-3. Thus, although f decays exponentially with V , better theoretical models must be developed to replace Equation (3.7) to determine the effective anisotropy for situations when thermal fluctuations are commensurate with the potential barrier for interacting MNPs. In their absence, our analysis overestimates the lower bound of particle radius for which a linear chain acquires remanence over a specified duration, i.e., the predicted range of particle sizes might be narrower than the actual window.

Table 3-4 Material properties of common MNP core materials [80] and the calculated critical radii for stable magnetization of isolated MNPs (a_1) and two-particle systems (a_2) over measurement time $\tau_m = 100$ ns.

Material	Saturation Magnetization (M_s) (kA/m)	Anisotropy Constant (K) (kJ/m ³)	a_1 $E_b = KV \sim 8k_B T$ (nm)	a_2 $E_b = K_{eff}V \sim 8k_B T$ (nm)
Magnetite	446	23	7	5.2
fcc FePt	1140	206	3.4	2.5
Maghemite	414	4.7	11.9	7.5
FeCo	1790	1.5	17.4	3.6
CoFe ₂ O ₄	425	180	3.5	2.8
BaFe ₂ O ₄	380	300	3.0	2.3

To test this, we introduce the time average of the x -component of the dimensionless magnetization vector $\langle e_x \rangle$ over 100 ns of simulated data as a metric for the net magnetization over $\tau_m = 100$ ns. Frequent magnetization reversals provide small values of $\langle e_x \rangle$ close to zero whereas for a stable magnetization $\langle e_x \rangle \sim 1$. The results in Figure 3-7 (a) validate the above estimate, i.e., for the stable magnetization of isolated MNPs, $a \geq 7$ nm. For $N = 2$, however, the critical radius a_2 that leads to a stable magnetic moment is ~ 4 nm, which is lower than the estimated $a_2 = 5.20$ nm. The actual window of particle sizes is thus indeed wider than one which was estimated above.

It is desirable to have a metric that relates this particle size window to material properties. While the actual particle size is dependent on the choice of τ_m , the ratio a_1 / a_2 depends on the material properties alone, i.e. on M_s and K . Specifically, it is related to the dipolar interaction strength $k_{int} = \mu_0 M_s^2 / 24K$ because $a_1 / a_2 = K_{eff} / K$, or,

$$\frac{a_1}{a_2} = (2 + k_{int})^{1/3}. \quad (3.12)$$

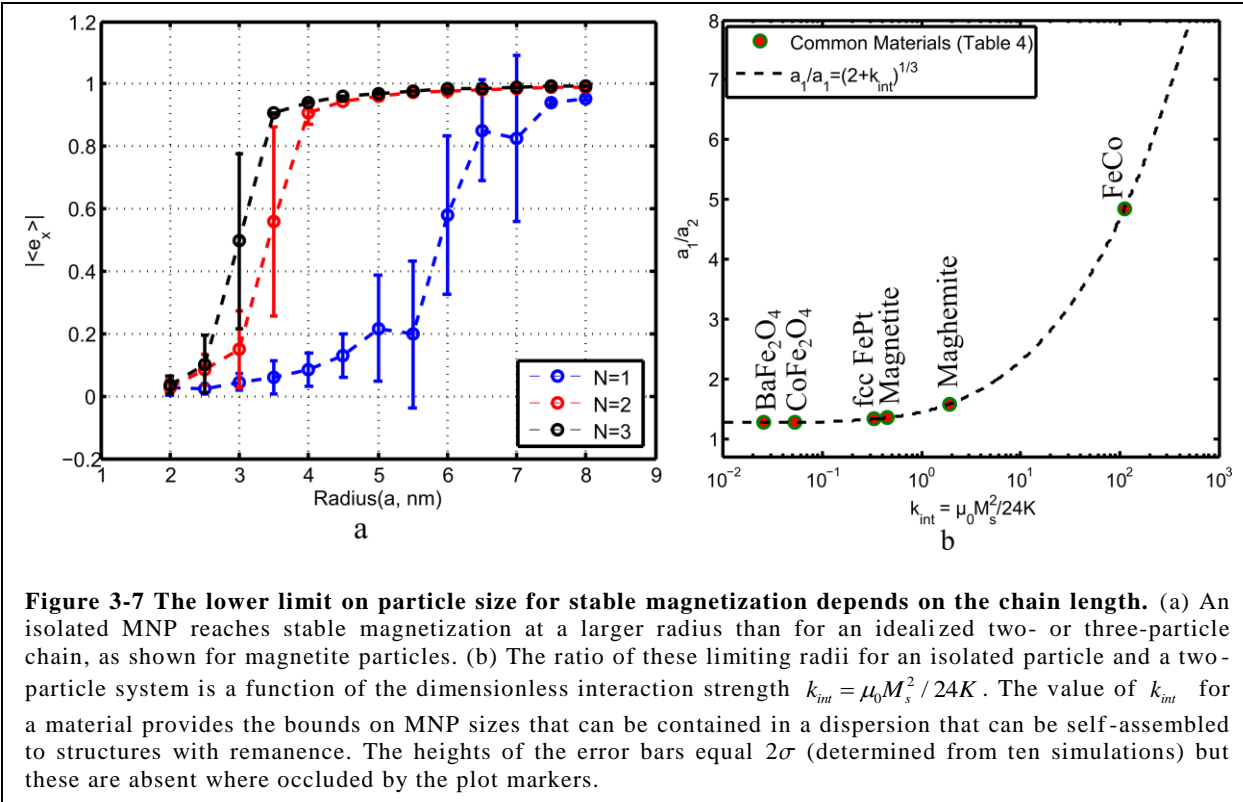


Figure 3-7 The lower limit on particle size for stable magnetization depends on the chain length. (a) An isolated MNP reaches stable magnetization at a larger radius than for an idealized two- or three-particle chain, as shown for magnetite particles. (b) The ratio of these limiting radii for an isolated particle and a two-particle system is a function of the dimensionless interaction strength $k_{int} = \mu_0 M_s^2 / 24K$. The value of k_{int} for a material provides the bounds on MNP sizes that can be contained in a dispersion that can be self-assembled to structures with remanence. The heights of the error bars equal 2σ (determined from ten simulations) but these are absent where occluded by the plot markers.

For a specific material, k_{int} provides a global measure of the width of the range of radii within which isolated MNPs behave as superparamagnetic nanoparticles but develop remanence upon SA into a linear chain. Figure 3-7 (b) plots Equation (3.12) and also identifies where the materials listed in Table 3-4 lie on it. Since the expression is independent of time, k_{int} serves as a material choice guide for designing an SA process where superparamagnetic nanoparticles self assemble to form structures with residual magnetization. Larger values of k_{int} allow a wider particle radii window for such an SA process, i.e., a material with large M_s and low K is ideal, e.g. FeCo.

3.4.3 Magnetization reversal in longer chains ($N > 2$)

Since linear chains formed by self-assembled MNPs are seldom two particles long, we now consider longer chains. In the absence of a rigorous estimate for E_b , we use Equation (3.8) for an

approximation. The relation shows that the potential barrier due to dipolar interactions approaches a finite value as N increases so that higher order terms beyond $p = 2$ can be neglected for long chains. This is also clear from the K_{eff} values determined from simulations that are listed in Table 3-3. To visualize the effect of this potential on the stability of a terminal dipole, we simulate the magnetization dynamics of MNP chains of various lengths for four particle sizes. The results presented in Figure 3-8 (a) show that systems with longer magnetite MNP chains have a more stable terminal dipole. This effect is more pronounced for systems in which individual MNPs have a significantly low anisotropy, such as magnetite MNP with $a = 2.5$ nm. Once a particular potential barrier that can no longer be overcome by thermal fluctuations is reached, magnetization stabilizes. Thus, for systems with particle sizes $a \geq 3.5$ nm, chains with $N = 2$ or 3 particles show no significant differences in net magnetization over the $\tau_m = 100$ ns chosen, whereas a similar comparison with $a = 2.5$ nm is appreciably different.

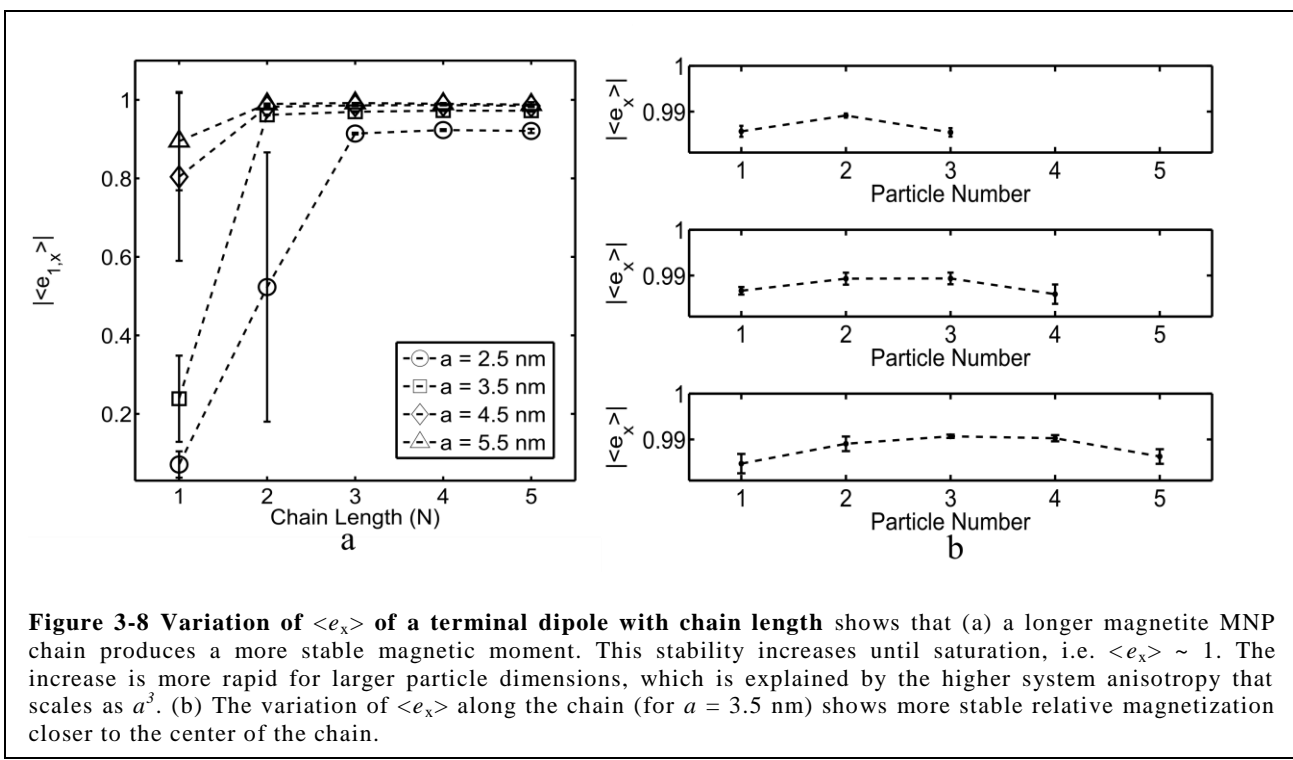


Figure 3-8 Variation of $\langle e_x \rangle$ of a terminal dipole with chain length shows that (a) a longer magnetite MNP chain produces a more stable magnetic moment. This stability increases until saturation, i.e. $\langle e_x \rangle \sim 1$. The increase is more rapid for larger particle dimensions, which is explained by the higher system anisotropy that scales as a^3 . (b) The variation of $\langle e_x \rangle$ along the chain (for $a = 3.5$ nm) shows more stable relative magnetization closer to the center of the chain.

The stability of spins varies along the length of a chain. Intuitively, terminal dipoles should have lower stability as they are coupled with only one neighboring dipole. Other MNPs in a chain have two nearest neighbor so the effects of dipolar coupling are higher. The MNP at the center of a chain should have the maximum stability. This is confirmed through the results shown in Figure 3-8 (b). However, the differences in $|<e_x>|$ between the terminal and other MNPs are not significant. This is an important consideration, since the terminal dipoles form the pole-faces of hypothetical self-assembled structures that develop a residual magnetization.

3.5 Conclusions

We investigate the influence of dipolar interactions on the stabilization of the magnetic moment at relatively high temperatures. Theoretical estimates for the potential barrier in the magnetization reversal of a two-particle chain [26] assume that magnetization reversal occurs along the energetically most inexpensive pathway, i.e., the saddle points in the energy surface. Our numerical simulations indicate that this is not necessarily true when thermal fluctuations are significant. Improved models must be developed to ascertain the effective potential barrier encountered by thermal fluctuations to force magnetization reversal in systems where the energy map is anisotropic and the encountered barrier becomes path-dependent. We empirically observe that a modified Néel-Arrhenius relation can be construed enabling the use of a universal value of the attempt frequency, the theoretical basis for which is left as a future exercise. Subsequently, we provide a conservative design strategy for the stabilization of magnetic moments using existing theoretical models. This will aid in the choice of materials and other process variables for the design of an SA process where the dipolar stabilization of the magnetic moments is maximized. In such a process, individual particles in a dilute dispersion will have frequent

magnetization reversals and thus a net zero magnetization corresponding to a measurement time. However, once self-assembled into linear chains with the easy axes aligned with the chain direction, dipolar interactions augment the potential barrier for magnetization reversal. This reduces the chance and, in effect, the frequency of magnetization reversal, leading to a microstructure that demonstrates remanence over the same measurement time.

3.6 Acknowledgements

The Virginia Tech Advanced Research Computing cluster ATHENA and the Department of Engineering Science and Mechanics Linux Compute Cluster were used for the simulations. We thank Mr. Sourav Mishra and Prof. Ge Wang of the Virginia Tech-Wake Forest University School of Biomedical Engineering and Sciences for providing access to X-Ray computed tomography that is supported by the NSF grant CMMI 0923297.

4. Magnetic assembly of 3D cell culture³

An externally applied magnetic field is used to assemble magnetized human cells into three-dimensional (3D) clusters. This forms the means for 3D cell culture without using artificial scaffolds. When the cells are held in close proximity with the magnetic field for a day, they form intercellular contacts aided by extra-cellular fibers. Subsequently, the cells organize themselves into tight clusters. For epithelial cells, the cluster takes the form of a multi-layer sheet. For fibroblasts, it is a tightly packed spheroid. The connecting fibers are observed to exercise tension on the cells. This suggests that the fibers are responsible for organizing the cells. For the HFL-1 cell line, cells on the periphery of the 3D clusters are seen to assume a different morphology than the cells that lie within them. This shows that cells assume different physical forms based on their functional role, as determined by sensing their microenvironment.

4.1 Motivation and background

Three-dimensional (3D) cell cultures better mimic *in vivo* conditions than monolayers [81] since activities of a cell, e.g., protein expression and morphology, are strongly influenced by its interactions with the microenvironment, i.e., neighboring cells [82] and the extra-cellular matrix (ECM) [83]. Popular 3D culture methods employ artificial scaffolding materials [84], e.g., polymer nano-fibers or extracellular proteins of animal [85] or microbial [86] origin, in order to

³Adapted from S. Ghosh *et al.*, “Magnetic assembly of 3D cell cultures eliminates the need for artificial scaffolds”. *In preparation*, 2013.

simulate the ECM. Thus the microenvironment differs from *in vivo* conditions, causing differences in cell behavior [87]. We present a 3D culture method that eliminates the need for artificial scaffolds. Cells are magnetized by internalizing magnetic nanoparticles (MNPs), which are then assembled into 3D structures by magnetic forces. We show here that when cells are held in place with magnetic force for a day, they form intercellular contacts facilitated by extracellular fibers. Through these contacts, the cells organize themselves into tight clusters: epithelial cells form multi-layer sheets while fibroblasts form spheroids. Further, cells tend to acquire different morphologies based on their position in the cluster.

Most 3D cell cultures in use employ artificial scaffolding materials to provide mechanical support to cells [88]. The most popular methods use gelatinous networks of extracellular proteins, e.g., Matrigel [85, 89]. However, these materials are never native to the cells involved, making the microenvironment different from *in vivo* conditions. Thus, a tissue cultured in this manner is not a faithful mimicry of *in vivo* state [85, 87]. One solution is to assemble cells into a structure using an external impetus that has no physical contact with the cells, e.g., magnetic forces. However, a strategy to ‘assemble’ an artificial tissue is feasible only if, after the assembly, cells form contacts with their neighbors and organize into a physical and functional form. We show the first evidence towards this in cells assembled by magnetic forces. Both epithelial and fibroblast cells form intercellular contacts and organize themselves into tighter clusters. Shape of such clusters is consistent with the physical form of the corresponding tissues in a natural environment.

Gelatinous scaffolds do not provide control over the shape and size of a culture, nor the ability to pattern heterogeneities in the population constitution. However, inter-cellular communications are often dependent on shape, size and population makeup of a tissue. For

instance, tumor growth is regulated by communications via interleukins [90]. Spatiotemporal variations in interleukin concentration are hypothesized to be responsible for the characteristics of tumorigenesis, e.g., ‘seed-to-soil’ organ-specific metastasis and long dormancy periods [91]. The shape, size and population makeup of a tumor dictates interleukin concentration, thus they have a significant bearing on tumor growth. Testing such a transformational hypothesis requires an experimental model in which (1) the cellular microenvironment replicates a live tissue, and (2) the shape, size and population heterogeneities of a 3D cluster of cells can be controlled as desired [92]. We present an economic method that can accomplish both. The method is easily implemented in any laboratory practicing cell culture.

‘Action-at-a-distance’ manipulation of magnetized cells has been explored for decades [93-95]. Potential uses span targeted drug delivery [36], cell-sorting [33] and tissue engineering [96, 97] besides novel tools enabling fundamental discoveries in biology [98]. These are achieved by coating MNPs with cytocompatible materials. Thus ‘camouflaged’, the MNPs are readily internalized by cells [99], and can be targeted to specific cell types [100]. Once the MNPs are internalized, the cells are magnetized and can be manipulated using an externally applied magnetic field [96, 101-104]. Recently, a method for magnetic assembly of cells into a tissue of desired shape was reported. It uses scaffolding materials of microbial origin conjugated with MNPs [86]. Cells first adhere to the scaffolds, and then the scaffolds are assembled into desired shapes using magnetic forces. However, the method must still incorporate foreign scaffolding materials. We show here that if magnetic forces are used to hold a group of cells in close proximity for a day, they form inter-cellular contacts and organize themselves into tighter clusters alleviating the need for artificial scaffolding materials.

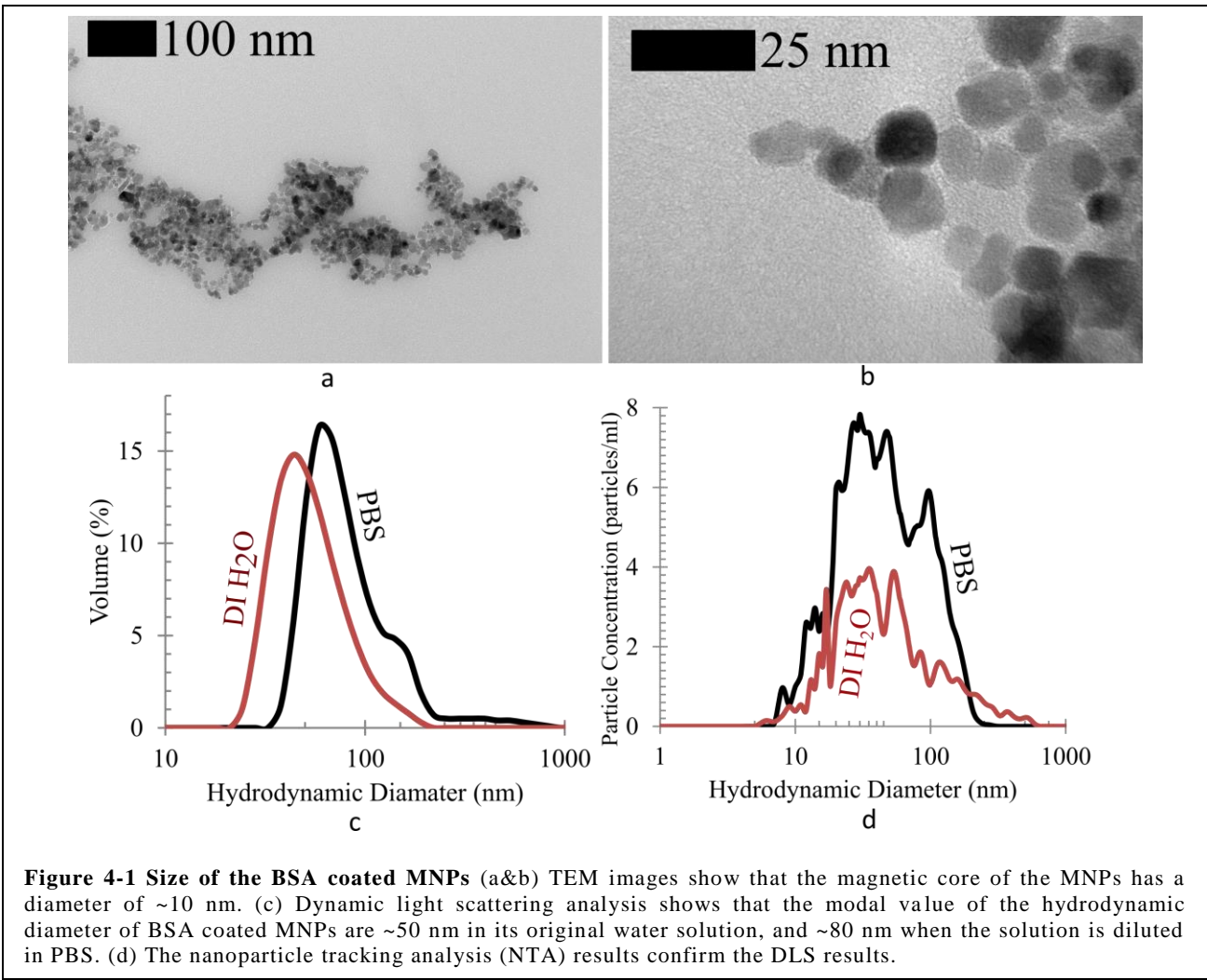
4.2 Materials and Methods

4.2.1 *Synthesis of magnetic nanoparticles*

Magnetite nanoparticles were synthesized by a modified Massart coprecipitation method [105] and coated with BSA essentially as described in Ref. [99]. 1.72 g FeCl₂·4H₂O and 4.67 g FeCl₃·6H₂O were dissolved in 60 ml degassed and deionized (DI) water (ASTM Type II, LabChem Inc.). The solution was then added to 20 ml ammonium hydroxide with vigorous stirring. A black-brown precipitate of magnetite nanoparticles was formed. The mixture was then centrifuged (5000×g, 15 minutes) and the pellet redispersed in deionized water to remove unreacted reagents and to decrease the pH. The process was repeated 5 times. The MNPs were then pelleted again and redispersed in 20 ml of 5% (w/v) aqueous solution of BSA (Fisher BioReagents, Fraction V, heat shock treated). The dispersion was then sonicated for 1 hour using a probe sonicator (Fisher Sonic Dismembrator, Model 300). The resulting dispersion was a homogeneous reddish brown liquid when inspected at 400× magnification through an inverted microscope. The solution was made to stand overnight, and then ultracentrifuged (OptimaTM L-90K, Beckman-Coulter) at 100,000×g for 1 hour. The pellet was redispersed in 40 ml deionized water by sonication. This process removed the excess BSA. The dispersion remained stable for several months when stored at 4°C.

4.2.2 *Characterization of magnetic nanoparticles*

The size of the MNPs was measured using dynamic light scattering (Malvern Zetasizer Nano ZS90), nanoparticle tracking analysis (NanoSight) and transmission electron microscopy (Philips EM420). The magnetic core of the MNPs was ~10 nm, while the modal value of the hydrodynamic diameter of particles were ~50 nm in DI water and ~80 nm when the stock



solution was diluted in PBS. This was possibly because of some agglomeration, as well as the BSA coating on the MNPs. Results are presented in Figure 4-1.

4.2.3 Cell culture

Vero cells were obtained from American Type Culture Collection (ATCC) and cultured in Dulbecco's Modified Eagle Medium (DMEM, Life technologies). Prostate cancer epithelial (PC-3) cells (ATCC) were cultured in Roswell Park Memorial Institute (RPMI) medium (Life technologies). Human lung fibroblast (HFL-1) cells (ATCC) were cultured in Ham's F-12K (Kaighn's) medium (Life technologies). All media were supplemented with heat inactivated 10% (v/v) fetal bovine serum (FBS, Atlanta Biologicals) and 1% (v/v) penicillin/streptomycin

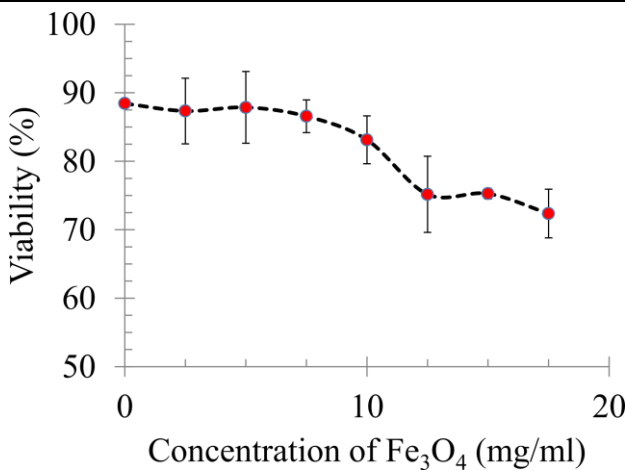


Figure 4-2 Cytotoxicity of the BSA coated MNPs are evaluated by measuring the % viability of PC-3 cells at various concentrations of MNPs in PBS. Measurements are done by typan blue staining of dead cells, followed by counting using the Nexcelom Cellometer®. Height of error bars = 2σ , $N = 4$.

(Sigma). Additionally, the RPMI media was supplemented with 1% (v/v) Geneticin (G418, Life technologies) to select stably transfected PC3-mOrange cells. The PC3-mOrange cells were originally developed in Dr. Elankumaran's laboratory (unpublished) and used in this work with no further modifications. The cells were trypsinized and reseeded every 3-4 days. They were cultured at 37 °C in a humidified environment with 5% CO₂. Vero and PC-3 cells were within their 20th and 40th passages, and HFL-1 cells were within their 5th and 10th passages.

4.2.4 Magnetization of cells

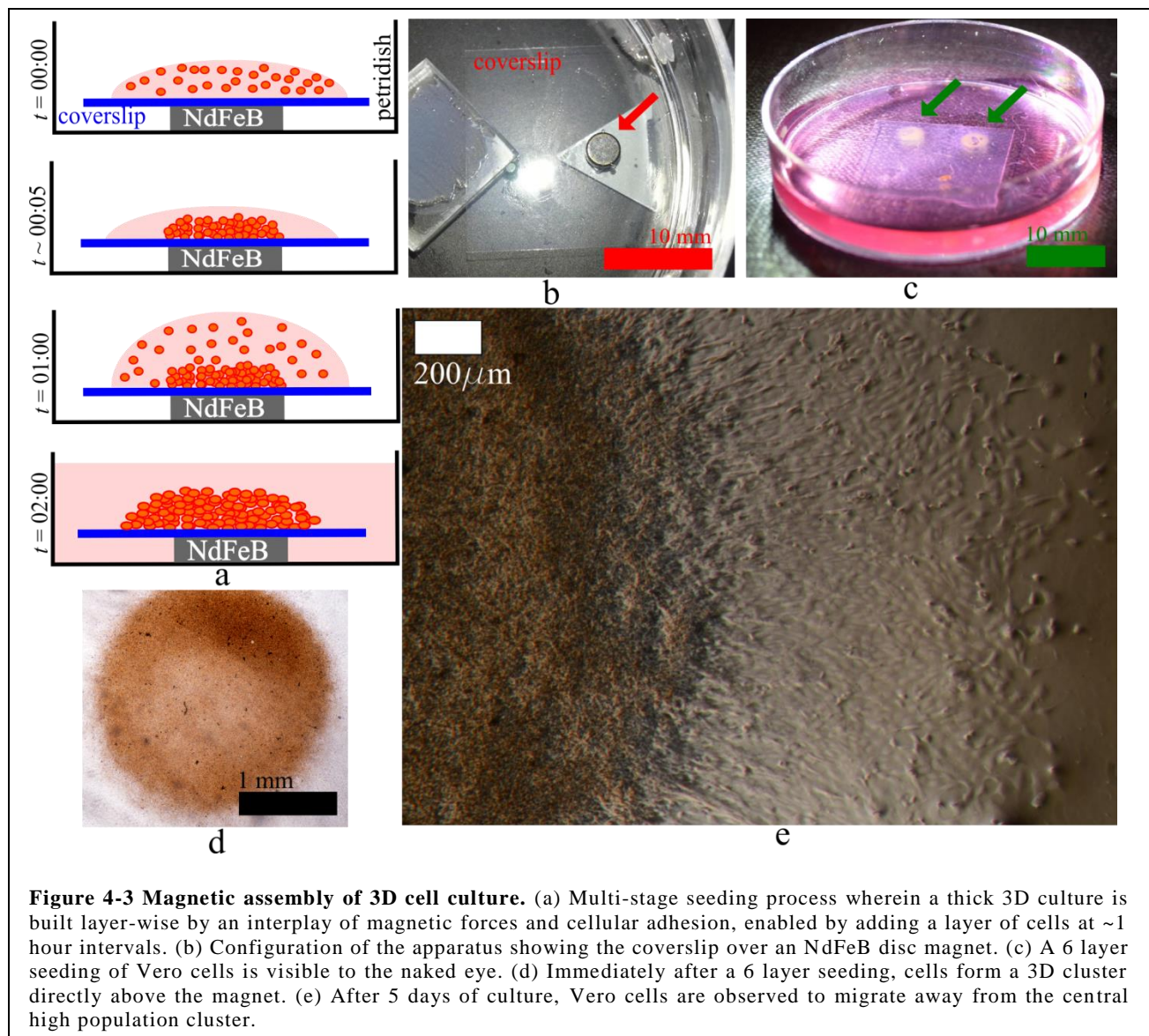
The solution of BSA coated MNPs in deionized water was diluted in Dulbecco's phosphate buffered saline (DPBS) at a ratio of 1:3 (v/v). This dilution had an MNP concentration of 12.5 mg ml⁻¹ and did not result in significant cytotoxicity, as seen in Figure 4-2. Cells were seeded in a 12 well tissue culture plate (Nunc) at 70-80% confluence and allowed to attach overnight. Each well was then washed and treated with the diluted MNP dispersion in PBS and incubated at 37 °C in a humidified environment with 5% CO₂ for 1 hour. The cells were subsequently washed 5 times, trypsinized using standard technique and used for experiments.

4.2.5 Sample preparation and imaging with Scanning Electron Microscopy (SEM)

The SEM images of the cells at various time points after seeding were obtained from samples fixed at the corresponding time points. Karnovsky's fixative was prepared by dissolving 4 g paraformaldehyde powder in 50 ml distilled water at 70°C. The solution cleared when a drop of potassium hydroxide was added. The solution was then cooled, 10 ml of 50% glutaraldehyde was added, and the volume was brought up to 100 ml using 0.2 M sodium cacodylate. Finally, 50 mg calcium chloride was added slowly. The 3D cell clusters, seeded on glass coverslips, were first washed three times with PBS, then treated with Karnovsky's fixative and left at 4°C overnight. The samples were subsequently washed with 0.1 M sodium cacodylate buffer for 15 minutes, post-fixed with 1% OsO₄ in 0.1 M sodium cacodylate for 1 hr, washed twice with sodium cacodylate buffer and dehydrated in graded ethanol series. Then, the samples were dried (Ladd critical point dryer), coated with gold (SPI Module™ sputter coater) and imaged using the Carl Zeiss EVO® 40 series scanning electron microscope.

4.2.6 Confocal microscopy

The PC-3 cells were stably transfected to express mOrange (unpublished) and cultured in media supplemented with Geneticin as described above in Section 4.2.3. Z-stack images of live 3D cell clusters were obtained 1 day after seeding using a Zeiss-LSM510 META laser scanning microscope on an inverted Axio Observer Z1 base.



4.3 Results and Discussions

We introduce bovine serum albumin (BSA) coated magnetite nanoparticles into adherent mammalian cells [99]. The magnetized cells were then assembled into a 3D cluster on a substrate using permanent magnets. The process is illustrated in Figure 4-3. (Similar 3D culture was also performed in suspension, shown in Figure 4-4.) Since each cell develops a very low

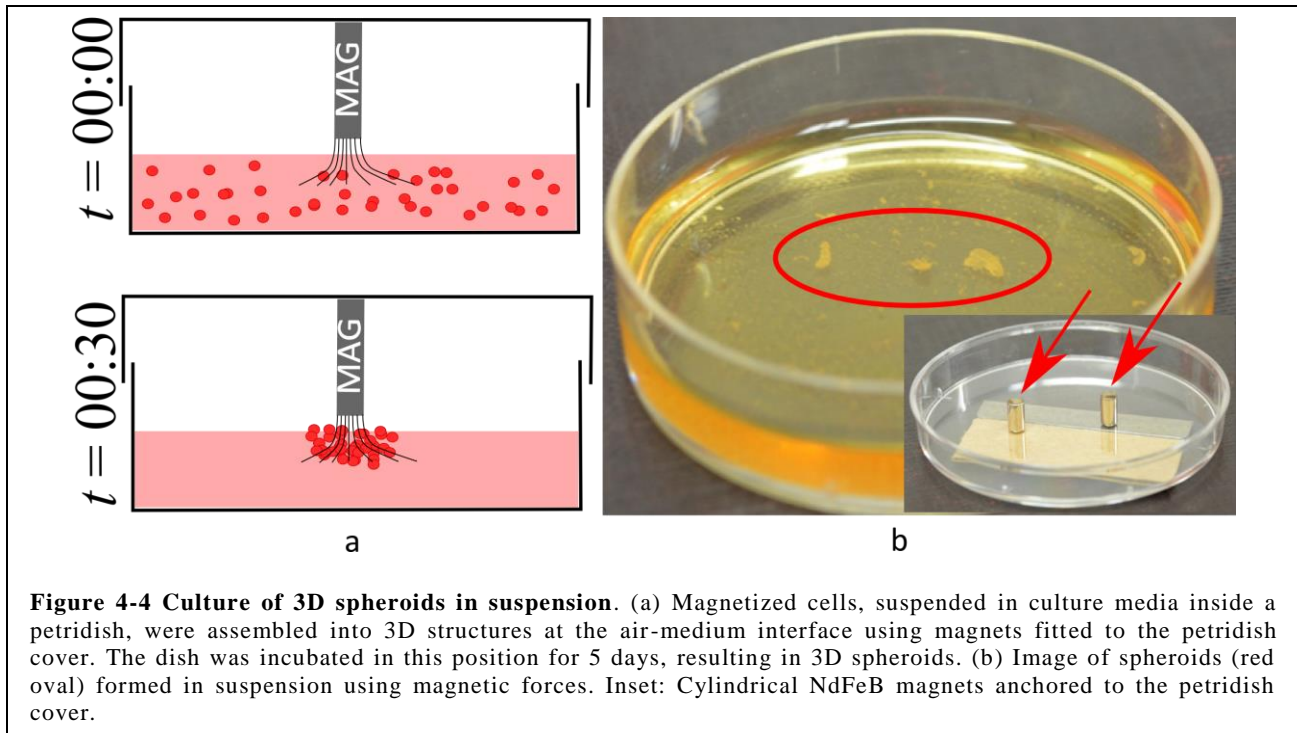


Figure 4-4 Culture of 3D spheroids in suspension. (a) Magnetized cells, suspended in culture media inside a petridish, were assembled into 3D structures at the air-medium interface using magnets fitted to the petridish cover. The dish was incubated in this position for 5 days, resulting in 3D spheroids. (b) Image of spheroids (red oval) formed in suspension using magnetic forces. Inset: Cylindrical NdFeB magnets anchored to the petridish cover.

magnetization, inter-cellular magnetostatic interactions are extremely weak. From the principles of magnetostatics, when a group of cells is pulled towards a substrate using a permanent magnet, they spread out as a very thin layer [48]. In order to develop thicker layers, we use magnetophoretic transport in conjunction with cellular adhesion. The 3D clusters of cells are built in layers through a multi-step seeding process, illustrated in Figure 4-3 (a). A small droplet ($\sim 100 \mu\text{L}$) of medium containing suspended magnetized cells is first placed on a glass coverslip immediately above the permanent magnets. The cells settle on the substrate within ~ 5 minutes due to the magnetophoresis, forming a cluster whose shape is dictated by the magnetic field. Within an hour, these cells adhere to the glass substrate or the adjoining cells. A second drop of magnetized cell suspension is then placed on top of the first. The process can be repeated several times, depending on the desired thickness of the cell layer. A 6-stage seeding conducted in this manner, shown in Figure 4-3 (c), results in an opaque cell layer that is visible to the naked eye.

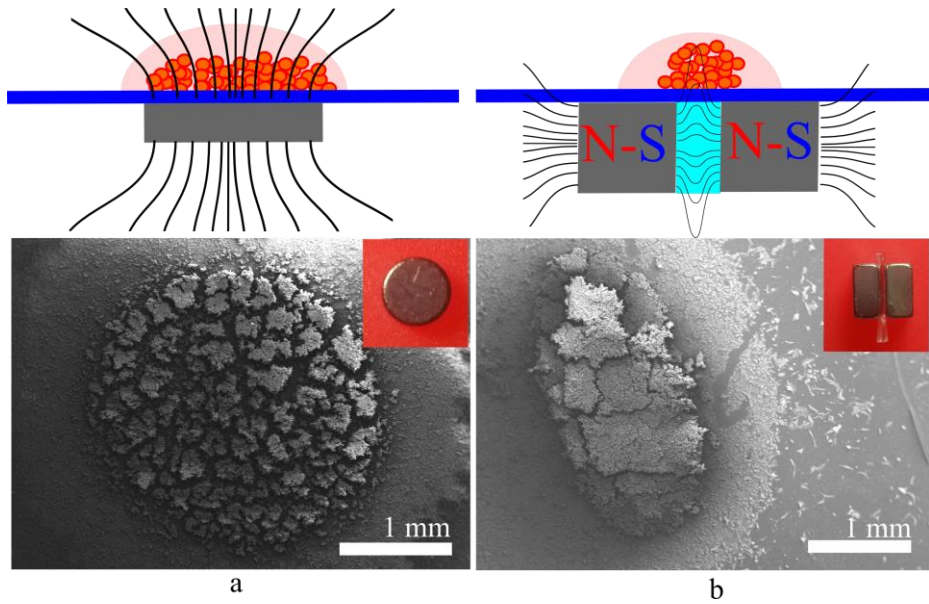


Figure 4-5 Control of shape using magnetic field. (a) A cylindrical disc magnet, which is axially magnetized, produced a circular sheet of cells. (b) A ‘flux gap’, formed by a layer of non-magnetic material sandwiched in between two rectangular magnets, produced a more anisotropic assembly. The PC-3 cell clusters presented here were fixed 5 days after seeding for SEM imaging. Insets: NdFeB magnet configuration used in each assembly. Note: Cracks in the cell assembly were a consequence of the sample preparation process; they were not seen in the live cell assembly

The shape and size of the assembly of cells can be controlled using the externally applied magnetic field. Cells settle on the coverslip at locations experiencing the highest magnetic field. Figure 4-5 shows two representative configurations of the permanent magnets. In the first, an axially magnetized cylindrical disc magnet is used. Such a magnet produces a ring-like geometry of field maxima on the coverslip immediately above the periphery of the magnet [86]. The cells thus initially organize themselves in a ring around the periphery. Subsequently, PC-3 cells organize into a disc-shaped multilayer sheet over the magnet, seen in Figure 4-5 (a). A second configuration uses a highly localized magnetic field gradient created by a ‘flux gap’ between two permanent magnets. This is produced by sandwiching a thin layer of non-magnetic polymer in between the two magnets. Cells adhere to the coverslip immediately above this gap, establishing an elongated cluster, seen in Figure 4-5 (b). Thus, depending on the desired shape of the cell assembly, the magnetic field can be determined *a priori*. The number of seeding stages can be

subsequently varied to obtain the desired thickness. Such a combination enables good control over the shape and size of the artificial ‘tissue’.

Cell morphology is known to differ vastly between monolayers and 3D cultures. This is clearly visible in the SEM images that we obtained. Figure 4-6 shows that the monolayers of two different cell lines take the familiar stretched and flattened morphology. When the same cells are assembled into 3D clusters, they are visibly less stretched. Confocal images also confirm this observation, as seen in Figure 4-7.

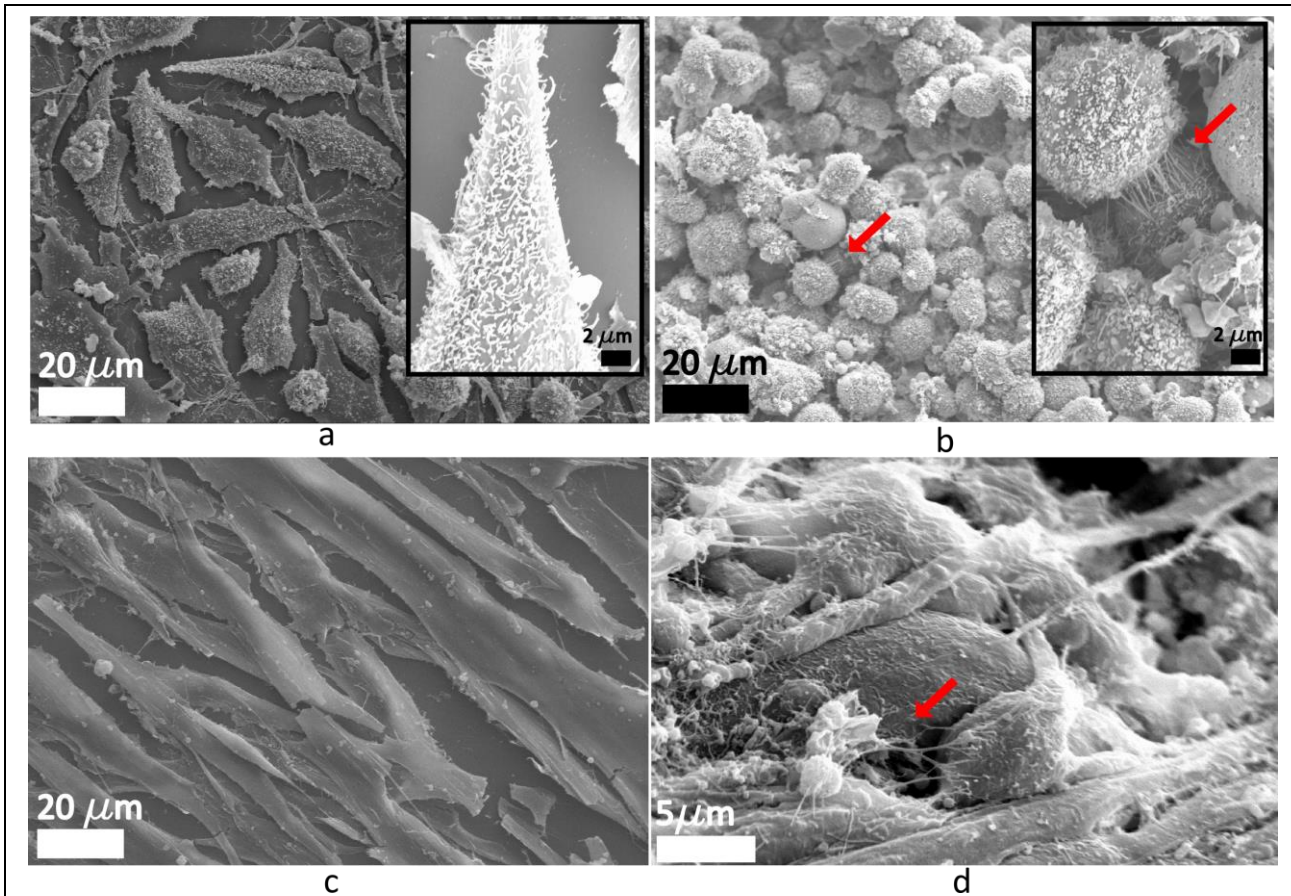
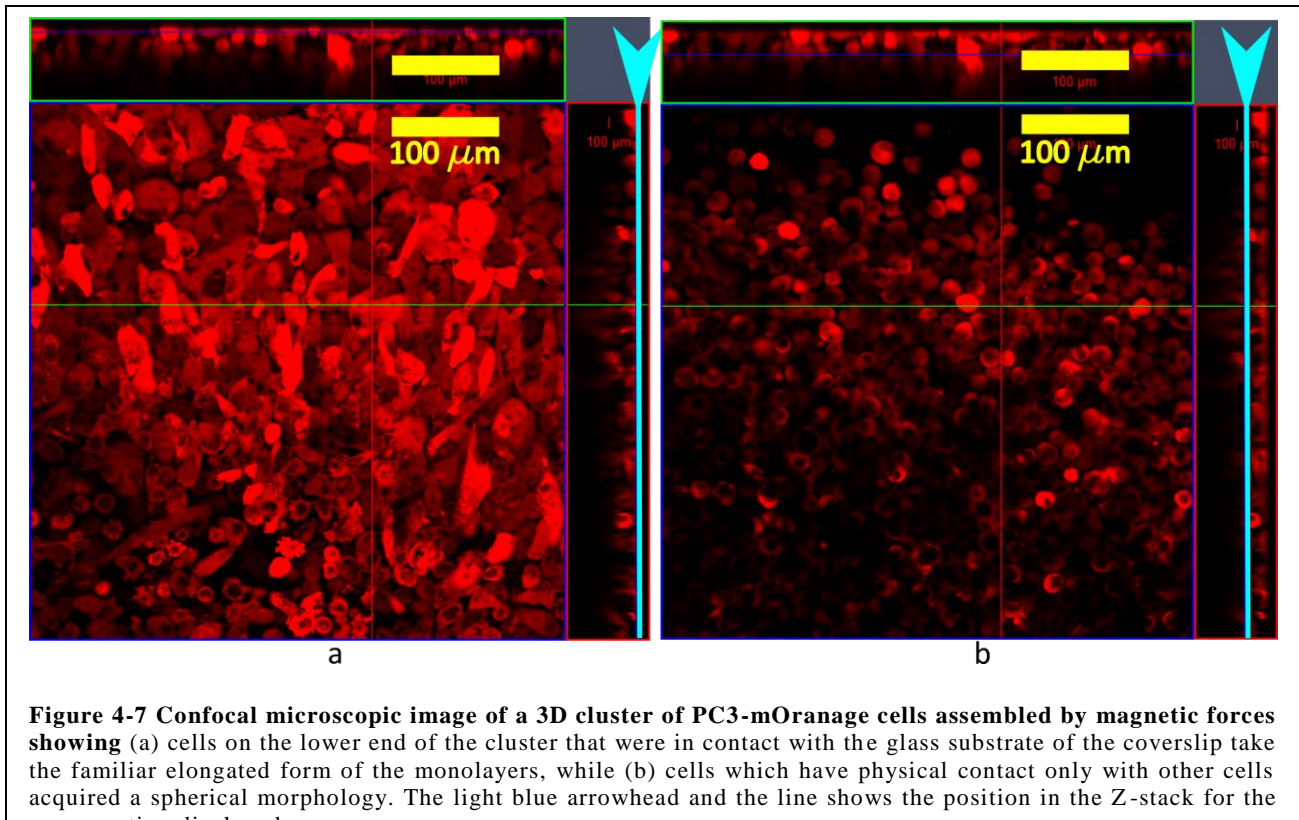


Figure 4-6 Morphology and Intercellular connections. Cell monolayers (a,c) acquired the familiar flattened form while cells organized into 3D clusters (b, d) were spheroidal. Cell-cell contacts were also influenced through the 3D assembly. (a) Monolayers of PC-3 cells showed extracellular fibers on their surface, but such fibers did not visibly serve any mechanical function. (b) When the PC-3 cells were organized into 3D clusters using magnetic forces, these fibers formed inter-cellular connections (see red arrows). (c) Monolayers of HFL-1 cells had no inter-cellular contact. (d) HFL-1 cells organized in 3D clusters exhibited ample evidence of inter-cellular contacts aided by extra-cellular fibers (see red arrow).



The most relevant difference between monolayers and 3D clusters is the cell-cell contacts, as seen in Figure 4-6. For the PC-3 cells, both monolayers and 3D clusters have fibers on the membrane. In the monolayers, seen in Figure 4-6 (a), these fibers do not serve any visible mechanical purpose. In the 3D clusters, similar fibers form contacts between cells, as seen in Figure 4-6 (b). For HFL-1, monolayer cells have a smooth membrane, as seen in Figure 4-6 (c). Figure 4-6 (d) shows that membranes of cells from 3D clusters have more asperities giving a corrugated appearance and form a larger number of cell-cell contacts. These contacts are aided by extracellular fibers giving credence to the observation that when cells are held in close proximity, they develop inter-cellular links and may form ECM, arguably transforming into a tissue [106, 107].

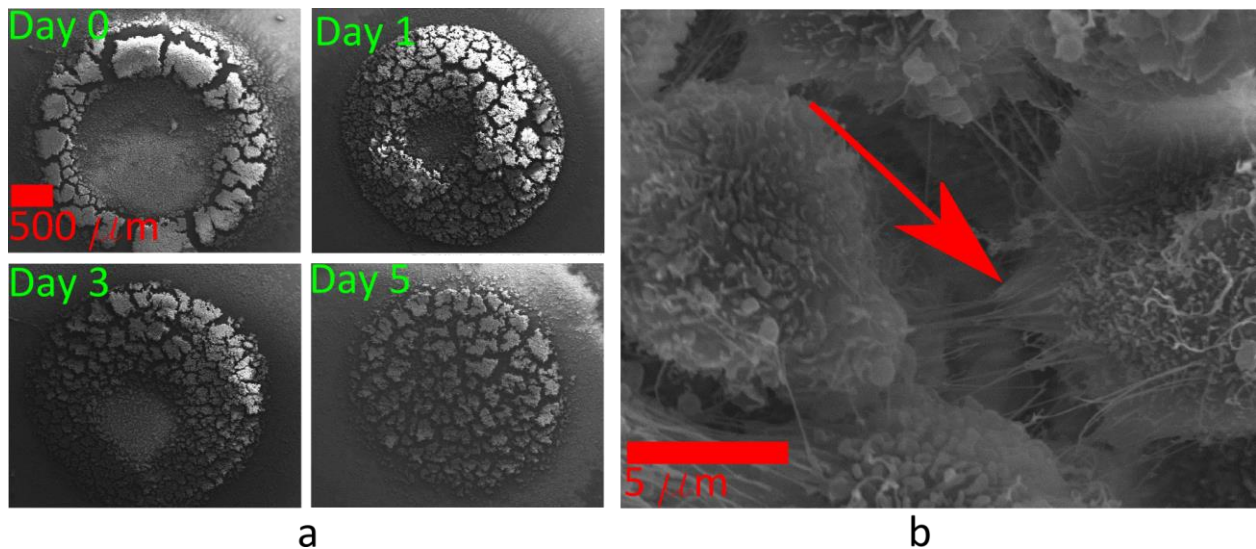


Figure 4-8 Figure 4 PC-3 cells organize themselves into a tight multilayer sheet. (a) PC-3 cells were initially assembled into a ring above a disc-shaped magnet. The cells organized themselves into a multilayer circular sheet over time. (b) Evidence of tension on an intercellular fiber given by observed stretching in the cell attached to it (red arrow) suggests that the cells pull themselves together using these fibers.

The intercellular fibers, besides ensuring rigidity of the ‘tissue’, possibly serve an important mechanical function, as observed for the PC-3 cells in Figure 4-8. We observe that when PC-3 cells are assembled into a ring, the cells organize themselves into a tighter disc. The process occurs gradually with time, as seen from the SEM images obtained by fixation of the cells at various time points after seeding. The magnetic force was applied for the entire length of the culture. Figure 4-8 (b) shows evidence of tension in the inter-cellular fiber connecting two cells. The cells attached to the fiber are stretched, indicating this tension. This may be the organizing force that results in tighter packing of the PC-3 cells on Day 5. Thus, the fibers making the inter-cellular contacts might be responsible for organizing the cells into a tighter clusters, in this case a multilayered sheet.

The temporal evolution of the shape of the cell assembly is even more interesting for the HFL-1 cell line, as seen in Figure 4-9. Starting from a ring-like cluster that is visually indistinguishable from that shown for Day 0 in Figure 4-8 (a) for PC-3 cells, the HFL-1 cells

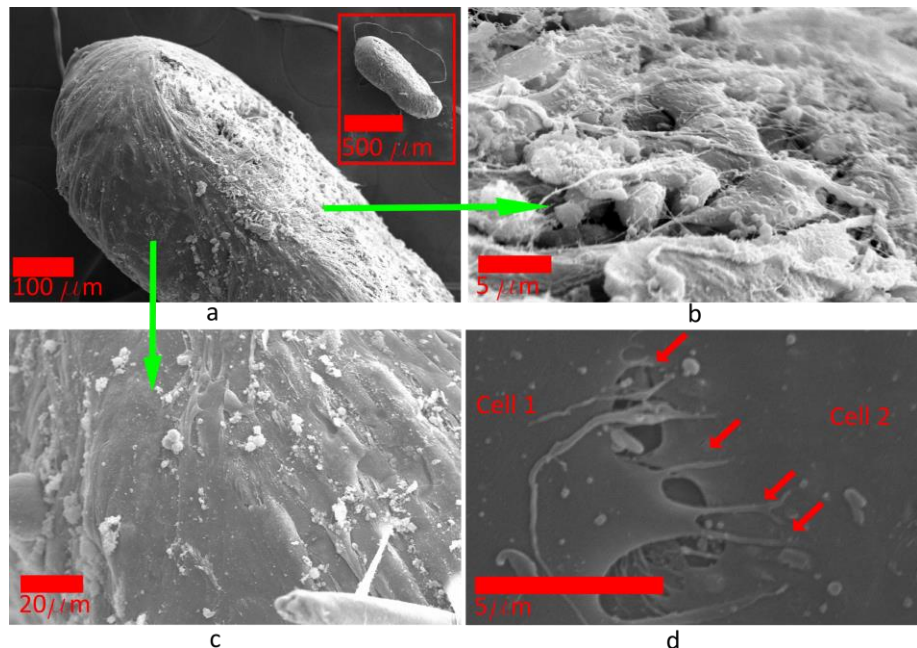


Figure 4-9 HFL-1 cells pack themselves into a tight spheroid. (a) Side view of a dislodged cluster (inset: lower magnification) shows (b) the underside that is torn away from the glass contains inter-cellular contacts and extracellular materials, while (c) the outside surface, which interfaced with the culture media, is smooth and comprised of stretched cells. (d) The stretched cells form inter-cellular contacts through filopodia-like protrusions.

organize themselves into a tightly packed spheroid within a day, as seen in Figure 4-9 (a). This spheroid is much smaller than the magnet, or the diameter of the initial ring that was formed. It can easily be dislodged from the glass substrate by agitation. The spheroid underside, which has been broken off from the glass substrate, show that the spheroid is formed of slightly stretched cells with several cell-cell connections. The spheroid outer surface, on the other hand, contains highly stretched cells with very smooth surfaces. These stretched cells are connected to each other at the boundaries through cytoplasmic protrusions that look like filopodia, as seen in Figure 4-9 (d), forming a ‘skin’ over the entire spheroid surface exposed to the media during growth. This shows how cells readily differentiate their morphology, possibly based on functional requirements in their environment. However, it should be noted that we did not examine the functional characteristics of any of these cell types.

4.4 Conclusions

In conclusion, we present a 3D cell culture method without using any scaffolding materials. Instead, we use magnetic forces to assemble cells into 3D clusters. When the cells are held in place by a magnetic field, they form cell-cell contacts which are aided by extra-cellular fibers. All cell lines organized themselves into tight clusters when cultured in 3D for several days. For the epithelial cell line (PC-3), the cluster takes the form of a multi-layer sheet. For fibroblasts (HFL-1), it is a tightly packed spheroid. The connecting fibers are observed to exercise tension on the cells. This suggests that the fibers are responsible for organizing the cells into a tighter cluster. For the HFL-1 cell line, cells on the periphery of the 3D clusters assume a different morphology than the cells that lie within them. This shows that cells assume different physical forms possibly based on their functional role, as determined by sensing their microenvironment. These 3-D clusters can be easily assembled in any laboratory practicing cell culture and can be made up of a single cell type or many different cell types as seen in tissue architecture. The advantage this method offers over conventional methods is that it is scaffold-free and allows directed organization into a desired form and possibly function.

4.5 Acknowledgements

We thank Kathy Lowe of the Virginia-Maryland Regional College of Veterinary Medicine for sample preparation and user training for SEM imaging, Kristi DeCourcy of the Fralin Life Science Institute at Virginia Tech for assistance with confocal imaging, Chris Winkler and the ICTAS Nanoscale Characterization and Fabrication Facility at Virginia Tech for TEM imaging of nanoparticles, Adria Allen (Dr. Elankumaran's laboratory) for stably transfected PC-3 cells expressing mOrange, Sonal Mazumdar, Sharavanan Balasubramanian and Richey Davis for

access to and user training of DLS and NanoSight, Daniel Dudek for the use of his fume hood in nanoparticle synthesis and Moanaro Biswas for helpful discussions.

5. Patterning stiffness of elastomers by magnetophoretic control of catalyst inhibitor distribution⁴

We present a method to pattern the stiffness of an elastomer by controlling the concentration distribution of magnetite nanoparticles (MNPs). The nanoparticles inhibit the platinum catalyst used to accelerate cross-linking reactions. The MNP concentration distribution is controlled in the liquid precursor to polydimethylsiloxane (PDMS) using a magnetic field. When the polymer is cured in the presence of a magnetic field, portions of PDMS that contain higher concentration of MNPs exhibit a lower stiffness. This method can be used to pattern any arbitrary stiffness geometry in PDMS by selecting the required magnetic field geometry *a priori*. Up to 200% variation in E_r is observed over a 2 mm length, and gradients of up to 12.6 MPa mm^{-1} are recorded. Thus, the method is capable of producing high-resolution patterns that are suitable for micro-electromechanical devices and 3D printing systems.

5.1 Motivation and background

Patterning heterogeneities in material properties, i.e., functional grading, enhances the mechanical performance of materials [108]. Nano- and micro-scale patterning abilities are particularly significant, since these are known to enhance damage tolerance in tough biomaterials, e.g., bones [109, 110]. However, existing methods to pattern heterogeneities are archaic, since they only enable unidirectional grading [111]. Here, we present a method to enforce heterogeneities in the stiffness of an elastomer in any arbitrary pattern. Such variations

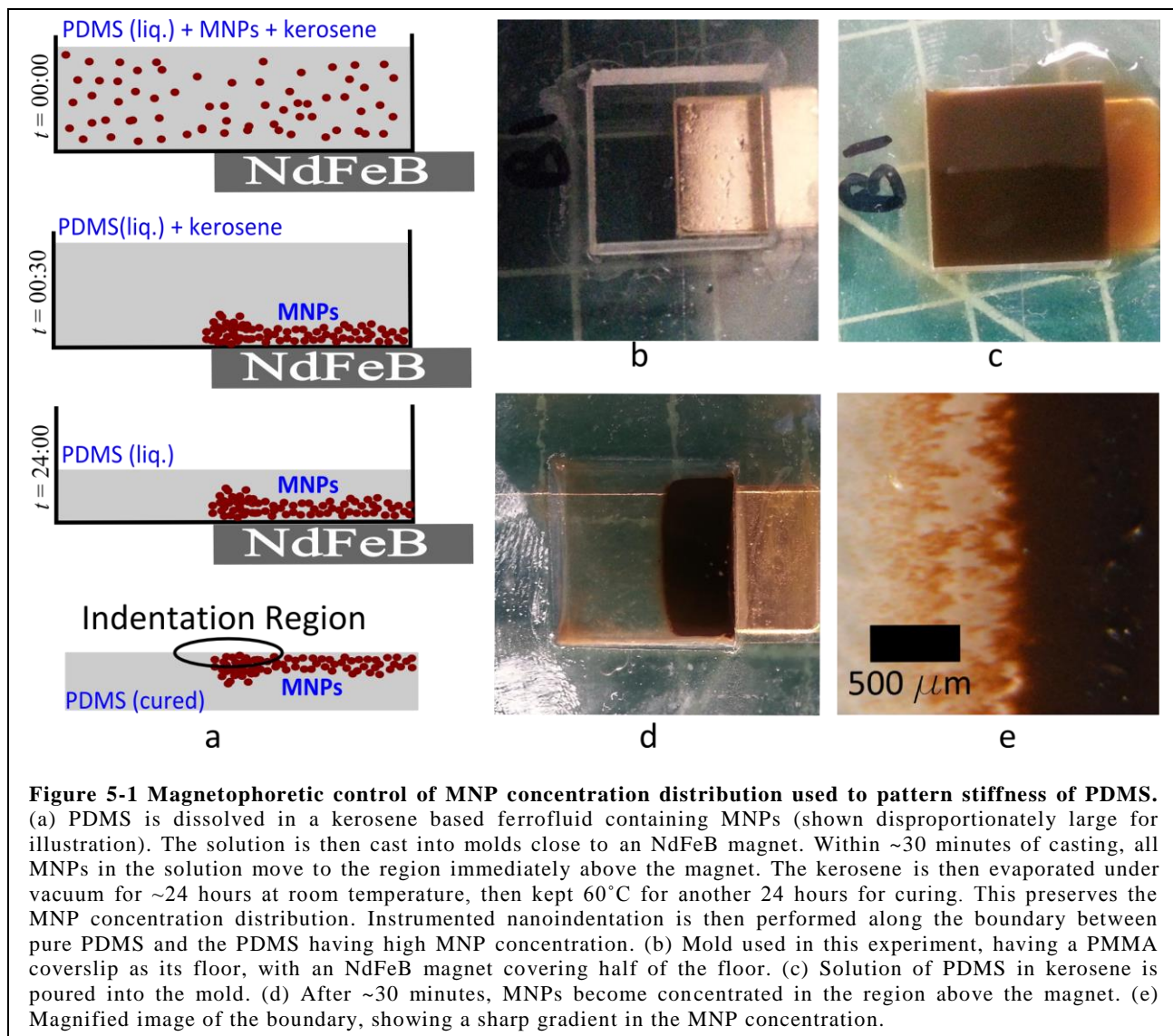
⁴Adapted from S. Ghosh *et al.*, “Patterning Stiffness of Elastomers by Magnetophoretic Control of Catalyst Inhibitor Distribution”, *In preparation*, 2013.

are realized by locally inhibiting the platinum catalyst used for polymer cross-linking reactions in polydimethylsiloxane (PDMS). To do so, the concentration distribution of magnetite nanoparticles (MNPs) in the liquid precursor of PDMS is controlled using an externally applied magnetic field. We demonstrate up to 200% variation in the elastic modulus of PDMS over a 2 mm length. Thus, a high-resolution, sharp gradient pattern in the elastic modulus becomes possible. The technique carries the potential to pattern material properties in micro-electromechanical devices and 3D printing systems.

Magnetic nanoparticles are well established in biomedical applications such as drug targeting because they can be manipulated remotely using a magnetic field, and conjugated with bio-molecules [53, 93, 94, 112-114]. Thus, the concentration distribution of MNP-conjugated biomolecules can be controlled, enabling localized reactions at desired locations [23, 24]. To our knowledge, we present the first use of such control on reagent concentration to pattern the stiffness of a material.

PDMS crosslinks in the presence of a platinum catalyst. When MNPs are mixed with the liquid precursor of PDMS, the catalyst is inhibited [37, 38]. This degrades the elastic modulus E of the polymer. In contradiction to the well-known mixture rule, a higher concentration of MNPs yields a lower E for the PDMS. Moreover, the concentration distribution of MNPs in PDMS can be controlled using an externally applied magnetic field [48]. The magnetophoretic control over MNP concentration distribution and the catalyst inhibiting effect of these MNPs are combined herein to prescribe a desired pattern for the elastic modulus in a PDMS-MNP composite system. The spatial distribution of the modulus is then mapped using instrumented nanoindentation. The method is illustrated in Figure 5-1.

The wide adoption of polymeric materials over the past few decades has led to several methods to grade polymer properties. Grading in polymers is typically accomplished in composites wherein a dispersed phase (A) is distributed in a polymeric matrix (B). Phase A is typically introduced into phase B by solvent casting or dissolution in the melt of B. Gradients in A-B proportions produce spatial variations in properties [115]. Grading is often only achieved in discrete steps, e.g., using compression molding of multiple composite sheets with composition variations [116], or by layer-wise curing of co-polymer blends in varied proportions [117],



thereby limiting the resolution. A continuous grading can be accomplished when A and B have different densities. For instance, centrifugal or gravity forces can induce variations in the ratio of the two phases [118-121]. For smaller length scales, continuous grading is enforceable by diffusion, allowing little control [122, 123]. Other methods such as mixing melts of co-polymers [124] and sophisticated extrusion processes [125] have also been reported. However, none of these methods enable heterogeneities beyond a unidirectional composition gradient. By using magnetic forces to control the MNP concentration in PDMS, we present a method to pattern any arbitrary distribution of stiffness after determining a suitable magnetic field distribution *a priori*. A proof of concept towards this is presented here.

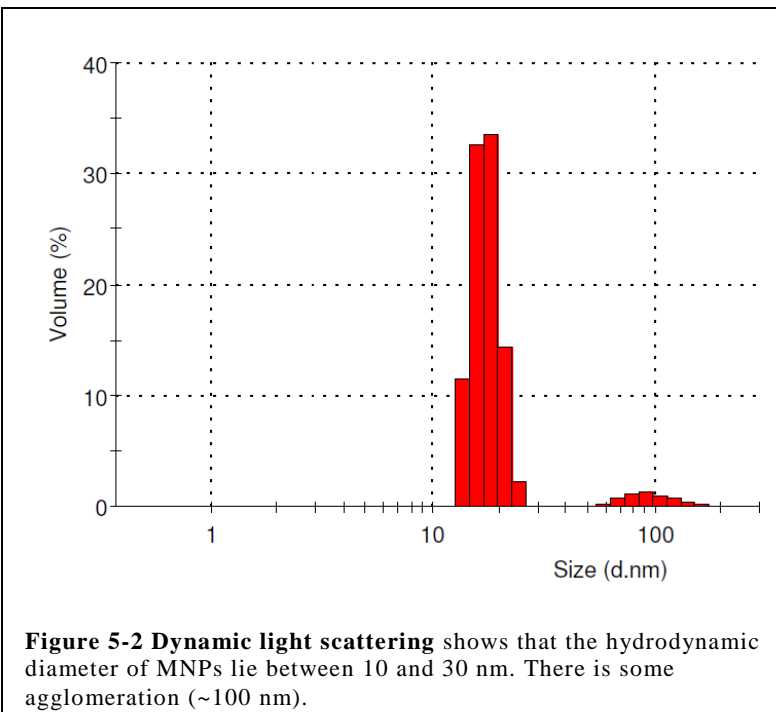
MNP-polymer nanocomposites have been explored extensively over the last decade [126, 127]. These are usually synthesized by solvent-casting the polymers after dissolving them in a colloidal dispersion of MNPs. An external magnetic field is then used to organize the MNPs into a desired microstructure. The solvent is subsequently evaporated and the polymer cured under exposure to the magnetic field, thus preserving the microstructure [48]. This enables a ‘material printer’. Beginning with the same polymer-MNP solution, an external magnetic field is used to vary the properties of the final material that is obtained [27-29, 128]. In addition, once cured, mechanical properties of such a material can be tuned at will using an external field [28, 128].

5.2 Materials and methods

5.2.1 Synthesis of Magnetic Nanoparticles and Ferrofluid

A stock ferrofluid of known MNP concentration is prepared by dispersing the nanoparticles in kerosene using oleic acid as surfactant. First, MNPs are synthesized by coprecipitation of Fe^{2+} and Fe^{3+} chlorides in an alkaline solution [105, 129]. 44.5 gm $\text{FeCl}_2 \cdot 4\text{H}_2\text{O}$ (ACS Grade, A16327, Alfa Aesar) and 120.8 gm $\text{FeCl}_3 \cdot 6\text{H}_2\text{O}$ (ACS Grade, 12497, Alfa Aesar) are dissolved in 300 ml

of degassed deionized water (LabChem, ASTM Type II). The solution is added slowly to 372 ml NH₄OH with vigorous stirring. A black precipitate of MNPs is immediately formed. The solution is heated to near boiling while stirring occasionally with a glass rod. 22.5 ml of oleic acid (A16663, Alfa Aesar) is added and the



solution stirred vigorously to mix. It is then maintained at near boiling for 2 hours until all the ammonia has evaporated. The solution is then cooled to room temperature and 367.5 ml of kerosene (K-1 grade, Sunnyside) is added to the solution. The solution is mixed vigorously until the kerosene is emulsified and then allowed to settle overnight. The MNPs, coated with oleic acid, are hydrophobic. They are exchanged from the water to the kerosene. Thus, when this mixture is allowed to settle overnight, the kerosene along with the MNPs moves to the top while transparent water is observed at the bottom. The kerosene-based ferrofluid is then decanted off. Dynamic Light Scattering (Malvern ZetaSizer Nano ZS-90) is used to determine the hydrodynamic diameter of the particles. The mean diameter is ~15 nm, as seen in Figure 5-2.

5.2.2 Preparation of Nanocomposites

The PDMS pre-deposition solution should have a low viscosity to ensure a thorough dispersion of MNPs in the PDMS. Thus, we begin with a solution containing 1:1 (w/w) of PDMS and kerosene. In order to accomplish this, the stock ferrofluid is first diluted in kerosene to obtain the desired mass ratio of MNPs to PDMS, ψ . The two parts of PDMS (SylgardTM 184, Dow Corning) are separately mixed in the prescribed ratio of 9:1 (w/w). The PDMS is then dissolved in the diluted ferrofluid so that the final mixture has equal weight of kerosene and PDMS. The solution is vigorously stirred until it appears to be homogeneous under an optical microscope. The solution is then transferred into PMMA molds (described later) that have attached NdFeB magnets, which provide the required magnetic field. The molds containing the PDMS-MNP mixture are transferred to a vacuum oven. Each sample is first placed at an absolute pressure of ~5 kPa for 24 hours at room temperature to evaporate the kerosene. The samples are then subjected to 60°C for another 24 hrs so that the PDMS cures. Figure 5-1 (a) illustrates this in detail.

5.2.3 Mold Fabrication

The sample molds are formed by cutting 15 mm square holes on a 3mm thick polymethylmethacrylate (PMMA) sheet using an Epilog laser cutter. The mold bottoms are produced using plastic cover slips (VWR, thickness 250 μm). For samples with patterned heterogeneities, about half of a coverslip is covered with a rectangular NdFeB rare earth magnet (Grade N52, 1/2"×1/2" ×1/8", gold plated, K&J Magnetics B882G-N52). The molds are shown in Figure 5-1 (b).

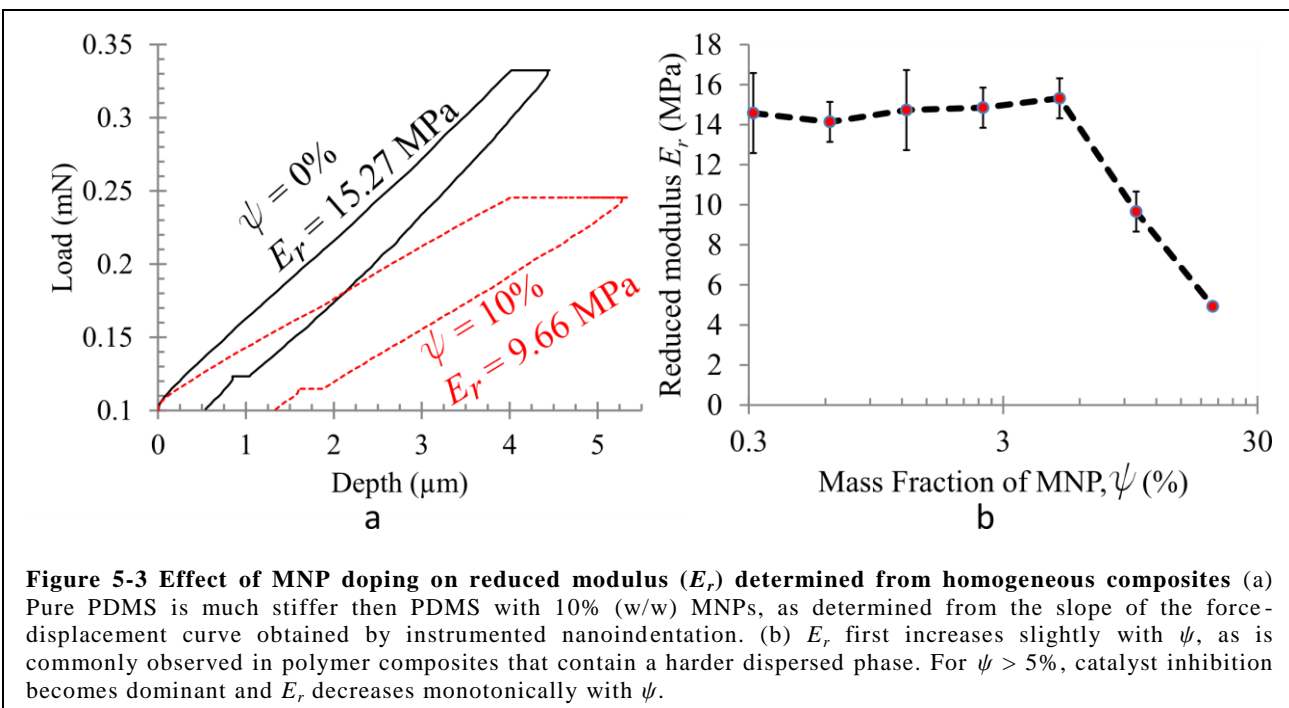


Figure 5-3 Effect of MNP doping on reduced modulus (E_r) determined from homogeneous composites (a) Pure PDMS is much stiffer than PDMS with 10% (w/w) MNPs, as determined from the slope of the force-displacement curve obtained by instrumented nanoindentation. (b) E_r first increases slightly with ψ , as is commonly observed in polymer composites that contain a harder dispersed phase. For $\psi > 5\%$, catalyst inhibition becomes dominant and E_r decreases monotonically with ψ .

5.2.4 Nanoindentation

Instrumented nanoindentation tests are performed using a NanoTestTM instrument (Micro Materials, UK). A 5 μm diameter spherical diamond indenter is used [130]. The maximum indentation depth is limited to 4 μm , with a loading time of 30 s, unloading time of 10 s and a dwell period of 80 s. The data are corrected for thermal drifts. The analysis of the load-indentation depth is performed using the Oliver-Pharr method [131].

5.3 Results and discussions

A higher weight percentage of MNPs (ψ) present during the curing process of PDMS leads to a lower reduced modulus (E_r) [37, 38]. This is verified by preparing composite samples that contain a homogeneous distribution of MNPs in the absence of a magnetic field. The corresponding indentation data are presented in Figure 5-3. We observe that E_r first increases slightly with ψ up to $\psi = 5\%$. We attribute this to the elastic modulus of magnetite (Fe_3O_4),

which is much higher than that of PDMS. This slight enhancement in E_r is commonly observed in polymer composites that contain a harder dispersed phase. However, at a higher MNP concentration, catalyst inhibition becomes dominant and E_r decreases monotonically. For $\psi > 20\%$, the inhibition effect reaches a level where a functional solid is no longer formed. Similar observations have been reported before [38].

Portions of the PDMS-MNP solution experiencing higher magnetic field strengths acquire a larger MNP concentration. Thus, cross-linking of the elastomer at desired locations is selectively inhibited. A high concentration of the MNPs collects above the magnet due to magnetophoresis. The highest concentration is located close to the periphery of the magnet, which experiences the strongest magnetic field. Thus, this region should have the lowest E_r . Moving away from this region should show a gradual increase in E_r . We test this by performing indentations over a 10×5 matrix of points on the region of the sample that has the largest MNP concentration gradient, i.e., on the sample surface that was closest to the periphery of the magnet during curing. These results are presented in Figure 5-4. To cover a large area, we use a coarse grid with $\Delta y = 500 \mu\text{m}$ and $\Delta z = 250 \mu\text{m}$. We denote the weight percentage of MNPs relative to PDMS in the starting solution by ψ^* . Heterogeneities in ψ are patterned using three different values of the starting concentration, i.e., $\psi^* = 0.1\%, 0.5\%$ and 1.0% . The MNP distribution is visibly most clear in the sample with $\psi^* = 0.1\%$, presented in Figure 5-4 (a). A band of MNPs is observed in the sample obtained from the region immediately above the magnet's edge. Approximate positions of the indentations are illustrated on this image. Figure 5-4 (b) shows that variations in E_r are unidirectional in this region, as expected from the pattern in the MNP concentration. The material is most stiff, i.e., E_r is highest in the region that contains pure PDMS ($\psi = 0$). It decreases gradually along y due to the increase in ψ . The stiffness again rises beyond

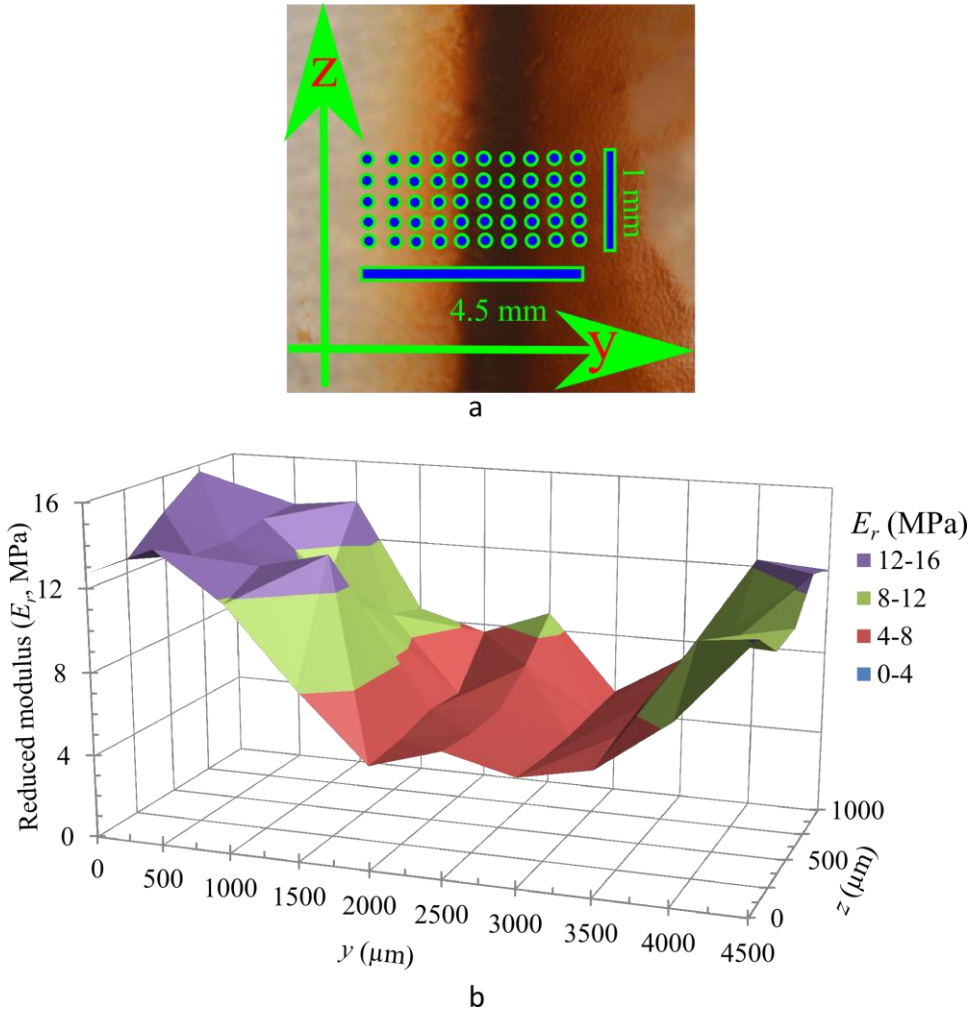


Figure 5-4 Magnetophoretic patterning of E_r . (a) The magnetic field is strongest along the periphery of the rectangular NdFeB magnet, thus MNP concentration is highest immediately above the periphery. The sample shown here has a starting MNP concentration $\psi^* = 0.1\%$ which best illustrates this feature. The dots show approximate locations of indentation points. (b) Map of E_r obtained from indentation at these points show that E_r varies along y axis. Data presented is for a sample with $\psi^* = 1.0\%$.

the band of high ψ . The starting concentration $\psi^* = 1.0\%$ produces the most distinct heterogeneities. A higher ψ^* results in a band of uncured PDMS above the magnet's edge because the local MNP concentration there exceeds the threshold $\psi = 20\%$.

Next, in order to determine the resolution of the method, we determine the gradient in E_r . We perform indentations in a straight line normal to the band of high MNP concentration at intervals of $\Delta y = 50 \mu\text{m}$. As presented in Figure 5-5, the highest gradient in E_r is observed for ψ^*

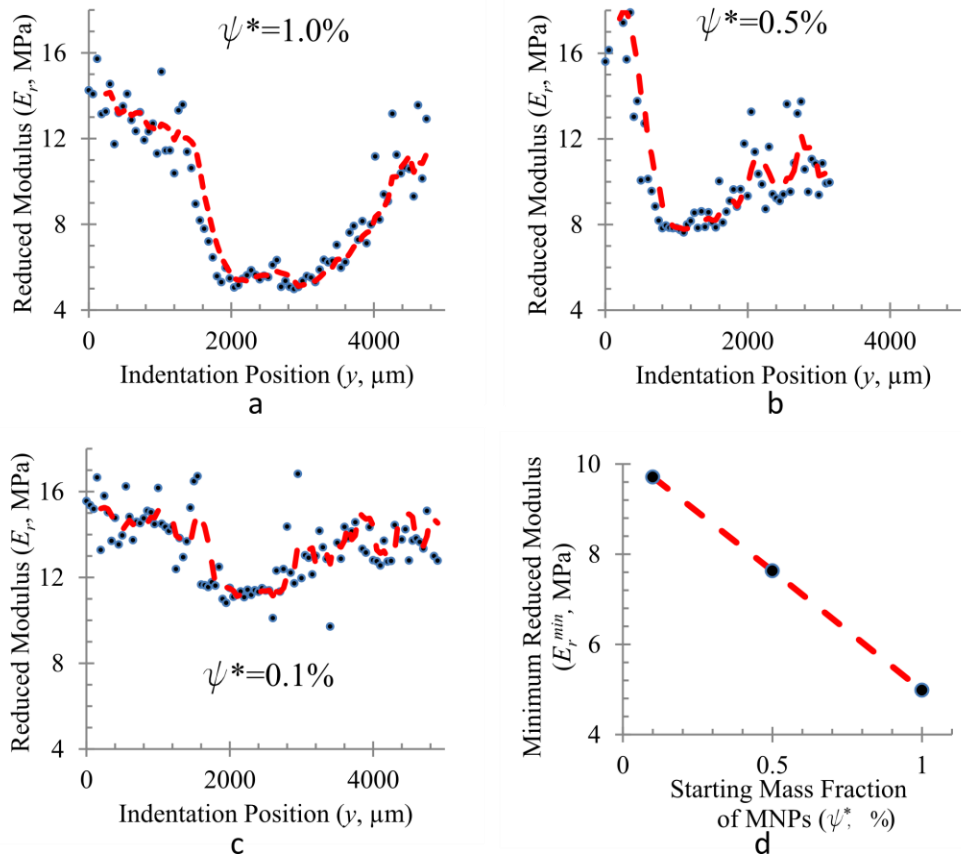


Figure 5-5 High resolution scan of E_r along a straight line for samples with (a) $\psi^* = 1.0\%$, (b) $\psi^* = 0.5\%$, (c) $\psi^* = 0.1\%$ shows that high gradients of the reduced modulus can be formed. The steepest gradient in (a) is 12.6 MPa mm^{-1} ($R^2 = 0.9623$). The general U-shaped profile is seen in all samples. The red dashed line is a 5-point moving average. (d) The minimum reduced modulus (E_r^{\min}) decreases linearly with ψ^* .

$= 1.0\%$. E_r ranges from ~ 15 MPa to ~ 5 MPa within a span of 2 mm. The steepest gradient is 12.6 MPa mm^{-1} , obtained by fitting a straight line over 10 points ($R^2 = 0.9623$). The gradient decreases for lower values of ψ^* . While the trend is clear, significant noise in the data prevents an accurate enumeration of any metrics for gradient. In homogeneous samples, the noise is eliminated by repeating the indentation multiple times at various locations. However, in a heterogeneous sample, this is not possible. The general ‘U’ shape in the E_r profile is observed for all three values of ψ^* . The minimum reduced modulus E_r^{\min} is the lowest for the highest value of ψ^* , and decreases linearly with increasing ψ^* , as seen in Figure 5-5 (d). The width of U also increases with increasing ψ^* .

5.4 Conclusions

In summary, we present a method to pattern the stiffness of an elastomer by controlling the concentration distribution of an MNP catalyst inhibitor, where the catalyst is used to accelerate cross-linking reactions. The MNP concentration distribution is controlled in the liquid precursor to PDMS using a magnetic field. When the polymer is cured in the presence of a magnetic field, portions of PDMS that contain higher concentration of MNPs exhibit a lower stiffness. This method can be used to pattern any arbitrary stiffness geometry in PDMS by selecting the required magnetic field geometry *a priori*. Up to 200% variation in E_r is observed over a 2 mm length, and gradients of up to 12.6 MPa mm^{-1} are recorded. Thus, the method is capable of producing high-resolution patterns that are suitable for micro-electromechanical devices and 3D printing systems.

5.5 Acknowledgements

We thank Prof. Daniel M. Dudek for the use of his fume hood for nanoparticle synthesis and ferrofluid preparation, Prof. Douglas P. Holmes and Mr. Anupam Pandey for access to a laser cutter for preparing the molds and Dr. Radim Ctvrtlik for helpful discussions.

6. Future directions

External control over organization and self-assembly of nanoparticles promises applications spanning multiple disciplines. This dissertation discusses the use of a static magnetic field to organize magnetic nanoparticles and magnetized human cells. However, control of self-assembly among nanoparticles will improve by orders of magnitude once the full spectrum of electromagnetic control has been explored. This will enable the design and fabrication of any conceivable structure by self-assembly of nanoparticle building blocks. The investigation will require novel experimental methods complemented by theoretical and computational models that couple electromagnetism with Stokesian particle dynamics. The knowledge gained will advance scientific understanding of inter-particle interactions at small scales. It will have significant applications in material design, tissue engineering and regenerative medicine.

6.1 Vision

Natural materials present a vivid example of how ‘form defines function’. Properties and behavior of any material are defined by the organization of its constituent atoms; diamond, graphite and carbon black are made of identical carbon atoms. Differing crystal structures (or the lack thereof) lead to starkly different mechanical, electrical and optical properties. On-demand control of crystal structure will enable tunable material properties – an object of science fiction. However, while Mother Nature had the luxury to ‘make’ her own atoms, our means to control ‘atomic organization’ are limited by her rules of chemical bonding. Nanoparticles, however, solve this problem. Being only several atoms in size, they can be used as building blocks of matter. Bulk properties of general composite materials depend on microstructure morphology, and microstructure can be generated by self-assembly of nanoparticles. Thus, control over

self-assembly will enable a ‘material printer’; starting from the same constituents, we can conceive of a device that will ‘print’ a material of desired mechanical, electrical, thermal, magnetic and optical properties. The microstructure morphology can often be changed on-demand after the material is formed using external triggers, e.g., electromagnetic field. This will enable tunable materials. Leveraging controlled organization of nanoparticles is the next step in mankind’s effort to control its environment. Unfortunately, the means to organize nanoparticles are rather limited, mainly because inter-particle interactions at small scales are not fully understood. Thus, the next step is to form a detailed understanding of inter-particle interactions and the means to control them. A few specific research topics are discussed hereinafter.

6.2 Controlled Self-assembly of Nanoparticles

Self-assembly is enabled by inter-particle interactions. For certain interactions, e.g., magnetostatic and electrostatic, self-assembly can be controlled by an external impetus, e.g., an electromagnetic field. However, electromagnetism and classical dynamics have been historically isolated. Combining these two will reveal methods to control the organization of nanoparticles with unparalleled flexibility.

The first step in this direction is to form an exhaustive map of electromagnetic control over nanoparticle self-assembly. This will involve synthesis and stabilization of the nanoparticles and detailed characterization of their size, shape and properties. Subsequently, external control on their self-assembly can be investigated by applying suitable electric and magnetic fields. This process will require an extensive use of 2D and 3D visualization tools spanning several orders of magnitude in length scale, e.g., SEM, TEM, X-Ray CT. The study remains incomplete if the geometry of structures cannot be predicted *a priori*. Thus, experimental observations need to be complemented by theoretical models that correlate process control variables to structure morphology. Such models will need to accurately describe inter-particle interactions at the nanoscale. The governing dynamics of millions of interacting particles presents mathematical complexities that cannot be treated by an analytical framework. Thus, scaling laws need to be developed. Parallelized computational models are a useful tool in this context. Specifically, established

methods in Stokesian Particle Dynamics will serve as an excellent tool to model the dynamics of interacting particles. The computational models are crucial in validating and fine-tuning the theoretical models that describe inter-particle interactions.

6.3 Magnetic Forces in Biotechnology

An important application area for directed assembly is biology, specifically tissue engineering and novel tools that will enable fundamental discoveries. This is because it allows a method for contactless manipulation of cells using magnetic forces, enabling their organization into a ‘tissue’ of desired form [86, 96, 97]. It also enables a method to deliver mechanical perturbations on live cells, enabling experiments that are otherwise impossible [98].

For decades, scientists have relied on petri-dish bound monolayer cell cultures to determine cell behavior. 3D cell cultures, which have emerged recently, better represent *in vivo* conditions than monolayers. This is because cell behavior is strongly influenced by interactions with its microenvironment, i.e., with neighboring cells and the extra-cellular matrix (ECM). Popular 3D culture methods employ synthetic materials as scaffolds in order to simulate the ECM. Since these materials are foreign to the cultured cells, cell behavior differs from that *in vivo*. Also, no control over shape of cell culture is possible. This dissertation reports the first evidence that cells, when held together by magnetic forces for several days, organize themselves towards a functional tissue. The method points to a transformational tool for fundamental discoveries in biology. For instance, it will enable the influence of tissue morphology on cell growth and differentiation. It will also enable studying intercellular communications, a phenomenon that drives all cellular processes within a living body.

Biocompatible MNPs developed in the course of the work will also support several other experiments on cell mechanics, e.g., the influence of mechanical cues on cellular response. Here, the mechanical perturbation will be provided by microstructures formed by self-assembly of magnetic nanoparticles. Subsequently, the microstructures can be manipulated remotely to ‘poke’ a cell in various different ways. Considering the microstructures are formed by self-assembly, they can be generated both

within and outside a cell. Further, from the understanding of the mechanics of a magnetic material in a magnetic field, the ‘poking’ force produced by such microstructures can be accurately calculated from knowledge of the magnetic field they experience.

6.4 Material Design

Magnetic nanoparticles are popular in biomedical applications such as drug targeting because the particles can be (1) manipulated remotely using a magnetic field, and (2) conjugated with bio-molecules. Thus, a concentration distribution of the molecules can be enforced externally, enabling localized reactions at desired locations. The materials world will also benefit from external control on concentration distribution of reagents to enforce localized reactions; the first evidence is presented in this dissertation.

The ability to pattern heterogeneities in material properties of any arbitrary geometry has promising potential in material design. This is because the bulk properties of a material have a strong dependence on the micro- or nanoscale heterogeneities. In the long run, a ‘material printer’ is envisaged. This is a ‘science fiction’ device that can ‘print’ a material of desired properties starting from a ‘cartridge’ of available nanomaterials and a polymer solution. For this, the first step is to investigate the influence of patterned heterogeneities in mechanical, magnetic and electrical properties on the corresponding bulk properties of materials.

7. References

- [1] S. Timoshenko and D. H. Young, *Elements of strength of materials*. Princeton, N.J.: Van Nostrand, 1968.
- [2] R. W. Gallant and C. L. Yaws, *Physical properties of hydrocarbons*. Houston: Gulf Pub. Co., 1993.
- [3] R. Kappiyoor, G. Balasubramanian, D. M. Dudek, and I. K. Puri, "Elastomechanical properties of resilin," *Soft Matter*, vol. 7, pp. 11006-11009, 2011.
- [4] S. C. Glotzer and M. J. Solomon, "Anisotropy of building blocks and their assembly into complex structures," *Nature Materials*, vol. 6, pp. 557-562, Aug 2007.
- [5] A. Traverset, "Self-Assembly Enters the Design Era," *Science*, vol. 334, pp. 183-184, October 14, 2011 2011.
- [6] K. J. M. Bishop, C. E. Wilmer, S. Soh, and B. A. Grzybowski, "Nanoscale Forces and Their Uses in Self-Assembly," *Small*, vol. 5, pp. 1600-1630, Jul 2009.
- [7] N. Bao and A. Gupta, "Self-assembly of superparamagnetic nanoparticles," *Journal of Materials Research*, vol. 26, pp. 111-121, 2011.
- [8] A. A. Tseng, C. Kuan, C. D. Chen, and K. J. Ma, "Electron beam lithography in nanoscale fabrication: recent development," *Electronics Packaging Manufacturing, IEEE Transactions on*, vol. 26, pp. 141-149, 2003.
- [9] M. J. Guffey and N. F. Scherer, "All-optical patterning of Au nanoparticles on surfaces using optical traps," *Nano letters*, vol. 10, p. 4302, 2010.

- [10] K. Butter, P. H. H. Bomans, P. M. Frederik, G. J. Vroege, and A. P. Philipse, "Direct observation of dipolar chains in iron ferrofluids by cryogenic electron microscopy," *Nature Materials*, vol. 2, pp. 88-91, Feb 2003.
- [11] K. Butter, P. H. H. Bomans, P. M. Frederik, G. J. Vroege, and A. P. Philipse, "Direct observation of dipolar chains in ferrofluids in zero field using cryogenic electron microscopy," *Journal of Physics: Condensed Matter*, vol. 15, p. S1451, 2003.
- [12] S. Mazumder, S. Ghosh, and I. K. Puri, "Non-premixed flame synthesis of hydrophobic carbon nanostructured surfaces," *Proceedings of the Combustion Institute*, vol. 33, pp. 3351-3357, 2011.
- [13] G. M. Whitesides and B. Grzybowski, "Self-assembly at all scales," *Science*, vol. 295, pp. 2418-2421, Mar 2002.
- [14] A. Centrone, Y. Hu, A. M. Jackson, G. Zerbi, and F. Stellacci, "Phase Separation on Mixed-Monolayer-Protected Metal Nanoparticles: A Study by Infrared Spectroscopy and Scanning Tunneling Microscopy," *Small*, vol. 3, pp. 814-817, 2007.
- [15] K. Nakata, Y. Hu, O. Uzun, O. Bakr, and F. Stellacci, "Chains of Superparamagnetic Nanoparticles," *Advanced Materials*, vol. 20, pp. 4294-4299, 2008.
- [16] A. M. Jackson, Y. Hu, P. J. Silva, and F. Stellacci, "From homoligand- to mixed-ligand-monolayer-protected metal nanoparticles: A scanning tunneling microscopy investigation," *Journal of the American Chemical Society*, vol. 128, pp. 11135-11149, Aug 2006.
- [17] A. M. Jackson, J. W. Myerson, and F. Stellacci, "Spontaneous assembly of subnanometre-ordered domains in the ligand shell of monolayer-protected nanoparticles," *Nature Materials*, vol. 3, pp. 330-336, May 2004.

- [18] A. Karimi, B. Denizot, F. Hindre, R. Filmon, J. M. Gremec, S. Laurent, *et al.*, "Effect of chain length and electrical charge on properties of ammonium-bearing bisphosphonate-coated superparamagnetic iron oxide nanoparticles: formulation and physicochemical studies," *Journal of Nanoparticle Research*, vol. 12, pp. 1239-1248, May 2010.
- [19] D. V. Talapin, E. V. Shevchenko, M. I. Bodnarchuk, X. Ye, J. Chen, and C. B. Murray, "Quasicrystalline order in self-assembled binary nanoparticle superlattices," *Nature*, vol. 461, pp. 964-967, 2009.
- [20] I. L. Medintz, H. T. Uyeda, E. R. Goldman, and H. Mattoussi, "Quantum dot bioconjugates for imaging, labelling and sensing," *Nature Materials*, vol. 4, pp. 435-446, Jun 2005.
- [21] R. Shenthal, T. B. Norsten, and V. M. Rotello, "Polymer-mediated nanoparticle assembly: Structural control and applications," *Advanced Materials*, vol. 17, pp. 657-669, Mar 2005.
- [22] J. Xiao and A. Zangwill, "Macrospin Models of Spin Transfer Dynamics," *Physical Review B*, vol. 72, pp. 01446-1 - 01446-13, 2005.
- [23] L. Bonnemay, S. Hostachy, C. Hoffmann, J. Gautier, and Z. Gueroui, "Engineering Spatial Gradients of Signaling Proteins Using Magnetic Nanoparticles," *Nano Letters*, 2013.
- [24] C. Alexiou, W. Arnold, R. J. Klein, F. G. Parak, P. Hulin, C. Bergemann, *et al.*, "Locoregional cancer treatment with magnetic drug targeting," *Cancer research*, vol. 60, pp. 6641-6648, 2000.
- [25] C. P. Bean and J. D. Livingston, "Superparamagnetism," *Journal of Applied Physics*, vol. 30, pp. S120-S129, 1959.

- [26] W. J. Chen, S. F. Zhang, and H. N. Bertram, "Energy barriers for thermal reversal of interacting single domain particles," *Journal of Applied Physics*, vol. 71, pp. 5579-5584, Jun 1992.
- [27] A. S. Robbes, F. Cousin, F. Meneau, F. Dalmas, F. Boue, and J. Jestin, "Nanocomposite Materials with Controlled Anisotropic Reinforcement Triggered by Magnetic Self-Assembly," *Macromolecules*, vol. 44, pp. 8858-8865, Nov 2011.
- [28] Z. Varga, G. Filipcsei, and M. Zrínyi, "Magnetic field sensitive functional elastomers with tuneable elastic modulus," *Polymer*, vol. 47, pp. 227-233, 2006.
- [29] D. Fragouli, R. Buonsanti, G. Bertoni, C. Sangregorio, C. Innocenti, A. Falqui, *et al.*, "Dynamical Formation of Spatially Localized Arrays of Aligned Nanowires in Plastic Films with Magnetic Anisotropy," *ACS Nano*, vol. 4, pp. 1873-1878, Apr 2010.
- [30] J. Ge, L. He, Y. Hu, and Y. Yin, "Magnetically induced colloidal assembly into field-responsive photonic structures," *Nanoscale*, vol. 3, pp. 177-183, 2011.
- [31] S. Bader and S. Parkin, "Spintronics," *Annu. Rev. Condens. Matter Phys.*, vol. 1, pp. 71-88, 2010.
- [32] Z. Z. Sun, A. Lopez, and J. Schliemann, "Zero-field magnetization reversal of two-body Stoner particles with dipolar interaction," *Journal of Applied Physics*, vol. 109, May 2011.
- [33] A. R. Kose, B. Fischer, L. Mao, and H. Koser, "Label-free cellular manipulation and sorting via biocompatible ferrofluids," *Proceedings of the National Academy of Sciences*, vol. 106, pp. 21478-21483, December 22, 2009 2009.

- [34] A. Sinha, R. Ganguly, and I. K. Puri, "Magnetic separation from superparamagnetic particle suspensions," *Journal of Magnetism and Magnetic Materials*, vol. 321, pp. 2251-2256, 2009.
- [35] R. Ganguly and I. Puri, "Field-assisted self-assembly of superparamagnetic nanoparticles for biomedical, MEMS and BioMEMS applications," *Advances in applied mechanics*, vol. 41, pp. 293-335, 2007.
- [36] R. Ganguly, A. P. Gaind, S. Sen, and I. K. Puri, "Analyzing ferrofluid transport for magnetic drug targeting," *Journal of Magnetism and Magnetic Materials*, vol. 289, pp. 331-334, 2005.
- [37] F. Pirmoradi, L. N. Cheng, and M. Chiao, "A magnetic poly(dimethylesiloxane) composite membrane incorporated with uniformly dispersed, coated iron oxide nanoparticles," *Journal of Micromechanics and Microengineering*, vol. 20, Jan 2010.
- [38] F. Fahrni, M. W. J. Prins, and L. J. van IJzendoorn, "Magnetization and actuation of polymeric microstructures with magnetic nanoparticles for application in microfluidics," *Journal of Magnetism and Magnetic Materials*, vol. 321, pp. 1843-1850, 2009.
- [39] F. Fahrni, M. W. J. Prins, and L. J. van IJzendoorn, "Micro-fluidic actuation using magnetic artificial cilia," *Lab on a Chip*, vol. 9, pp. 3413-3421, 2009.
- [40] B. A. Evans, A. R. Shields, R. L. Carroll, S. Washburn, M. R. Falvo, and R. Superfine, "Magnetically Actuated Nanorod Arrays as Biomimetic Cilia," *Nano Letters*, vol. 7, pp. 1428-1434, 2007.
- [41] Y. Lalatonne, J. Richardi, and M. P. Pilani, "Van der Waals versus dipolar forces controlling mesoscopic organizations of magnetic nanocrystals," *Nat Mater*, vol. 3, pp. 121-125, 2004.

- [42] Y. Sahoo, M. Cheon, S. Wang, H. Luo, E. P. Furlani, and P. N. Prasad, "Field-Directed Self-Assembly of Magnetic Nanoparticles," *The Journal of Physical Chemistry B*, vol. 108, pp. 3380-3383, 2004/03/01 2004.
- [43] M. Klokkenburg, B. H. Erne, J. D. Meeldijk, A. Wiedenmann, A. V. Petukhov, R. P. A. Dullens, *et al.*, "In situ imaging of field-induced hexagonal columns in magnetite ferrofluids," *Physical Review Letters*, vol. 97, Nov 2006.
- [44] W. K. Lee, "X-ray microtomography of field-induced macro-structures in a ferrofluid," *Journal of Magnetism and Magnetic Materials*, vol. 322, pp. 2525-2528, Sep 2010.
- [45] H. Zeng, J. Li, J. P. Liu, Z. L. Wang, and S. Sun, "Exchange-coupled nanocomposite magnets by nanoparticle self-assembly," *Nature*, vol. 420, pp. 395-398, 2002.
- [46] X. W. Teng, X. Y. Liang, S. Rahman, and H. Yang, "Porous Nanoparticle Membranes: Synthesis and Application as Fuel-Cell Catalysts," *Advanced Materials*, vol. 17, pp. 2237-2241, 2005.
- [47] P. Y. Keng, B. Y. Kim, I.-B. Shim, R. Sahoo, P. E. Veneman, N. R. Armstrong, *et al.*, "Colloidal Polymerization of Polymer-Coated Ferromagnetic Nanoparticles into Cobalt Oxide Nanowires," *ACS Nano*, vol. 3, pp. 3143-3157, 2009/10/27 2009.
- [48] S. Ghosh and I. K. Puri, "Soft polymer magnetic nanocomposites: microstructure patterning by magnetophoretic transport and self-assembly," *Soft Matter*, vol. 9, pp. 2024-2029, 2013.
- [49] L. N. Donselaar, P. M Frederik, P. Bomans, P. A. Buining, B. M. Humbel, and A. P. Philipse, "Visualisation of particle association in magnetic fluids in zero-field," *Journal of Magnetism and Magnetic Materials*, vol. 201, pp. 58-61, 1999.

- [50] C. Neto, M. Bonini, and P. Baglioni, "Self-assembly of magnetic nanoparticles into complex superstructures: Spokes and spirals," *Colloids and Surfaces A: Physicochemical and Engineering Aspects*, vol. 269, pp. 96-100, 2005.
- [51] P. de Gennes and P. Pincus, "Pair correlations in a ferromagnetic colloid," *Zeitschrift für Physik B Condensed Matter*, vol. 11, pp. 189-198, 1970.
- [52] R. W. Chantrell, A. Bradbury, J. Popplewell, and S. W. Charles, "Agglomerate formation in a magnetic fluid," *Journal of Applied Physics*, vol. 53, pp. 2742-2744, 1982.
- [53] R. Ganguly and I. K. Puri, "Field-assisted self-assembly of superparamagnetic nanoparticles for biomedical, MEMS and BioMEMS applications," *Advances in Applied Mechanics*, vol. 41, pp. 293-335, 2007.
- [54] R. Ganguly, B. Zellmer, and I. K. Puri, "Field-induced self-assembled ferrofluid aggregation in pulsatile flow," *Physics of Fluids*, vol. 17, p. 097104, 2005.
- [55] R. Ganguly, A. P. Gaind, and I. K. Puri, "A strategy for the assembly of three-dimensional mesoscopic structures using a ferrofluid," *Physics of Fluids*, vol. 17, May 2005.
- [56] H. Bertram and J. Mallinson, "Switching dynamics for an interacting anisotropic dipole pair of arbitrary bond angle," *Journal of Applied Physics*, vol. 41, pp. 1102-1104, 1970.
- [57] H. Bertram and J. Mallinson, "Theoretical coercive field for an interacting anisotropic dipole pair of arbitrary bond angle," *Journal of Applied Physics*, vol. 40, p. 1301, 1969.
- [58] A. Lyberatos and R. W. Chantrell, "Thermal fluctuations in a pair of magnetostatically coupled particles," *Journal of Applied Physics*, vol. 73, pp. 6501-6503, May 1993.

- [59] D. Cimpoesu, A. Stancu, I. Klik, C. R. Chang, and L. Spinu, "Thermally activated transitions in a system of two single domain ferromagnetic particles," *Journal of Applied Physics*, vol. 109, Apr 2011.
- [60] S. Morup and E. Tronc, "Superparamagnetic Relaxation of Weakly Interacting Particles," *Physical Review Letters*, vol. 72, pp. 3278-3281, May 1994.
- [61] S. Mørup, "Superferromagnetic nanostructures," *Hyperfine Interactions*, vol. 90, pp. 171-185, 1994.
- [62] T. L. Gilbert, "A phenomenological theory of damping in ferromagnetic materials," *Magnetics, IEEE Transactions on*, vol. 40, pp. 3443-3449, 2004.
- [63] T. L. Gilbert, "A Lagrangian formulation of the gyromagnetic equation of the magnetization field.(Abstract only)," *Physical Review*, vol. 100, 1955.
- [64] A. Lyberatos, D. V. Berkov, and R. W. Chantrell, "A method for the numerical simulation of the thermal magnetization fluctuations in micromagnetics," *Journal of Physics: Condensed Matter*, vol. 5, pp. 8911-8920, Nov 1993.
- [65] Y. Nakatani, Y. Uesaka, N. Hayashi, and H. Fukushima, "Computer simulation of thermal fluctuation of fine particle magnetization based on Langevin equation," *Journal of Magnetism and Magnetic Materials*, vol. 168, pp. 347-351, 1997.
- [66] P. W. Ma and S. L. Dudarev, "Langevin spin dynamics," *Physical Review B*, vol. 83, Apr 2011.
- [67] L. Neél, "Théorie du traînage magnétique des ferromagnétiques en grains fins avec applications aux terres cuites," *Ann. géophys*, vol. 5, pp. 99-136, 1949.

- [68] P. V. Hendriksen, G. Christiansen, and S. Morup, "Magnetization Reversal in Chain Like Clusters of Interacting Particles," *Journal of Magnetism and Magnetic Materials*, vol. 132, pp. 207-218, Apr 1994.
- [69] E. Boerner and H. N. Bertram, "Non-Arrhenius behavior in single domain particles," *Magnetics, IEEE Transactions on*, vol. 34, pp. 1678-1680, 1998.
- [70] D. Rodé, H. N. Bertram, and D. R. Fredkin, "Effective Volume of Interacting Particles," *IEEE Transactions on Magnetics* vol. 23, pp. 2224-2226, Sep 1987.
- [71] J. L. Dormann, L. Bessais, and D. Fiorani, "A Dynamic Study of Small Interacting Particles-Superparamagnetic Model and Spin-Glass LawsLAWS," *Journal of Physics C-Solid State Physics*, vol. 21, pp. 2015-2034, Apr 1988.
- [72] I. Klik and C.-R. Chang, "Thermal relaxation in arrays of coupled ferromagnetic particles," *Physical Review B*, vol. 52, pp. 3540-3545, 1995.
- [73] W. F. Brown, "Thermal Fluctuations of a Single-Domain Particle," *Physical Review*, vol. 130, p. 1677, 1963.
- [74] D. V. Berkov and N. L. Gorn, "Susceptibility of the disordered system of fine magnetic particles: a Langevin-dynamics study," *Journal of Physics: Condensed Matter*, vol. 13, p. 9369, 2001.
- [75] D. V. Berkov, N. L. Gorn, R. Schmitz, and D. Stock, "Langevin dynamic simulations of fast remagnetization processes in ferrofluids with internal magnetic degrees of freedom," *Journal of Physics: Condensed Matter*, vol. 18, pp. S2595-S2621, Sep 2006.
- [76] M. Azeggagh and H. Kachkachi, "Effects of dipolar interactions on the zero-field-cooled magnetization of a nanoparticle assembly," *Physical Review B*, vol. 75, May 2007.

- [77] J. L. García-Palacios and F. J. Lázaro, "Langevin-dynamics study of the dynamical properties of small magnetic particles," *Physical Review B*, vol. 58, pp. 14937-14958, 1998.
- [78] H. B. Callen and T. A. Welton, "Irreversibility and Generalized Noise," *Physical Review*, vol. 83, pp. 34-40, 1951.
- [79] R. Kappiyoor, M. Liangruksa, R. Ganguly, and I. K. Puri, "The effects of magnetic nanoparticle properties on magnetic fluid hyperthermia," *Journal of Applied Physics*, vol. 108, Nov 2010.
- [80] R. Kappiyoor, M. Liangruksa, R. Ganguly, and I. K. Puri, "The effects of magnetic nanoparticle properties on magnetic fluid hyperthermia," *Journal of Applied Physics*, vol. 108, p. 094702, 2010.
- [81] F. Pampaloni, E. G. Reynaud, and E. H. K. Stelzer, "The third dimension bridges the gap between cell culture and live tissue," *Nat Rev Mol Cell Biol*, vol. 8, pp. 839-845, 10//print 2007.
- [82] J. T. Bergthorsson, M. K. Magnusson, and T. Gudjonsson, "Endothelial-rich microenvironment supports growth and branching morphogenesis of prostate epithelial cells," *The Prostate*, 2012.
- [83] A. J. Engler, S. Sen, H. L. Sweeney, and D. E. Discher, "Matrix elasticity directs stem cell lineage specification," *Cell*, vol. 126, pp. 677-689, 2006.
- [84] M. P. Lutolf and J. A. Hubbell, "Synthetic biomaterials as instructive extracellular microenvironments for morphogenesis in tissue engineering," *Nat Biotech*, vol. 23, pp. 47-55, 01//print 2005.

- [85] C. S. Hughes, L. M. Postovit, and G. A. Lajoie, "Matrigel: A complex protein mixture required for optimal growth of cell culture," *PROTEOMICS*, vol. 10, pp. 1886-1890, 2010.
- [86] G. R. Souza, J. R. Molina, R. M. Raphael, M. G. Ozawa, D. J. Stark, C. S. Levin, *et al.*, "Three-dimensional tissue culture based on magnetic cell levitation," *Nat Nano*, vol. 5, pp. 291-296, 2010.
- [87] S. Vukicevic, H. K. Kleinman, F. P. Luyten, A. B. Roberts, N. S. Roche, and A. Reddi, "Identification of multiple active growth factors in basement membrane Matrigel suggests caution in interpretation of cellular activity related to extracellular matrix components," *Experimental cell research*, vol. 202, pp. 1-8, 1992.
- [88] M. Rimann and U. Graf-Hausner, "Synthetic 3D multicellular systems for drug development," *Current Opinion in Biotechnology*, vol. 23, pp. 803-809, 10// 2012.
- [89] N. Blow, "Cell culture: building a better matrix," *Nat Meth*, vol. 6, pp. 619-622, 08//print 2009.
- [90] S. Grivennikov and M. Karin, "Autocrine IL-6 signaling: A key event in tumorigenesis?," *Cancer Cell*, vol. 13, pp. 7-9, Jan 2008.
- [91] S. Ghosh, S. Elankumaran, and I. K. Puri, "Mathematical model of the role of intercellular signalling in intercellular cooperation during tumorigenesis," *Cell Proliferation*, vol. 44, pp. 192-203, 2011.
- [92] D. E. Discher, D. J. Mooney, and P. W. Zandstra, "Growth Factors, Matrices, and Forces Combine and Control Stem Cells," *Science*, vol. 324, pp. 1673-1677, June 26, 2009 2009.

- [93] Q. A. Pankhurst, J. Connolly, S. K. Jones, and J. Dobson, "Applications of magnetic nanoparticles in biomedicine," *Journal of Physics D: Applied Physics*, vol. 36, p. R167, 2003.
- [94] Q. A. Pankhurst, N. K. T. Thanh, S. K. Jones, and J. Dobson, "Progress in applications of magnetic nanoparticles in biomedicine," *Journal of Physics D: Applied Physics*, vol. 42, p. 224001, 2009.
- [95] V. Clavijo-Jordan, V. D. Kodibagkar, S. C. Beeman, B. D. Hann, and K. M. Bennett, "Principles and emerging applications of nanomagnetic materials in medicine," *Wiley Interdisciplinary Reviews: Nanomedicine and Nanobiotechnology*, 2012.
- [96] K. Ino, A. Ito, and H. Honda, "Cell patterning using magnetite nanoparticles and magnetic force," *Biotechnology and Bioengineering*, vol. 97, pp. 1309-1317, 2007.
- [97] M. D. Krebs, R. M. Erb, B. B. Yellen, B. Samanta, A. Bajaj, V. M. Rotello, *et al.*, "Formation of Ordered Cellular Structures in Suspension via Label-Free Negative Magnetophoresis," *Nano Letters*, vol. 9, pp. 1812-1817, May 2009.
- [98] P. Tseng, J. W. Judy, and D. Di Carlo, "Magnetic nanoparticle-mediated massively parallel mechanical modulation of single-cell behavior," *Nat Meth*, vol. 9, pp. 1113-1119, 11/print 2012.
- [99] A. Bajaj, B. Samanta, H. Yan, D. J. Jerry, and V. M. Rotello, "Stability, toxicity and differential cellular uptake of protein passivated-Fe₃O₄ nanoparticles," *Journal of Materials Chemistry*, vol. 19, pp. 6328-6331, 2009.
- [100] S. Mohapatra, S. Mallick, T. Maiti, S. Ghosh, and P. Pramanik, "Synthesis of highly stable folic acid conjugated magnetite nanoparticles for targeting cancer cells," *Nanotechnology*, vol. 18, p. 385102, 2007.

- [101] K. Ino, A. Ito, H. Kumazawa, H. Kagami, M. Ueda, and H. Honda, "Incorporation of capillary-like structures into dermal cell sheets constructed by magnetic force-based tissue engineering," *Journal of Chemical Engineering of Japan*, vol. 40, pp. 51-58, Jan 2007.
- [102] A. Ito, M. Hayashida, H. Honda, K. I. Hata, H. Kagami, M. Ueda, *et al.*, "Construction and harvest of multilayered keratinocyte sheets using magnetite nanoparticles and magnetic force," *Tissue Engineering*, vol. 10, pp. 873-880, May 2004.
- [103] A. Ito, E. Hibino, C. Kobayashi, H. Terasaki, H. Kagami, M. Ueda, *et al.*, "Construction and delivery of tissue-engineered human retinal pigment epithelial cell sheets, using magnetite nanoparticles and magnetic force," *Tissue Engineering*, vol. 11, pp. 489-496, Mar 2005.
- [104] A. Ito, K. Ino, M. Hayashida, T. Kobayashi, H. Matsunuma, H. Kagami, *et al.*, "Novel methodology for fabrication of tissue-engineered tubular constructs using magnetite nanoparticles and magnetic force," *Tissue Engineering*, vol. 11, pp. 1553-1561, Sep 2005.
- [105] R. Massart, "Preparation of aqueous magnetic liquids in alkaline and acidic media," *IEEE Transactions on Magnetics* vol. 17, pp. 1247-1248, 1981.
- [106] J. M. Kelm, V. Lorber, J. G. Snedeker, D. Schmidt, A. Broggini-Tenzer, M. Weisstanner, *et al.*, "A novel concept for scaffold-free vessel tissue engineering: Self-assembly of microtissue building blocks," *Journal of Biotechnology*, vol. 148, pp. 46-55, Jul 1 2010.
- [107] Y.-C. Tung, A. Y. Hsiao, S. G. Allen, Y.-s. Torisawa, M. Ho, and S. Takayama, "High-throughput 3D spheroid culture and drug testing using a 384 hanging drop array," *Analyst*, vol. 136, pp. 473-478, 2011 2011.

- [108] S. Suresh, "Graded Materials for Resistance to Contact Deformation and Damage," *Science*, vol. 292, pp. 2447-2451, June 29, 2001 2001.
- [109] K. Tai, M. Dao, S. Suresh, A. Palazoglu, and C. Ortiz, "Nanoscale heterogeneity promotes energy dissipation in bone," *Nature Materials*, vol. 6, pp. 454-462, 2007.
- [110] G. Balooch, M. Balooch, R. K. Nalla, S. Schilling, E. H. Filvaroff, G. W. Marshall, *et al.*, "TGF-beta regulates the mechanical properties and composition of bone matrix," *Proceedings of the National Academy of Sciences of the United States of America*, vol. 102, pp. 18813-18818, Dec 2005.
- [111] B. Kieback, A. Neubrand, and H. Riedel, "Processing techniques for functionally graded materials," *Materials Science and Engineering: A*, vol. 362, pp. 81-106, 12/5/ 2003.
- [112] R. Ganguly and I. K. Puri, "Microfluidic transport in magnetic MEMS and bioMEMS," *Wiley Interdisciplinary Reviews: Nanomedicine and Nanobiotechnology*, vol. 2, pp. 382-399, 2010.
- [113] I. K. Puri and R. Ganguly, "Particle Transport in Therapeutic Magnetic Fields," *Annual Review of Fluid Mechanics*, vol. 46, 2014.
- [114] R. Ganguly and I. K. Puri, "Microfluidic transport in magnetic MEMS and bioMEMS," *Wiley Interdisciplinary Reviews-Nanomedicine and Nanobiotechnology*, vol. 2, pp. 382-399, Jul-Aug 2010.
- [115] M. Shen and M. B. Bever, "Gradients in polymeric materials," *Journal of Materials Science*, vol. 7, pp. 741-746, 1972/07/01 1972.
- [116] N. J. Lee and J. Jang, "The effect of fibre-content gradient on the mechanical properties of glass-fibre-mat/polypropylene composites," *Composites Science and Technology*, vol. 60, pp. 209-217, 2000 2000.

- [117] X. Q. Liu, Y. S. Wang, and J. H. Zhu, "Epoxy resin/polyurethane functionally graded material prepared by microwave irradiation," *Journal of Applied Polymer Science*, vol. 94, pp. 994-999, Nov 5 2004.
- [118] M. Krumova, C. Klingshirn, F. Haupert, and K. Friedrich, "Microhardness studies on functionally graded polymer composites," *Composites Science and Technology*, vol. 61, pp. 557-563, 3// 2001.
- [119] C. E. Rousseau and H. V. Tippur, "Influence of elastic variations on crack initiation in functionally graded glass-filled epoxy," *Engineering Fracture Mechanics*, vol. 69, pp. 1679-1693, Sep 2002.
- [120] X. F. Yao, T. C. Xiong, W. Xu, and H. Y. Yeh, "Experimental investigations on deformation and fracture behavior of glass sphere filled epoxy functionally graded materials," *Applied Composite Materials*, vol. 13, pp. 407-420, Nov 2006.
- [121] M. Kirugulige and H. Tippur, "Mixed-mode dynamic crack growth in functionally graded glass-filled epoxy," *Experimental mechanics*, vol. 46, pp. 269-281, 2006.
- [122] K. Yamazaki, T. Dong, N. Asakawa, Y. Inoue, and K. Yazawa, "Fabrication of Compositional-Gradient Biodegradable Polymeric Films Showing Self-Bending Deformation," *Macromolecular rapid communications*, vol. 30, pp. 435-441, 2009.
- [123] T. Saito, H. Tanuma, P. Pan, T. Dong, and Y. Inoue, "Gelatin/poly (ethylene oxide) blend films with compositional gradient: fabrication and characterization," *Macromolecular Materials and Engineering*, vol. 295, pp. 256-262, 2010.
- [124] B. Y. Wen, Q. C. Li, S. H. Hou, and G. Wu, "Preparation and structure study of polypropylene/polyamide-6 gradient materials," *Journal of Applied Polymer Science*, vol. 91, pp. 2491-2496, Feb 15 2004.

- [125] G. Wu, B. Y. Wen, and S. H. Hou, "Preparation and structural study of polypropylene-talc gradient materials," *Polymer International*, vol. 53, pp. 749-755, Jun 2004.
- [126] S. Abramchuk, E. Kramarenko, D. Grishin, G. Stepanov, L. V. Nikitin, G. Filipcsei, *et al.*, "Novel highly elastic magnetic materials for dampers and seals: part II. Material behavior in a magnetic field," *Polymers for Advanced Technologies*, vol. 18, pp. 513-518, 2007.
- [127] S. Abramchuk, E. Kramarenko, G. Stepanov, L. V. Nikitin, G. Filipcsei, A. R. Khokhlov, *et al.*, "Novel highly elastic magnetic materials for dampers and seals: Part I. Preparation and characterization of the elastic materials," *Polymers for Advanced Technologies*, vol. 18, pp. 883-890, 2007.
- [128] J. Jestin, F. Cousin, I. Dubois, C. Ménager, R. Schweins, J. Oberdisse, *et al.*, "Anisotropic Reinforcement of Nanocomposites Tuned by Magnetic Orientation of the Filler Network," *Advanced Materials*, vol. 20, pp. 2533-2540, 2008.
- [129] R. Massart, E. Dubois, V. Cabuil, and E. Hasmonay, "Preparation and properties of monodisperse magnetic fluids," *Journal of Magnetism and Magnetic Materials*, vol. 149, pp. 1-5, Aug 1995.
- [130] M. Tehrani, M. Safdari, and M. Al-Haik, "Nanocharacterization of creep behavior of multiwall carbon nanotubes/epoxy nanocomposite," *International Journal of Plasticity*, vol. 27, pp. 887-901, 2011.
- [131] W. C. Oliver and G. M. Pharr, "Measurement of hardness and elastic modulus by instrumented indentation: Advances in understanding and refinements to methodology," *Journal of Materials Research*, vol. 19, pp. 3-20, Jan 2004.